Front Microrheology of biological Fluids

Claudia A. Trejo Soto

UNIVERSITAT DE BARCELONA

FRONT MICRORHEOLOGY OF BIOLOGICAL FLUIDS

PH.D. THESIS

AUTHOR: CLAUDIA A. TREJO SOTO

ADVISOR: AURORA HERNÁNDEZ MACHADO

UNIVERSITAT DE BARCELONA
Departament d’ Estructura i Constituents de la Matèria
Programa de Doctorado en Física
Barcelona, 2016

This Thesis was posible thanks to the fellowships program Becas Chile from Conicyt and the Ministerio de Educación de Chile.

Its has also contributed the Facultat the Física of the Universitat de Barcelona.

Contents

I Introduction 1

Glossary

Symbols

Letter	*Name*	*Unit*
Q	Flow rate	$\frac{m^3}{s}$ or $\frac{\mu l}{min}$
η	Viscosity	$Pa \cdot s$
ρ	Density	$\frac{kg}{m^3}$
$\dot{\gamma}$	Shear Rate	s^{-1}
σ	Shear Stress	Pa
∇P	Pressure gradient	Pa/m
ΔP	Pressure drop	Pa
P_{atm}	Atmospheric pressure	Pa
P_{cap}	Capillary pressure	Pa
P_L	Laplace pressure	Pa
P_R	Resistance pressure	Pa
$P_{hyd} = \rho g H$	Hydrostatic pressure	Pa
g	Acceleration of gravity	$\frac{m}{s^2}$
H	Column height	m
h	Position	m
$\dot{h}_k$	Instant velocity	$\frac{m}{s}$
$\dot{h}$	Mean velocity	$\frac{m}{s}$ or $\frac{m}{s}$
v_t	Velocity in the tube	$\frac{\mu m}{s}$
v_c	Velocity in the channel	$\frac{m}{s}$
l_c	Channel's length	m
w	Channel's width	m
b	Channel's height, gap or depth	μm
l_t	Tube's length	m
r	Tube's radius	m
σ_{rs}	Rescaled pressure	Pa
$\dot{\gamma}_F$	Rescaled shear rate	s^{-1}
σ_w	Wall stress	Pa
$\dot{\gamma}_w$	Wall shear rate	s^{-1}
η_0	Solute viscosity	$Pa \cdot s$
$\eta_{eff} = \frac{\eta}{\eta_0}$	Effective viscosity	

Letter	*Name*	*Unit*
η_{norm}	Normalized viscosity	$Pa \cdot s$
ϕ	Hematocrit Concentration	
ν	Velocity exponent	
n	Viscosity exponent	
C_a	Capillary Number	
Re	Reynolds Number	
$\kappa \approx 50k_BT$	Bending coefficient	J
D_e	Well depth of the Morse potential	J
β	Width of the well of the Morse potential	
U_a	Aggregation energy	J

Abbreviations

Htc.	Hematocrit
Eq.	Equation
Fig.	Figure
Etgl.	Ethylene-glycol
Gl.	Glycerol

Acronyms

BEM	Element Boundary Method
BP	Blood Plasma
CGS	Centimeters-Grams-Seconds Unit System
DPD	Dissipative Particle Dynamics
ESR	Erythrocyte Sedimentation Rate
HIV	Human Immunodeficiency Virus
ISC	Irrevesible Sickle Cells
LB	Lattice Boltzmann Method
LD-RBC	Low Dimensional RBC Model
LoC	Lab on a Chip
MEMS	Micro Electro-Mechanical Systems
MS-RBC	Multiscale RBC Model
μTAS	micro Total Analysis System
PDMS	Poly-dimethylsiloxane
PET	Poly-ethylene
POCT	Point of Care Testing
RBC's	Red Blood Cells
SI	International Unit System
WBC's	White Blood Cells
WRM	Weissenberg-Rabinowitsch-Mooney

List of Figures

List of Tables

PART I

Introduction

General Introduction

Since ancient times scientist have been motivated to understand blood. Due to its complex nature and the lack of tools to study it, the road to its fully understanding has been slow and still growing. Even though, the peak of blood rheology research was between the 1960's and 1980's the development of new technologies have re-focus the interest in hemorheological research.

1.1 Background of hemorheology

By common knowledge we know that blood in rest separates in different layers of fluid. An upper layer known as serum or plasma, a thin layer of leukocytes and platelets and a red blood cells layer on the bottom. Early studies in ancient Greece developed a diagnostic method dependent on the proportions of those blood layers. This was the first attempt to relate blood to the diagnostic of deceases.

The breakthrough discovery of blood circulation in the XVII century by William Harvey opened a new door to the understanding of blood. This was a huge physiological insight and had a great importance for hemorheology because it exposed the importance of blood flow. Later, in 1660 Malpighi was the first to see micro circulation and to prove microscopically the connection of the network of small blood vessels, nevertheless, blood was still understood as a simple fluid. It was thanks to Anthoni van Leeuwenhoek in 1674 that this changed, as he rightly described red blood cells. He was accurate to observe RBC‘s deformation as they flow through capillaries. He also noticed red cells aggregation and discovered that it was related to pregnancy and infection, moreover, he related the increase of aggregation and alterations of red blood cells deformability to pathology. These discoveries are, still today, of major importance to hemorheology.

Years later, after many microscopic investigations of in vivo blood flow properties, Jean Leonard Poiseuille decided to simplified the problems with in vivo observation and decided to study blood flows in glass tubes. He realized that blood was very difficult to measure so he perform his study using simpler liquids like water. This experiments led to the publication in 1840 of the widely known Poiseuille Law [Poiseuille, 1844]. Since we now know that this law only applied to Newtonian fluids, it may be assume that the difficulties Poiseuille encounter were mostly due to the non-Newtonian behavior of blood.

A great deal of development in diagnostic came with the studies perform by Robin

Fåhraeus. He observed the relation between increased aggregation and rate of settling and developed the Erytrocytes Sedimentation Rate Test (ESRT), still nowadays a used quantitative diagnostic tool for some inflammatory diseases. He also made other contributions to hemorheology as he studied blood flow in very small diameter glass tubes which led to the discovery of the Fåhræus effect [Fåhræus, 1929] and later to the Fåhræus-Lindqvist effect [Fåhræus and Lindqvist, 1931]. By this time, it was determined that the elevated ESR was associated with an increase in the degree of formation of red blood cells aggregates in the blood which is related as well to high levels of plasma proteins, such as fibrinogen. This led to think that there was also an association between an increase in plasma viscosity, due to proteins, and pathology.

Blood studies continue to develop in the early twentieth century, and the dependency of an apparent viscosity of blood of the diameter of the tube through which it flows was found. It was also discovered the viscosity relation on its rate of flow which provided the proof of the shear thinning properties of blood. One of the biggest issues in this period was the lack of measurement techniques which did not allow the comparison of the results between different laboratories. In 1933 Whittaker and Winton develope in vivo experiment using dog blood. They were able to establish a logarithmic relation between viscosity and the hematocrit of a sample. They also determined that at the driving pressures and flow rates they used the viscosity was constant, meaning that blood behaved as a Newtonian fluid [Whittaker and Winton, 1933].

The lack of instrumentation that was holding up the advancements in hemorheology was overcome in the second half of the twentieth century. It started in 1963 when Harkness provided a solution to this by introducing the capillary viscometer which was used to determined plasma viscosity. Later, with the creation of viscometers capable of measure non-Newtonian viscosity in a standardized manner, the interest in hemorheology upraised between several investigation groups. One of the most notable apparatus created was the Weissenberg Rheogoniometer, Fig. 1.1. The instrument was later modified by A. L. Copley to allow its use on blood [King and Copley, 1970]. Fig. 1.2 shows one of the first results of blood viscosity using this new instrument. These changes generated a “boom” in the study of the viscometric properties of blood that extended from the 1960’s to the end of the 1980’s. The results of all this activities was the discovery of viscometric abnormalities in a vast array of clinical conditions [Dintenfass, 1971; Lowe et al., 1988]. Furthermore, the development of hemorheologically based pharmaceutical products was a main factor in the progress of clinical hemorheology in this period.

At the beginning of hemorheology studies, the viscoelastic properties of blood was the main area of study [Thurston, 1972]. However, the field began to extend and diversify and the interest in red blood cells properties and its deformability star to gain interest. This interest was also stimulated by the high number of studies been perform in sickle cell anemia, a blood disease directly related to cell deformability [Chien et al., 1970a]. Though at first, the methodologies for measuring red cell deformability were complex and expensive, simpler methodologies began to be developed. Red blood cells aggregation was as well a very studied subject, in fact several in vivo investigations of the effects of aggregation in hemodynamics have been attempt but are still unclear.

Since the peak of hemorheology several new areas have been growing to incorporate clinical applications of blood to diagnostic.

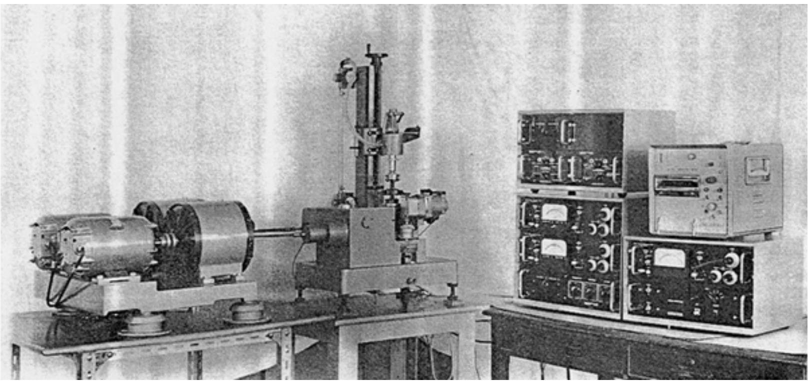

Figure 1.1: *Image of the Weissenberg Rheogoniometer. The image was obtained from: weissenberg.bsr.org.uk*

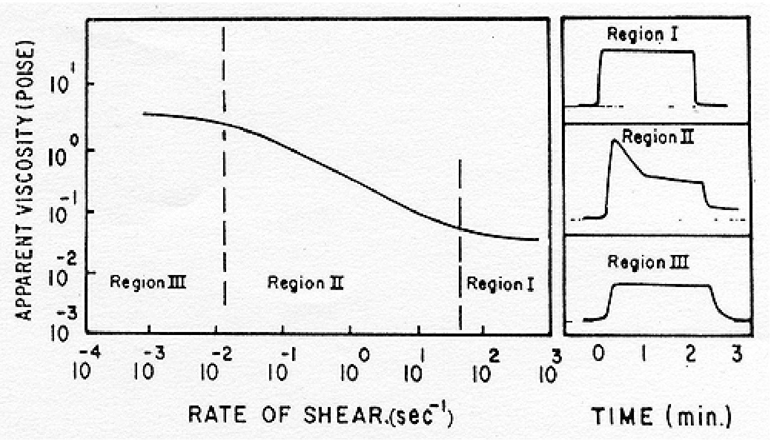

Figure 1.2: *The image shows one of the first results obtained for blood viscosity using the adapted Weissenberg Rheogoniometer for biological testing [King and Copley, 1970].*

A persistent problem in hemorheological investigation was the lack of relation between the hemodynamics in vivo and in vitro. The rise of microfluidics in the 1990's and the beginning of 2000's brought several new applications and innovation to many areas, such as, biological analysis and biomedical research [Whitesides, 2006]. The emergence of this new field allowed the in vitro replication of small confined channels with simple flow characteristics, shortening the gap of hemodynamics in vivo and in vitro [Thurston and Henderson, 2006].

During the last decade, bio-electronic industry has gain interest with intensive research performed in small portable devices capable of rapid detection and monitoring of lab scale processes allowing to perform diagnostic tests directly at the point of patient service. These applications have open a new focus on hemorheological properties and its relation with disease diagnostic.

1.2 The rise of a new technology

Microfluidics is known as the discipline and technology that allow the manipulation of small amounts of fluid at a submillimetre scale. The advantages of microfluidics devices are, their small size, the use of low amount of sample and the ability to reproduced laminar flow conditions, Fig. 1.3. An additional advantage at the microscale, is the low effect produced by gravity in comparison with macroscale conditions. However, other features as surface tension and capillary forces become dominant [Squires and Quake, 2005; Tabeling, 2010].

The origins of microfluidics are directly related to the progress in miniaturization. In the 1980's, the capacity to reduce the size of typical macroscale features to the microscale environment inspired the rise of MEMS (micro-electro-mechanical systems). During this decade MEMS became fundamental to several industrial applications, which enabled the expansion of the field [Gad-el-Hak, 2001]. Thus, at the beginning of the 1990's, these new applications gave birth to microfluidics devices which have the potential to perform fundamental studies of physical, chemical and biological processes.

From here, all sort of microfluidic systems began to be fabricated. Initially microfluidics devices were manufactured in silicon and glass, as MEMS. But these materials have been replaced by plastics [Martynova et al., 1997], polymers [McDonald and Whitesides, 2002] and, in the latest years, paper [Martinez et al., 2008] or wax [Nilghaz et al., 2012]. The emergence of new materials allowed to extend microfluidics features, since it is easier to fabricate the components for microcanalytical systems using elastic polymers (elastomers) than rigid materials. Most of the research in microfluidics have been performed with elastomer material such as poly(dimethylsiloxane) PDMS which properties provided simpler fabrication methods and increased functionality. The change to more flexible material enabled the creation of several component now typical integrated in microfluidics systems, such as, pipes, valves, mixers and pumps [Thorsen et al., 2002; Hong and Quake, 2003; Zhang et al., 2007].

The absence of movable parts in microfluidic devices and the relative easy accessibility to many of these technologies have made possible to integrate several elements on the same chip to create Lab-on-a-Chip Devices [Burns et al., 1998]. The rapid expansion of the field of microfluidics seems to be driven by the possibility of integration. The domain of integrated analysis systems has been designated as μTAS (micro-Total Analysis Systems) [Reyes et al., 2002; Arora et al., 2010]. The primary goal of these μTAS is to be able to process, detect and characterize a sample all in one single device.

Initial studies in microfluidics focus their attention in liquid flows and their manipulation techniques for specific research in e.g. electrokinesis, mixing, dispersion and multiphase flows [Stone et al., 2004]. Microanalytical methods in microfluidics made possible to achieve high sensitivity and high resolution using small amount of sample. These initial experiment were perform mostly as a proof-of-concept as an attempt to demonstrate the efficacy of this rising discipline. It was not difficult to see the op-

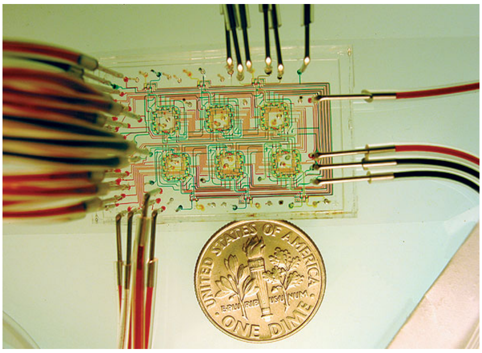

Figure 1.3: *Image of a microfluidics device used to study the growth of microbial population [Balagaddé et al., 2005].*

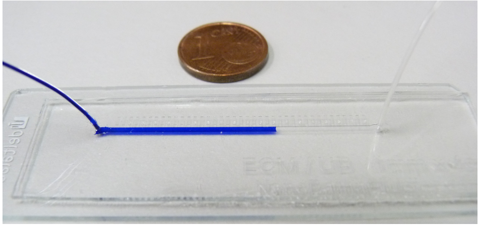

Figure 1.4: *Image microfluidic device with a rectangular microchannel fabricated in PDMS. The dimensions of the channel are: length* $L = 4\,cm$*, width* $w = 1\,mm$ *and depth* $b = 300\,\mu m$*.*

portunities given by microfluidics and be extended to other domains like bioanalyses, namely, macromolecular analyses or examination and manipulation of single cells and molecules [Beebe et al., 2002].

It was originally thought that one of the primary goal for microfluidics systems was to develop technologies that enhance the capabilities of investigators in biology and biomedical research. Taking advantage of its features: requiring small amount of sample, routine operation by untrained personnel and low cost. Currently cell biology and biology comprise most of the microfluidics research, where the main subject are diagnostic applications and manipulation of blood sample for hematology and immunology [Sackmann et al., 2014]. Is in these matters, where microfluidics methods have big advantages over traditional methods, due to its portability and rapid feedback. Even so, until now, they usually offer improvements on methods that already exist instead of new capabilities.

Fortunately, given that microscale offers unique properties that would not be achieved by macroscale devices, it is not a field to be discouraged. Clinical applications are increasing since new techniques for biofluids analyses and purification are develop [Srinivasan et al., 2004]. In the case of blood, microfluidics reduces blood processing times and decreases considerably the amount of sample needed from milliliters (from a vein) to microlitres (from a fingertip). Several advances are being performed in the field of detection and diagnostics, mostly focus to low resources locations and the diagnostic of infectious and endemic diseases as HIV [Chin et al., 2011], Malaria [Warkiani et al., 2015] or Ebola [Cai et al., 2015].

Another topic of microfluidic, LoC and μTAS applications is Point of Care Testing (POCT), which allow to perform diagnostics tests directly at the location of the patient. These devices provide rapid detection and diagnosis without the necessity of a laboratory nor an experienced technician, taking the lab itself to the patient [Sista et al., 2008]. Usually disease diagnostic used blood plasma, therefore the interest of developing devices that separate plasma from the cell fraction [Rodríguez-Villarreal et al., 2010] and perform measures of blood plasma properties, as viscosity, using microfluidics devices [Srivastava et al., 2005; Guillot et al., 2006].

Current diagnostic micro-devices focus on a targeted bio-marker to diagnose particular diseases. One of the biggest problem with blood is that is a complex fluid filled with hight number of cells, proteins, DNA and small molecules other that the targeted bio-maker, which represent noise. The idea of considering whole blood properties as a diagnostic marker would simplified the methods and enable the technology to focus on detection over sample preparation. In this matter, newer achievements using whole blood as a diagnostic tool are been reached [Toner and Irimia, 2005; Mohammadi et al., 2015].

In order to convert microfluidics in a practical and commercially successful technology it must be able to solve problems for unexperts users, making appropriate systems widely and inexpensively available. The scientific and medical communities are still in the hope of the emergence of striking applications of microfluidics, LoC and μTAS devices that would bring this technology to the common people. These applications would become a general improvement in health care worldwide.

1.3 Thesis aims and structure: Front microrheology

The aim of this thesis project was to extend the study of front microrheology though the development of a device and method that describes accurately the nonlinear rheology of biofluids, mainly blood, by means of the characterization of the fluid-air interface. We center in the fluid front (interface fluid-air) since is a direct, easy and cheap method to study fluid flows. The motivation for the study is the high relevance that blood has in disease's diagnostics and the advantages of microfluidics. We create a micro-device , Fig. 1.4, capable of describing blood viscosity and its shear thinning character. The developed method, as well, enables to establish a relation between blood viscosity and its red blood cells characteristics. The work have been mainly experimental comprising: fabrication of microfluidic devices and experiments with Newtonian and non-Newtonian fluids.

The thesis is structured in six parts. The first part contains three introduction chapters. Chapter 1 presents a background of hemorheology and microfluidics along with this thesis aims and structure. Chapter 2 describes the theoretical principles of fluid dynamics and rheometry that are relevant for our study. Last, Chapter 3 presents typical features of blood and its hemorheological properties, as well as a general view of diseases related to hemorheology and RBC's properties.

Part II describes the experimental configurations, Chapter 4 is separated in three sections. The first part presents a description of the device and a general view of its fabrication process. The second part explains the design of the experimental setup which was based on a previous work developed at the microfluidics laboratory [Queralt-Martín et al., 2011], Finally the third part is dedicated to explain the procedure to extract the data from the captured images of the fluid interface and I describe the statistical analisys of the data obtained.

To ensure that the results obtained with our device and method are accurate, before the blood testing, a characterization with Newtonian fluids needs to take place. The experiments and results for Newtonian fluids are encompassed in Part III. Chapter 5 presents the experimental results for water in various microchannels with different heights. Here it is also include the explanation of the method for the calculation of the viscosity. Chapter 6 compares water results with other Newtonian fluids, such as, Ethylene-Glycol and Blood Plasma. Last chapter dedicated to Newtonian fluids, Chapter 7, introduces a change to the system used in the previous experiments to include a second fluid, which pushes the studied fluid into the microchannel, in this case a new model for viscosity had to be developed. This three chapters are summarize in [Trejo-Soto et al., 2016a] and states our microfluidic device and method as a Viscometer.

Part IV of this thesis is dedicated to non-linear hemorheology and comprises all the results for blood. Chapter 8 is dedicated to describe the experimental protocols to measure blood in the microchannel and presents initial results for different blood samples. Chapter 9 presents the viscosity results for blood applying two different non-Newtonian fluids models: Power Law Model and Weissenberg-Rabinowitsch-Mooney correction for rheometrical measures. In the last section of this chapter, our experimental results are compare with a theoretical model which considers a shear rate that depends on the non-linear exponents for the viscosity of the blood samples. Finally, the last two chapters are dedicated to established a relation between the viscosity of the blood samples and the features of its red blood cells. In Chapter 10 we relate blood viscosity with the RBC aggregation phenomenon by means of an aggregation energy based on a Morse Potential [Trejo-Soto et al., 2016b]. Also in this chapter we established a relation is established between blood viscosity and the bending coefficient of its red blood cells membrane, for healthy and anemic blood.

Part V, is dedicated to introduce an extension to our method of optical detection. In this part, we describe the design and tests performed with an electronical detection device, which measures the velocity of the fluid. We compared the results obtained with this new electronical device with the optical tracking method presented in this thesis.

Finally, the last part is dedicated to summarized the whole thesis and presents the general conclusions and futures perspectives of this work.

CHAPTER 2

Fluid Dynamics and Rheology

The basic idea for a viscous fluid, according to Newton's words, is that the proportionality relation between the "resistance of a fluid to move" and "the velocity by which the parts of the fluid are being separated" is the viscosity of that fluid. In modern word the viscosity of a fluid is defined as the ratio between the stress at which the fluid is submitted and the shear rate between the different layers of the fluid.

The first measurements of viscosity were performed using a small straight tube or capillary. Hagen in 1839 in Germany and independently Poiseuille in 1840 in France. They both used small capillaries to measure the viscosity of water. Hagen first observed that when pressure drives a fluid through a channel, velocity is maximum at the center. The velocity gradient or shear rate and also the shear strain will be maximum at the wall and zero in the center of the flow. In 1844 Poiseuille provided the experimental results for pipe flow [Poiseuille, 1844]. Yet, it was until 1856 were Poiseuille's capillary flow data was analized to prove Newton's relation experimentally.

The CGS units for viscosity is the *Poise* $[P]$ in Poiseuille's honor. In the international units system (SI) the viscosity is measured in $[Pa \cdot s]$ where $(1\, Pa \cdot s \equiv 10\, P)$. The viscosity of water measured by Poiseuille was defined as approximately $1\, cP$ (1 centi-Poise) or $0.001\, Pa \cdot s$.

This chapter is dedicated to describe the theoretical basis to the studies that we aims in this tesis. In section 2.1 we will review the basics of hydrodynamics for viscous fluids. Section 2.2 describes the governing equation and characteristics of a fluid moving at the microscale. Section 2.3 presents an introduction to non-Newtonian fluids, their main properties and how their viscosity is measure.

2.1 Constitutive Equation for Newtonian Fluids

The most general description of the mechanical motion of an imcompressible viscous fluid is given by the Navier-Stokes equation [Guyon, 2001]:

$$\rho \left[\frac{\partial \vec{v}}{\partial t} + (\vec{v} \cdot \nabla)\vec{v} \right] = \rho \vec{f} - \nabla p + \eta \nabla^2 \vec{v} \tag{2.1}$$

Here $\vec{v} = (v_x, v_y, v_z)$ is the three-dimensional velocity field, ρ is the density of the fluid, η is the dinamic viscosity, p the pressure inside the fluid and $\vec{f}$ represent the forces applied to the fluid. This equation does not have, in general, an analytic solution.

This is mainly due to the non-linear term, $(\vec{v} \cdot \nabla)\vec{v}$. In the case of a one-dimensional flow, meaning that the velocity field of the fluid points in a single direction, the non-linear term becomes negligible. This states that when the velocity field is stationary the movement of fluid particles results from the balance between the pressure gradient and the viscous friction forces [Guyon, 2001].

In order to understand this one-dimensional stationary regime we will present three examples that are related to the work we intend in this thesis. First, we will refer to a plane Couette flow. Second, to a Poiseuille flow between to parallel plates and third a Poiseuille flow in a cilindrical tube.

2.1.1 One-dimensional Flows

A plane Couette flow is originated between to parallel plates, separated a distance b, where the upper plate moves parallel to itself at a constant velocity V, as shown in Figure 2.3 and can be written as:

$$|F_x| = |\sigma_{xz}| = \eta \frac{\partial v_x}{\partial z} = \eta \frac{V}{b} \tag{2.2}$$

A poiseuille flow is a steady state pressure driven flow. A viscous fluid flowing in between to parallel plates separated a distance b from each other, can be describe as a Poiseuile flow between two parallel plates and it is written as:

$$Q = \frac{\Delta P}{12\eta} \frac{b^3}{L} \tag{2.3}$$

In a cilindrical tube, a Poiseuille flow states that the velocity profile of a flow moving inside a tube of radius r has a parabolic shape, as shown in Figure 2.2. It is traditionally written as:

$$Q = \frac{\Delta P}{8\eta} \frac{\pi r^4}{L} \tag{2.4}$$

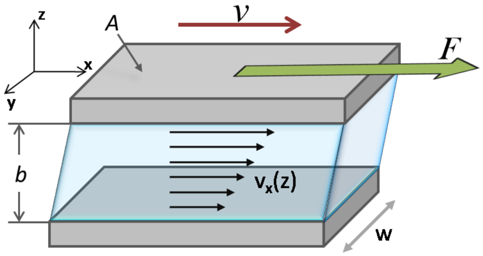

Figure 2.1: *Schematic of a plane Couette Flow that describe the velocity gradient or shear rate,* $\dot{\gamma}_{xz} = \frac{dv_x}{dz}$*, of a steady shear flow. In this case the ratio* $\frac{b}{w} << 1$.

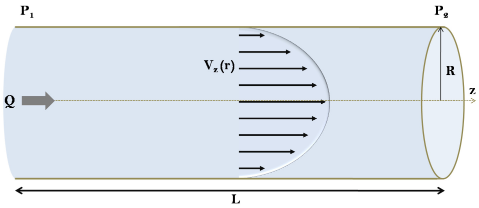

Figure 2.2: *Schematic representation of Poiseuille Flow in a cylindrical tube of radius R. The velocity* $V_z(r)$ *of the flow* Q *in the direction* z *is represented by the arrows of the flow profile. The pressure difference is* $\Delta P = P_2 - P_1$.

The Newtonian constitutive equation states that the stress is proportional to the velocity gradient[Bird et al., 1987; Larson, 1999]. If we define the velocity as $\vec{v} = (v_x, v_y, v_z)$, the **stress tensor**, σ, and the velocity gradient tensor, also know as, **shear rate tensor**, $\dot{\gamma}$, are defined respectively as:

$$\sigma = \begin{pmatrix} \sigma_{xx} & \sigma_{yx} & \sigma_{zx} \\ \sigma_{xy} & \sigma_{yy} & \sigma_{zy} \\ \sigma_{xz} & \sigma_{yz} & \sigma_{zz} \end{pmatrix} \tag{2.5}$$

$$\dot{\gamma} = \nabla\vec{v} = \begin{pmatrix} \frac{\partial v_x}{\partial x} & \frac{\partial v_y}{\partial x} & \frac{\partial v_z}{\partial x} \\ \frac{\partial v_x}{\partial y} & \frac{\partial v_y}{\partial y} & \frac{\partial v_z}{\partial y} \\ \frac{\partial v_x}{\partial z} & \frac{\partial v_y}{\partial z} & \frac{\partial v_z}{\partial z} \end{pmatrix} \tag{2.6}$$

The simplest situation to describe their relation is the simple shear flow or plane Couette Flow. Fig. 2.3 shown an schematic general representation of this type of flow. Here we consider a flow between 2 planes, a fix lower plane at $z = 0$ and an upper plane at $z = b$ moving at a constant velocity v in the x direction. In this case the only non-zero velocity component of the shear rate tensor is v_x and it varies in the z direction. Fig. 2.4, show the effect of the stress tensor over a volume differential of the moving flow. The simplest state of the stress is in which the fluid element is only under hydrostatic pressure and in this case $|\sigma| = -P_{hyd}$.

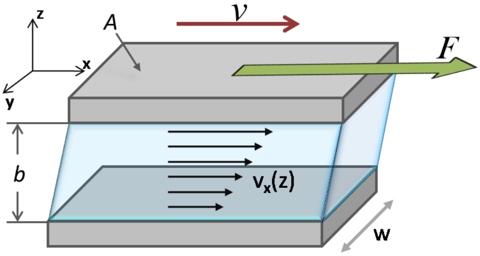

Figure 2.3: *Schematic of a plane Couette Flow that describe the velocity gradient or shear rate,* $\dot{\gamma}_{xz} = \frac{dv_x}{dz}$*, of a steady shear flow. In this case the ratio* $\frac{b}{w} << 1$.

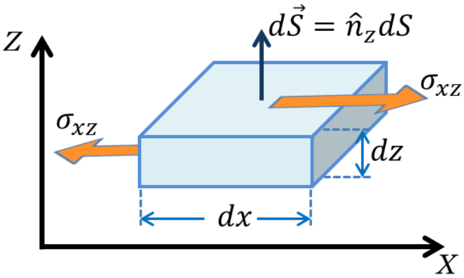

Figure 2.4: *Schematic of the stress tensor over a volume differential. Here the only surviving component is in the* x *direction,* $\sigma_{xz} = \Delta P$.

Under these conditions the stress tensor and the shear rate tensor are simplify and equations (2.5) and (2.6) are reduced to:

$$\sigma_{xz} = \frac{F}{A} = \Delta P \tag{2.7}$$

$$\dot{\gamma}_{xz} = \frac{\partial v_x(z)}{\partial z} \tag{2.8}$$

2.2 Microfluidics

In microfluidics the fundamental physics changes as the size scale decreases. Small dimensions in fluid dynamics repress inertial nonlinearity eliminating instabilities and turbulence typical in several macro-scaled systems [Squires and Quake, 2005; Tabeling, 2010]. In miniaturized fluidic systems several phenomena active in normal scale, such as gravity, are reduce, while others as capillary forces and surface tension, become relevant.

Fluids physics is determined by adimensional numbers which define flows behavior such as Reynolds number, which relates inertial forces to viscous forces, or Capillary number, relating viscous forces to surface tension. Both numbers are of mayor importance to define microfluidic systems.

The Reynolds Number is defined as a function of the density ρ and the shear viscosity η of a fluid, as well as its velocity v inside a tube of diameter D, the relation is written as:

$$Re = \frac{\rho v D}{\eta} \tag{2.9}$$

At the microscale the values of D and v are in the order of $10^{-4}\,(m)$, and considering water as the typical calibration fluid, the value of the Reynolds Number is $Re \approx 10^{-2} << 1$. This low value confirms the linearity of flows at the micro-scale, eliminating the nonlinear term in the Navier-Stokes equation, eq. (2.1). The resultant equation is called the Stokes equation and is may be written as:

$$\rho_f \frac{\partial \vec{v}}{\partial t} = \rho_f \vec{f} - \nabla p + \eta \nabla^2 \vec{v} \tag{2.10}$$

2.2.1 Darcy Law at the micro-scale

Lets consider a micro-scaled system, where a fluids moves along a rectangular microchannel of width w and height b, with an aspect ratio $b/w << 1$. Fig. 2.5 shows an schematic representation of the system described.

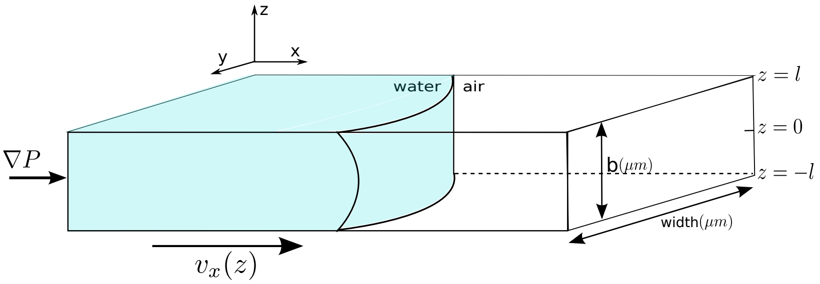

Figure 2.5: *Schematic representation of a fluid interface moving through a microchannel of width w and height b. Here ∇P is the pressure gradient, $v_x(z)$ is the velocity of the fluid interface.*

Starting from the Stokes equation, eq.(2.10) and considering a stationary regime $\frac{\partial v}{\partial t} = 0$, we have:

$$\eta \nabla^2 v = \nabla p_x \tag{2.11}$$

Integrating twice equation (2.11) with respect to z with the boundary conditions $v\,(z = \pm l) = 0$ we obtain:

$$\eta \int \frac{\partial^2 v(z)}{\partial z^2} dz = \int \nabla p_x dz \tag{2.12}$$

$$v_z = \frac{1}{2\eta} \nabla p_x \left(z^2 - l^2\right) \tag{2.13}$$

Here eq. (2.13) describes the velocity profile of the fluid inside the microchannel.

Since we are not interested in describing the velocity profile, instead we calculate the mean velocity of the interface, through the whole height b of the microchannel, from $z = -l$ to $z = l$.

$$\langle v \rangle = \frac{1}{2\eta} \nabla p_x (\langle z^2 \rangle - l^2) \;\; \text{with} \;\; \langle z^2 \rangle = \frac{l^2}{3} \tag{2.14}$$

$$\langle v \rangle = \frac{b^2}{12\eta} \nabla p_x \tag{2.15}$$

The pressure gradient can be expressed as $\nabla p_x = \frac{\Delta P}{h}$, where h is the position of the fluid interface inside the microchannel and equation (2.15) is expressed as:

$$\langle v \rangle = \frac{b^2}{12\eta} \frac{\Delta P}{h} \tag{2.16}$$

Equation (2.16) can be re-written to an expression that describes the viscosity of a fluid flowing in the confined microchannel schematicly represented in Fig. 2.5. This expression is known as the Darcy Law and is represented as:

$$\eta = \frac{b^2}{12\langle v \rangle} \frac{\Delta P}{h} \tag{2.17}$$

2.3 Non-Newtonian Fluids: front microrheology

Based on Poiseuille studies, several researchers used his design to study a wide variety of fluids. They soon found that many colloidal suspensions and polymer solutions did not obey this simple linear relation. This unusual behavior was first observed in early 1900's and Eugene Bingham used the name rheology to refer to it. Rheology is now recognized as a specialized part of fluid mechanics and is concerned mainly with non-Newtonian and viscoelastic substances.

A Newtonian liquid is one in which the viscosity, at fixed temperature and pressure is independent of the shear stress, fluids as water or honey are Newtonian. A non-Newtonian fluid is one in which the viscosity depends on the shear stress, fluids with complex micro-structures, e.g., suspension of particles or polymer melts exhibit a wide variety of behaviors and are non-Newtonian.

When a steady flow is established, for Newtonian fluids, the viscosity, η, is constant and depends only on the temperature. The viscosity is then defined as the ratio between the shear stress, σ, and the shear rate, $\dot{\gamma}$, as:

$$\eta = \frac{\sigma}{\dot{\gamma}} \tag{2.18}$$

In the case of non-Newtonian fluids, this condition does not sustain and in some cases the viscosity is a decreasing function of the shear rate, this type of behavior is called **shear thinning**. The opposite behavior is known as **shear thickening**.

2.3.1 Power Law model for non-Newtonian Fluids

The Power Law Model, also known as, Oswaldt-de-Waele Model is one of the simpler models to describe de viscosity behavior of non-Newtonian fluids. It states that the viscosity of the fluid depends on the shear rate following a power law described by:

$$\eta(\dot{\gamma}) = m\dot{\gamma}^{n-1} \tag{2.19}$$

The velocity profile of a flow inside a Hele-Shaw cell (a rectangular canal with high aspect ratio between width and depth) may be written only on the direction of the flow as $\vec{v} = (v_x(z), 0, 0)$ where the shear rate is defined as the velocity gradient of the flow, equation 2.20:

$$\dot{\gamma} = \frac{\partial v_x}{\partial z} \tag{2.20}$$

2.3.2 Rheometry

A **rheometer** is an instrument that measures stress and deformation history of a material which rheological constitutive equation is unknown. A **viscometer** is a special type of rheometer which can only measure the steady shear viscosity function of a material [Tropea et al., 2007]. Rheometers may be differentiate on the type of induce flow between drag flows and pressure-driven flows. Typical drag flow rheometer are the coaxial cylinder Couette flow and coaxial Cone-Plate, while capillary rheometers are pressure-driven, see Fig. 2.6. I will center in this section on the pressure-driven capillary rheometer basis since it is this kind of rheometer that we intend.

A capillary rheometer is a pressure driven flow device which can only measure the steady shear functions of the flow. This devices are widely used since they are relatively inexpensive to build and simple to operate. Capillary rheometers are close devices so they can eliminate solvent evaporation and other problems that plague rotational devices with free surfaces [Pipe and McKinley, 2009].

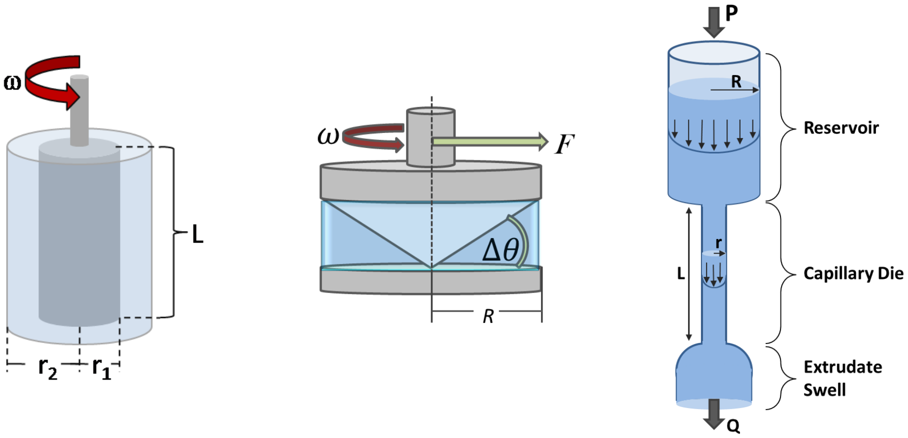

Figure 2.6: *Schematic representation of different types of rheometers. Presented from left to right: coaxial cylinders Couette flow, coaxial Cone-plate and cylindrical capillary rheometers*

The capillary was the first rheometer and this type of devices remain the most common method of measuring viscosity. The basics features of this instrument are shown in Fig. 2.6. The pressure on the test fluid in a reservoir may be generated by gravity, compressed gas or as piston. A capillary is connected to the bottom of the reservoir, where the pressure drop and the flow rate through this capillary are used to determine the viscosity.

In capillary rheometry there are several features to take into account. The flow properties need to be:

- Laminar Flow
- Isothermal
- No wall slipagge
- Velocity distribution is distributed along the radius direction.
- Incompressible material

In the case of a cylindrical capillary we may define a wall shear stress, σ_w, due to pressure difference and a wall shear rate, $\dot{\gamma}_w$. In the case of a Newtonian fluid this quantities define the viscosity of a fluids by mean of equation:

$$\eta = \frac{\sigma_w}{\dot{\gamma}_w} \tag{2.21}$$

The wall stress and shear rate definitions in eq. (2.21) will depend on the geometry and the characteristics of the capillary.

In the case of non-Newtonian fluids the wall shear rate can be affected by a wall slip which will cause the instrument to measure a higher than expected shear rate. Also corrections on the flow profile in the capillary need to be taken into account.

The Weissenberg-Rabinowitsch-Mooney correction of Newtonian v/s non-Newtonian behavior [Macosko and Larson, 1994] defines the viscosity through a so called ”true” shear rate, $\dot{\gamma}_t$, which is defined as a function of the wall shear rate as:

$$\dot{\gamma}_t = \frac{1}{4}\dot{\gamma}_w \left[3 + \frac{d\,lnQ}{d\,ln\sigma_w}\right] \tag{2.22}$$

Here Q is the flow rate of the fluid inside the capillary which is easy calculated trough the velocity of the fluid front.

CHAPTER 3

Blood

Blood circulation plays an fundamental role in maintaining an appropriate environment in all the body tissues and keep the optimal function of cells. Therefore, a key aspects in circulation is the understanding of flow properties of blood. These properties depend on the composition of blood and the particular properties of its constituents. Blood is known to be a complex mixture of blood plasma and blood cells. It is recognize to present a non-Newtonian behavior even if blood plasma behaves as a Newtonian fluids by itself. The study of blood flow can be approach from two points of views. First, we can study the fluid dynamics of the blood flow as a steady fluid and second we can study the flow properties and rheology of blood and its components.

This chapter is dedicated to describe the general features of blood, its properties and how these relate to diseases. First we review the composition of blood and why it affects its behavior. In section 3.2 we reefer to the past and current studies of the characteristics of blood flow at the microscale. Section 3.3, describes blood rheology (hemorheology), mainly the behavior of its viscosity. The last section is dedicated to describe our interest in hemorheology exposing its high importance in the diagnostic of diseases related to blood viscosity.

3.1 Blood Components

Human Blood is a two-phase fluid system and consists mainly of an aqueous polymeric and ionic solution of low viscosity, the plasma, in which is suspended a 0.45-0.50 concentrated cellular fraction. The plasma is a liquid phase mixture of metabolites, proteins and lipoproteins suspended in a salt solution composed mostly of water. The cellular fraction is a complex mixture of mainly erythrocytes, commonly known as red blood cells, but it also contains leukocytes (white blood cells) and trombocytes (platelets). Nearly a 99% of the cellular fraction in blood is represented by red blood cells. The complete set of blood components is usually referred as whole blood.

Plasma proteins play a important role on the hemorheological properties of whole blood. First, because even though blood plasma is $\approx 92\%$ water, its viscosity at $37°C$ is nearly twice the viscosity of water at the same temperature and this is due mainly to plasma proteins. Second, plasma proteins (especially fibrinogen) causes red blood cells to stick together forming aggregates, like piles of coins, known as rouleaux. Rouleaux formation is important because it causes the viscosity of blood to be very dependent on the shear rate to which it is exposed [Lowe et al., 1988].

The erytrocytes volume fraction on a blood sample is commonly referred as hematocrit. The normal range of hematocrit differs between men and women and it is 40 to 50% and 36 to 46% respectively. Leukocytes and trombocytes together only comprise about 1% of the cellular fraction [Baskurt, 2007]. This high concentration of RBC's is the main reason that they are hemorheologically important, though physical and morphological properties of them also contribute to blood behavior.

Human red blood cells have an unusual shape, this particular morphology may be appreciated in Fig. 3.1. They are anucleate biconcave discs of about $7.8\,\mu m$ diameter and a thickness of $2.5\,\mu m$ at the thickest point and $1\,\mu m$ or less in the center [Hall, 2010], this gives them the capacity to align with the direction of flow. The cellular membrane of a healthy RBC is flexible, which means, that it can change its shape and deform under different conditions. This is due to the elastic properties of its bilayered composition and cytoskeleton. They also have the, previously mentioned, tendency to adhere together forming aggregates, also referred as rouleaux, this aggregates formation are shown in Figs. 3.2 and 3.3. Last, they contain an hemoglobin solution of high concentration which affects the speed at which they deform [Dacie et al., 2002]. All these properties of red blood cells act together to give blood a viscosity substantially higher than blood plasma and contribute to its non-Newtonian properties.

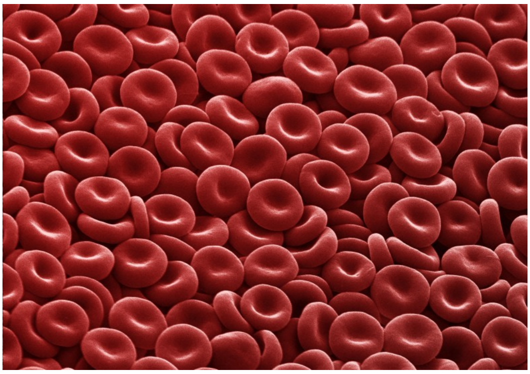

Figure 3.1: *Photograph of Red Blood Cells. In this picture we can appreciate their biconcave disc shape. Credits: Annie Cavanagh available under Creative Commons by-nc-nd 4.0 from http://wellcomeimages.org/.*

On the other hand, white blood cells and platelets hemorheological role is less significative, mainly due to its low concentration in blood in comparison with red blood cells. Even though white blood cells are bigger in size and present viscoelastic properties by themselves, they play an important role in micro-circulation resistance. However since its volume concentration is aproximatelly three orders of magnitude lower than red blood cells, its effects are less relevant in general circulation. In the case of platelets, they are much smaller than RBC's $(2-4\,\mu m)$ and their volume in blood is even smaller than the leukocytes concentration. In consequence, they neither influence whole blood viscosity nor micro-vascular resistance.

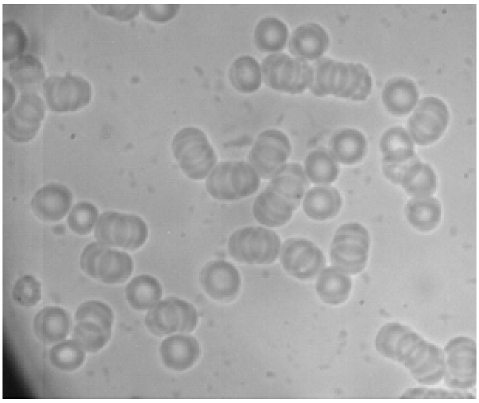

Figure 3.2: *Unaggregated Red Blood Cells of a 1 day old blood sample of a 48% hematocrit. We may appreciate the discocyte morphology of RBC's. Since the sample is at rest we also see a tendency to aggregate. The image was taken with an inverted microscope Optika XDS-3 and a* 100× *objective.*

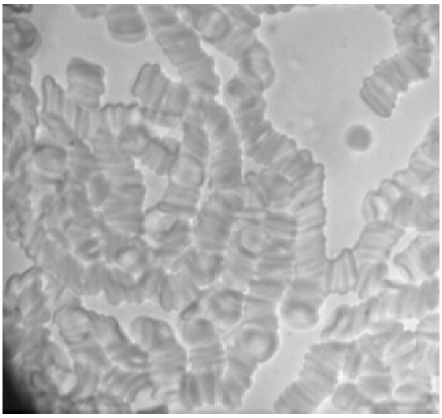

Figure 3.3: *Aggregated Red Blood Cells of a 5 days old blood sample of a 48% hematocrit. The image was taken with an inverted microscope Optika XDS-3 and a* 100× *objective.*

3.2 Hemodynamics

The study of the fluid dynamics of blood flow is called hemodynamics. Hemodynamics research has a long history and the field continues to expand due to recent advancements in numerical and experimental techniques at the microscale. It is an attractive topic where several theoretical, experimental and computational studies have been developed in the past 50 years [Omori et al., 2015]. In micro-vessels over $200\mu m$ diameter it can be assumed that blood is an homogeneous continuous fluid. This assumption is not true for smaller micro-vessel and here the individual motion of red blood cells becomes important.

In most computational studies shear rate is normalized by an adimensional quantity, which expresses the ratio between the viscous stress of the fluid and the elasticity of the membrane of its suspended cells. This adimensional quantity is usually defined by the viscosity of the liquid surrounding the cells, the characteristic length of a cell, the shear rate and a parameter related to red blood cells properties (elasticity, deformability, aggregation). Several computational techniques have been reported to model blood flows and single cellular RBC mechanics, such as finite element method (BEM) [Peng et al., 2014], lattice-Boltzmann method (LBM) [Gompper et al., 2008; Lázaro et al., 2014a,b; Pontrelli et al., 2014], dissipative particle dynamics (DPD) [Fedosov et al., 2011; Lei et al., 2013].

From and experimental point of view early hemodynamical experiments only provided a qualitative understanding of blood flow. Quantitative information, such as rheological effects and blood cell deformability were difficult to obtain due to lack of time and spatial resolution. Eventually, high speed and high resolution cameras with an enhanced sensitivity and mounted to an optical microscope enabled velocity measurements of such small scale flows. In this aspect, several techniques have been developed to measure the velocity fields at the microscale such as μPIV (micro-particles image velocimetry) [Santiago et al., 1998; Degré et al., 2006] or PTV (particle tracking velocimetry) [Meinhart et al., 1999].

Even thought this velocity measuring techniques have been successful [Sugii et al., 2005; Nghe et al., 2008; Kikuchi and Mochizuki, 2011; Pitts and Fenech, 2013], they present several issues, such as, the selectivity of tracer particles and the difficulties to label cells. The μPIV tecnique also has a limited spatial resolution due to the diffraction limits and the size of the particles must be at least 100 times smaller than the diameter of the micro-tubes [Wereley et al., 1998], otherwise affects the traceability of the blood flow around it and changes the viscosity of the fluid. Although these issues has been corrected the main disadvantages that this techniques have is that they are very expensive to acquire and require specific infrastructures, that usually are difficult to achieve.

3.3 Blood Rheology

The rheometrical properties of blood have been studied many years and has been clearly demonstrated that blood has a shear thinning behavior, which means, that the viscosity of blood is high at low flow velocities, but as the velocity of the flow increases, its viscosity value decreases. [Cokelet et al., 1963; Merrill, 1969; Chien, 1970; Thurston, 1972]. Some typical values for the viscosity of healthy blood at low shear rate ($0.277\,s^{-1}$) are $39 \pm 4\,mPas$ for females and $48 \pm 6\,mPas$ for males. At high shear rates ($128\,s^{-1}$) the viscosity values are $4.3 \pm 0.2\,mPas$ and $4.7 \pm 0.2\,mPas$ respectively for females and males [Baskurt, 2007].

Two properties of red blood cell are particularly important to understand this behavior: their tendency to form aggregates or rouleaux when at rest and their deformability [Chien et al., 1970b; Rampling, 1990; Ivlev et al., 2007; Kaoui et al., 2009]. This causes highly non-Newtonian behavior observed with red blood cell suspensions in plasma. At low shear rate the viscosity of blood is high, whereas, at high shear rate red cell disaggregation and deformation reduces the viscosity of blood, a schematic representation of this situation is shown in Fig. 3.4.

From a macro-rheological point of view, it is widely known that the viscosity of blood also increases with hematocrit [Pries et al., 1992; Eckmann et al., 2000]. Given the particular properties of RBC's the increase or decrease of its concentration on plasma will affect the behavior of blood. It affects its viscosity values as well as its Non-Newtonian behavior which is lost at low hematocrit. This effects from hematocrit have been widely studied and are shown in Fig. 3.5 [Baskurt, 2007].

Red blood cell aggregation is fundamental for the Non-Newtonian behavior of blood but it originates complications when using a viscometer. One of this complications is a phenomenon called red blood cells syneresis which is due to the internal movement of red blood cells as they aggregate, leaving layer of low cells concentration at the wall of several kind of viscometers (or rheometers). This effect becomes impor-

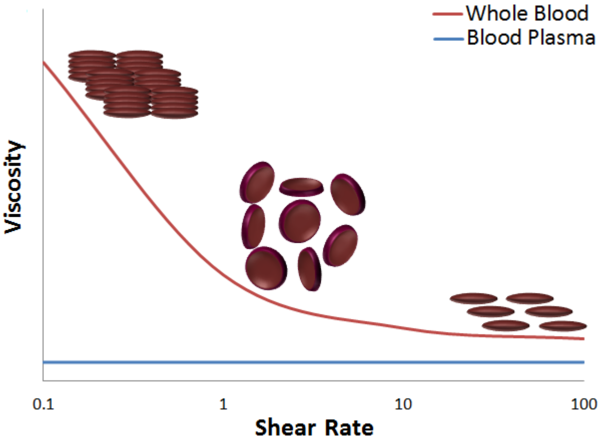

Figure 3.4: *Schematic representation of red blood cells and blood viscosity as a function of shear rate. At rest or at low shear rate Red Blood Cells form aggregates which are responsible for an increase value of viscosity. As the shear rate increases cells disaggregate and move freely through blood vessels. If the shear rate keep increasing RBC's deform, elongate and align with the direction of the flow, which happen in micro-capillary vessels.*

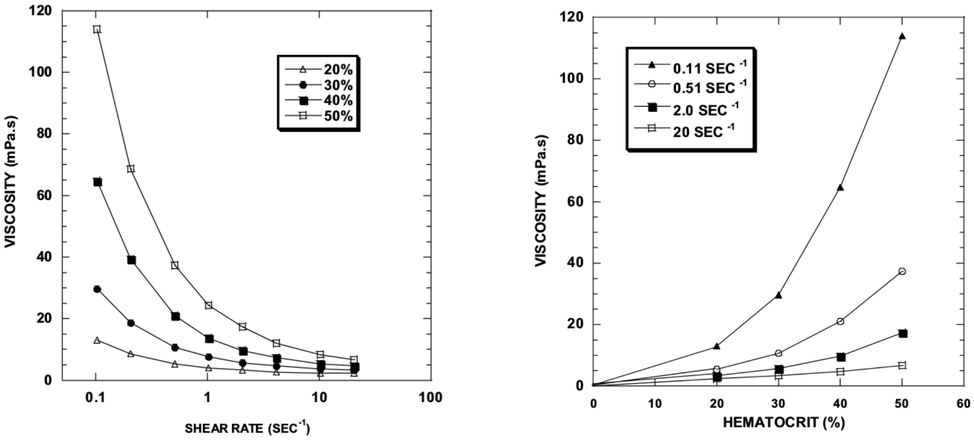

Figure 3.5: *The figure on the left shows the value of blood viscosity as a function of the shear rate for different hematocrit. The figure on the right shows the viscosity as a function of the hematocrit for different values of the shear rate. From the left image we may inferred the shear thinning behavior of blood since the viscosity value decreases as the shear rate increases, we may also observed how this shear thinning becomes less noticeable as the hematocrit decreases. The right side image clearly show the dependence of blood viscosity on the hematocrit [Baskurt, 2007].*

tant when performing measures at low shear rates ($< 1\,s^{-1}$) and may lead to inaccurate results regarding blood rheology. Syneresis is not to be confused with red blood cell sedimentation which is the tendency of RBC's in suspension to settle against a surface due to gravity. Both phenomena have similar consequences but their cause is different.

Either way both behaviors (syneresis and sedimentation) become important when using Cone-plate, Couette or Capillary viscometers.

When blood measures are transported to the microscale other effects may be observed, namely, the Fåhraeus and the Fåhraeus-Lindqvist effects. Both effects have been reported in tubes with a diameter of less than $300\,\mu m$. In the first case, is found that to achieve a steady flow the hematocrit in the reservoir is higher than the hematocrit inside the tube, where cells move towards the central region of the tube as they flow downstream [Fåhræus, 1929]. The second effect is observed at fast flow rates, which do not allow enough red cells aggregation, in this case the viscosity of blood depends on the tube diameter [Fåhræus and Lindqvist, 1931].

An additional rheological characteristics is present in blood as it exhibits yield stress. This means that if the stress is kept lower than a critical value, σ_Y, no flow will occur. However, if the stress threshold is exceeded, a steady flow is established. This behavior is due to cell aggregation, at rest aggregated cell with plasma form a sort of gel which is broken under specific flow conditions and becomes a suspension of individual cells in plasma as the shear rate increases. Early studies have obtained yield stress values by means of extrapolation from the relation between the stress applied and the shear rate response using Couette and Capillary rheometers [Chien et al., 1966]. Other have been able to obtained this values using other techniques which allow accurate measures of stress at low shear rate [Magnin and Piau, 1990; Picart et al., 1998]. Since the critical values of yield stress is low ($\sigma_Y \approx 100\,mPa$) its effects at shear rates higher than $\dot{\gamma} = 10^{-2}\,s^{-1}$ may be neglected.

In general, blood rheology has been proved to be experimentally difficult to measure and its results frequently led to inappropriate interpretations [Thiébaud et al., 2014]. Many new techniques and more advances artifacts have been able to reduced this problems. Still, many considerations need to be taken in order to obtain feasible results and will condition the design of devices and the characteristics of experimental set-ups.

3.4 Hemorheological Pathologies

As mention in previous sections, human blood is an unusual fluid. While blood plasma alone behaves as a simple Newtonian fluid, the complete set of blood components are Non-Newtonian, meaning that, its viscosity varies according to the speed at which is set in motion. This characteristics tell us two important issues in clinical hemorheology. The first is that in vitro measurements of the viscosity of plasma alone never reflects the totality of events occurring in vivo in patient circulation. The second is that the cellular elements, by acting as particles in suspension, are mainly responsible for the non-Newtonian behavior of blood [Leblond, 1987]. This is why instead of considering only abnormal plasma proteins in diseases we should also consider the rheological abnormalities of red blood cells.

Since plasma proteins are responsible for the elevation of blood plasma viscosity in comparison to water, a change in their composition may as well alter the hemorheological properties of blood. Some diseases as Wasldenstrom's macroglobulinaemia generates an uprise in macrogobulins that increase the viscosity of blood plasma. Furthermore, in this condition proteins become more susceptible to form rouleaux which increase blood viscosity at low shear rate. An increase in plasma fibrinogen concentration generates an abnormal increase of RBC's aggregation, changing the rheological behavior of blood, this has been observe in diseases associated with vascular disorders as diabetes mellitus [Cho et al., 2008], hypertension[Letcher et al., 1981] or coronary slow flow [Bilgi et al., 2012], this last one even referred as a rheological disease.

Although plasma affects blood rheology, red blood cell are the most prominent hematological factor influencing hemorheology. Among circulating red blood cells, erytrocytes interact most significantly with plasma, mainly as a function of the hematocrit. However, RBC's have physical properties of their own capable of directly influence blood flow regardless of hematocrit, hence the importance of taking RBC's properties into account when studying its effects on diseases that affects whole blood viscosity.

Most typical diseases related to blood viscosity are related to its percentage of red blood cells concentration (hematocrit), as anemia (low % hematocrit) or polycythemia (high % hematocrit). Others like sickle cell anemia, alfatalasemia or malaria are directly related to red blood cell elasticity, deformation or aggregation properties.

Hyperviscosity and Anemia

The elevated values of blood viscosity, characterizing hyperviscosity syndromes may occur due to different factor in the properties of blood: an increase in the viscosity of blood plasma, high production of fibrinogen, increased numbers of cells (polycythemia or leukemia) or to increased resistance of cells to deformation (sicklemia or spherocytosis). In the case of whole blood viscosity the most influential factor to increase its viscosity is the hematocrit. If the hematocrit of blood exceeds 65%, which is the case of polycythemia [Sarkar and Rosenkrantz], various rheological abnormalities arise, i.e, the sedimentation rates decreases significantly as a result of red blood cells crowding, as well as, the elasticity and deformation of red blood cells becomes more relevant to achieve smooth driven flows, otherwise, micro-circulation may be severely compromised.

On the other hand, a decrease in the hematocrit as in the case of anemic blood, hematocrit lower than a 30%, neglect almost every Non-Newtonian characteristic and usually displays a Newtonian behavior. The yield stress is almost non-presents and no important rheological changes may be appreciated, unless in special cases of anemia where cell properties are altered.

Red Blood Cells related diseases

Some diseases, such as Diabetes Mellitus, Malaria or Sickle Cell Anemia are directly related to changes in red blood cells elasticity and deformability. Malaria, for example, affect directly the membrane elasticity of red blood cells making them stiffer than normal cells [Hosseini and Feng, 2012] affecting the hemodynamical properties of the blood flow [Dondorp et al., 2000; Imai et al., 2010; Wu and Feng, 2013]. In the case of Sickle Cell Anemia, red blood cells have a unusual shape and are referred as irreversibly sickle cells (ISC) which are stiffer and less deformable than normal cells, furthermore, ISC are unable to aggregate. Due to the presence of ISC, in oxygenated conditions, the ”htc/viscosity” ratio is lower than for normal blood samples [Chien et al., 1970a; Connes et al., 2015]. If the natural hematocrit of the sample is raised to typical hematocrit of unanemic blood a rise on the viscosity is observe at all shear rates. Plasma viscosity of subject with sickle cell anemia is also higher than the viscosity of healthy subjects. In severe cases ISC’s obstruct micro-vessels altering normal circulation of blood [Ohene-Frempong et al., 1998].

Studies and devices in microfluidics, have been evoked to study cell properties individually but not many have focus on understanding its behavior as a whole suspension. Early cited studies of blood viscosity were mostly qualitative. Lately, new interest is uprising in the study of blood rheology related to individual properties of red cells as physical bio-markers. Moreover, it is simpler and cheaper to study experimentally blood as a continuous fluid instead of individual cells, since a more advance technology is required in this last case.

PART II

Experimental Set Up

CHAPTER 4

Experimental Setup and Method

As mentioned in the introduction part, there are several method to study the dynamics of blood flow and the rheology of blood. In this last matter, the macro-scale provides several type of rheometers to measure the properties of blood, but these equipments usually require high amounts of sample which is difficult to acquire. Moreover, some equipments deliver inaccurate results due to blood properties.

The microscale displays good advantages in this matter since the amounts of sample to perform a measure is not higher than $100\,\mu l$. Additionally, microdevices are suitable to study the hemodynamics of micro-circulation, but some of the current method (μPIV or PVT) are expensive and required techniques which are not always available. In order to simplify the study of hemodynamics, we have developed a simple microfluidic device and method which allow us to determine the velocity of a fluid interface using basic equipments.

This chapter is dedicated to explain our experimental setup and describe the method that we have develop to measure and control fluids flow. Section 4.1 is dedicated to describe the microfluidic device and refers in general to its fabrication. Section 4.2 presents a description of the experimental setup and the procedure to obtain the images of a fluid-air interface moving inside the microchannel. Section 4.3 explains how the images are analized to obtain the data of the position and velocity of the fluid front using a particular computational code.

4.1 The Microfluidic Device

The main objective of the design of the microfluidic device was to develop a small, simple, single channel gadget which allows to capture the movement of a fluid-air interface across the channel length, using simple optical equipment. The features of the device must allow the fluid to enter the microchannel by means of a constant pressure difference, ΔP, exerted by a column of fluid submitted to atmospheric pressure.

4.1.1 Description of the Device

We have developed a rectangular microchannel, of width $w = 1\,mm$, length $l_c = 4\,cm$ and various heights between $b = 350$ and $b = 50 \pm 9\,\mu m$, molded in a biocompatible hydrophobic silicone, poly(dimethylsiloxane) PDMS, on a glass substrate of $2.5 \times 7.5\,cm^2$. The bottom surface of the microchannel is made of glass and the top and lateral surfaces are made of PDMS. The inlet and the outlet are perpendicular holes set at each extremity of the channel which permit the entrance of the fluid and air, Figure 4.1 shows an schematic view of the microchannel.

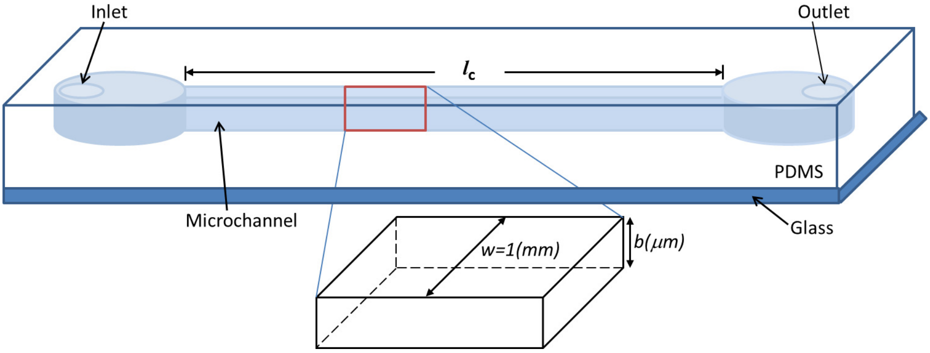

Figure 4.1: *Schematic representation of the device containing the rectangular microchannel. Microchannel features are length* $l_c = 4cm$*, width* $w = 1\,mm$ *and height* $b\,\mu m$*.*

The microchannels are fabricated according to Replica Molding technique [Xia et al., 1997; McDonald and Whitesides, 2002; Qin et al., 2010], which is an easy and low cost manufacturing method. This method consist of a PDMS replica of a photolythographic mold [Moreau, 2012; Rodríguez Villarreal, 2011] so-called master, made of SU-8 aqueous photoresist or Ordyl SY300 dry film photoresist with a printed relief pattern. Liquid PDMS is poured over the master and when it solidifies the relief is printed on it. After peeling, the solid PDMS from the master is placed over a glass substrate leaving an air cavity which is known as the microchannel. A photograph of the device containing the microchannel is shown in Figure 4.2.

Several methods and designs were use until we obtained the desired features of the channel. For the design, we started with channels of $l_c = 2\,cm$ which were later extended to $l_c = 4\,cm$ to observe a broader behavior of the front. Our first designs had a $5\,mm$ diameter pool, which was later eliminated since it presented difficulties for cleaning and drying the channel. We also added to the design small structures of $500\,\mu m$ length separated $500\,\mu m$ to identify the position of the channel where the measure was being performed. The design masks were developed using a computer application for creating two-dimensional vector graphics called Macromedia Free Hand MX. The masks are printed with a high resolution printer on an acetate sheet.

For the fabrication trials and protocols, we tested channels of $b = 300\mu m$ using SU-8 1150 resin useful to achieve high molds [MicroChem, 2011]. We later change to Ordyl SY355, which was easier to manage and featured very homogeneous heights along the channel [ElgaEurope, 2012; Rigat-Brugarolas et al., 2012; Vulto et al., 2005]. Another advantage of this dry film photoresist was that it allowed us to fabricate molds of several heights by simply adding layer of $55\mu m$. All the fabrication process of microchannels, Photolithography and Replica Molding, was developed at the Clean Room of the Facultat de Física of the Universitat de Barcelona.

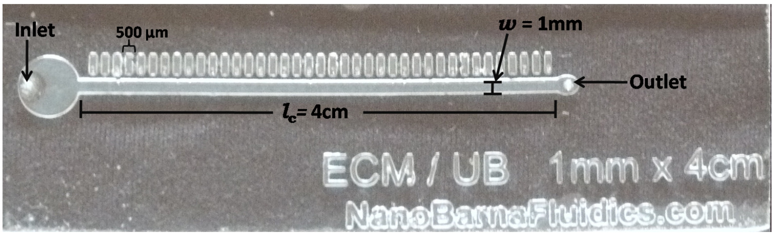

Figure 4.2: *Real image of the device containing the microchannel with length* $l_c = 4\,cm$ *and width* $w = 1\,mm$.

4.1.2 Fabrication of the Devices

The whole fabrication process consists in several steps. The process starts with the cleaning of the glass substrates which are rinsed with Acetone, sonicated with Ethanol for 3 minutes and then rinsed with de-ionized water (DI water). The substrates are dried with nitrogen and then placed on a hot plate at $100°C$ to dehydrate the surface. Finally the substrates are exposed to plasma cleaning for 30 minutes to eliminate residues of the organic solvents. The different steps of the fabrication process are explained in general below and shown schematically in Figure 4.3. Details on the fabrication process are described in Appendix A.

1. **Coating**: The coating process depends on the photoresist used to fabricate the master. In the case on SU-8 (section A.2.2) the substrate is homogeneously covered with resit and then spun at tabulated revolutions per minute, depending on the expected height. In the case of Ordyl (section A.2.3), a polyethylene cover protecting the resist is extracted and the sheet of Ordyl is extended over the substrate, avoiding the formation of bubbles and wrinkles. Then it is passed through a hot laminator to secure good adhesion to the surface. Before exposure to UV light, the coated substrate (wafer) with SU-8 is submitted to $65°C$ to eliminate solvents and later to $95°C$ to cure and harden. Ordyl does not need this procedure and may be expose immediately after coating.

2. **Exposure**: Once the SU-8 photoresist has hardened or all the Ordyl layers have been placed, the obtained wafer is cover by the mask with the printed design and expose to UV light. The resist in contact with light polimerizes and get attached to the substrate. After the exposure a Post Exposure Bake is performed for SU-8 photoresist at $95°C$ for approximately 20 minutes. For the Ordyl photoresist a PEB of no more than 10 second is performed.

3. **Develope**: Each resist has its own chemical developer. The wafer is immerse on the developer and in some cases submitted to agitation to increase dissolution rates of the unexposed photoresist. Once the relief of the channel is visible and all the unexposed resist is dissolved, the master is rinsed with isopropyl and dried with nitrogen. Both photoresist master are placed in an oven for 60 minutes at $150°C$ to secure the adhesion of the master to the glass substrate.

4. **Pouring of PDMS**: Once the master is well attached to the substrate, liquid pre-polymer PDMS is poured over, which conforms to the shape of the master and replicates the features of its design with high fidelity. The PDMS mixture is degassed inside a vacuum pump to eliminate the bubbles that appear during its preparation and pouring. Once the PDMS is completely degassed, it is set to cure in an oven at $65°C$ for 60-120 minutes until it solidifies.

5. **Pattern Molding**: After curing, the PDMS is carefully peeled from the master and its surface replicates the relief structure on the surface of the original master. Then, the PDMS cast is perforated at the extremes of the printed channel to set the inlet and outlet, that will allow the entrance of fluid and air.

6. **Sealing**: The PDMS cast is set with a clean glass substrate on the Plasma Cleaner for 10 seconds. This way a molecular sweep occurs in both surfaces which are irreversible sealed at contact by means of a molecular bonding.

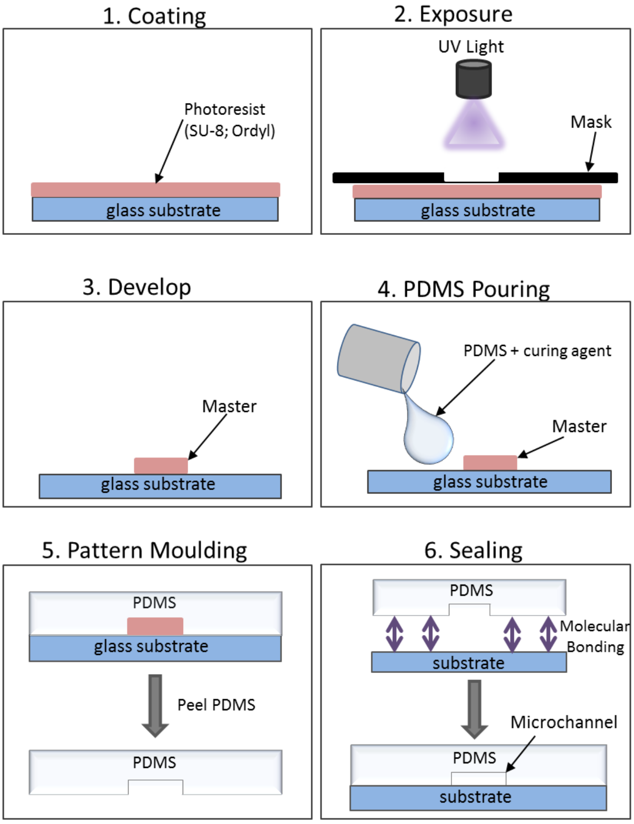

Figure 4.3: *Schematics of the steps of the microfabrication process. The general features of the process are described in the previous list and identified with its respective number on the figure. Details on the fabrication process of microchannel are presented in Appendix A.*

4.2 Experimental Setup and Method

The setup we use to perform the experiments was based on previous work developed at the microfluidics laboratory [Pradas Gené, 2009; Queralt-Martín et al., 2011; Queralt Martín, 2009]. Some modifications were made to the base setup and new equipment was acquired. The new equipments acquired for the laboratory at the Departament d'Estructura i Constituents de la Matèria were:

1. Microscope Optika B-353LD1
2. High Speed Camera: Fastec Imaging Trouble Shooter TSHRMS
3. Syringe Pump NE-300.

Measures for this thesis development were also performed at the Complex Fluids Laboratory at the Centre de Recerca Matèmatica at Bellaterra. This laboratory is equipped with:

1. Inverted Microscope Optika XDS-3
2. High Speed Camera: Photron Fastcam Viewer 3
3. Syringe Pump
4. Malvern Kinexus Rotational Rheometer

4.2.1 Description of the Experimental Setup

Our experimental setup consists of a fluid column in a width container of 5 cm diameter submitted to atmospheric pressure. The fluid container is set over a platform with controlled vertical movement which allow us to vary the column height from $H = 0$ to $50\,cm$.

The container is connected to the microchannel through a small biocompatible tube, with uniform internal circular cross-section of radius $r = 0.127\,mm$ and length $l_t = 43.0 \pm 0.1\,cm$.

The microdevice is set on the microscope plate to obtain a zoomed image of the fluid-air interface. The motion of the interface inside the microchannel is recorded by the high speed camera. A scheme and a photograph of the experimental setup are presented in Figures 4.4 and 4.5, respectively.

The fluid enters the microchannel pushed by a pressure difference, ΔP, exerted by the fluid column set at heights from $H = 0.420$ to $0.050\,m$. Since the fluid container and the outlet of the microchannel are exposed to air, the atmospheric pressure, P_{atm}, does not play a role, therefore, the pressure difference is given almost entirely by the hydrostatic pressure, $P_{hyd} = \rho g H$. Here ρ is the density of the fluid, g the acceleration of gravity and H the distance from the microchannel entrance to the top of the fluid column in the container.

We use a wide fluid container to have a negligible variation of the height of the fluid column, ΔH, while the microchannel is been filled, see Figure 4.6. Thus, the

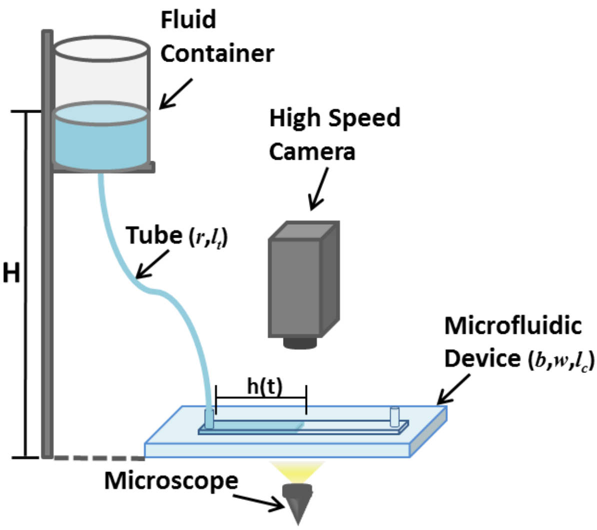

Figure 4.4: *Scheme of the experimental setup. H, is the height of the fluid column and $h(t)$ the position of the fluid front inside the microchannel. The diameter of the fluid container is $d = 5\,cm$. The height of the fluid column can vary from $H = 0\,cm$ to $H = 50\,cm$. The tube parameters are: radius, $r = 0.127\,mm$ and length, $l_t = 43\,cm$. The microchannel parameters are: length $l_c = 4\,cm$, width $w = 1\,mm$ and heights from $b = 50\,\mu m$ to $b = 350\,\mu m$.*

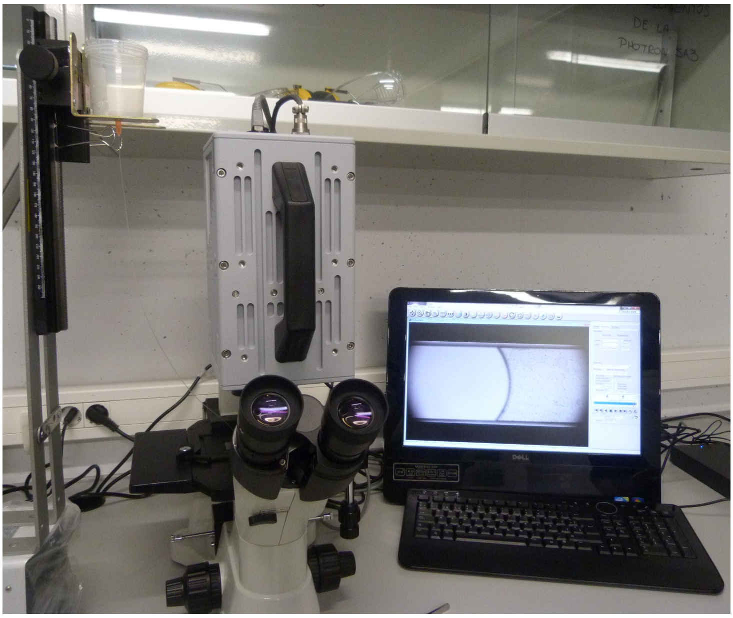

Figure 4.5: *Photograph of the set up. In this image we appreciate the captured image of the zoomed fluid interface inside the microchannel.*

hydrostatic pressure exerted does not depends on time and may be consider constant. To estimate the variation of height, ΔH, we consider the volume of liquid that fills the channel, V_{ch}, and the difference in volume inside the fluid container, V_{co}, as:

$$\begin{aligned} V_{co} &= V_{ch} \\ \pi r^2 \Delta H &= bwl_c \\ \Delta H &= \frac{bwl_c}{\pi r^2} \end{aligned}$$

For a container of $5\,cm$ of diameter and a microchannel of $b = 350\,\mu m$, $w = 1\,mm$ and $l_c = 4\,cm$ the difference in height is $\Delta H \approx 10^{-3}\,mm$. This variation on the height of the fluid column gives an hydrostatic pressure, $P_{hyd} \approx 10^{-2} << 1\,(Pa)$. Hence, the pressure variation as the channel is being filled is considered negligible.

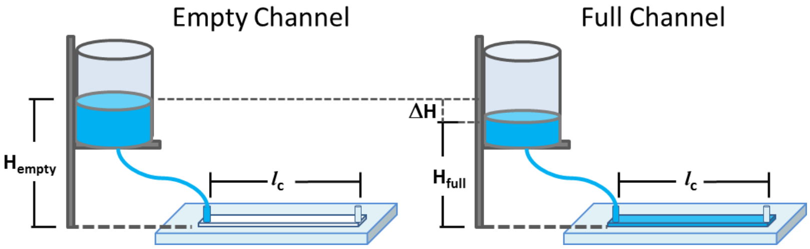

Figure 4.6: *Representation of the variation of height ΔH, when the channel is empty and when the channel is filled with liquid. Considering the parameter of our experimental setup, $\Delta H \approx 10^{-3}\,mm$ which is a pressure difference of $\Delta P_{hyd} \approx 10^{-2}\,Pa$.*

Modification to the setup for blood measures

An slight difference in the setup is made when the measures are performed with blood. Since blood is a suspension of cells, it presents experimental complications due to the sedimentation of these cells. In order to avoid the effects of sedimentation at the bottom of the fluid container, this one is filled with a glycerol dilution instead of blood. The density ρ of the glycerol dilution is approximate to the blood density to maintain the values of the hydrostatic pressure unaltered. This modification to the setup is shown in Figure 4.7 and the percentages of the glycerol dilution are shown in Table 4.1.

4.2.2 Image Acquisition

The camera captures the fluid-air interface, view from the top of the channel, in an image of dimensions $640 \times 288\ (pixel)^2$. The range of vision depends on the magnitude of the microscope objective. The objectives used to capture the images of the fluid front are $4\times$ or $10\times$ of magnitude. For a $4\times$ magnitude objective the vision range of the channel length is approximately $5\,mm$, while for an objective of $10\times$ magnitude is around $2.5\,mm$. In Figure 4.8 we can see the microchannel under the microscope,

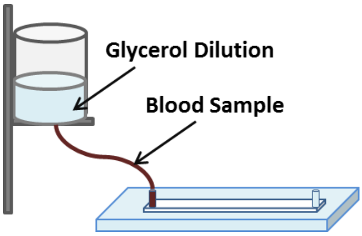

Figure 4.7: *Representation of the modified setup for blood.*

RBCs concentration	Density, ρ $\left(\frac{kg}{m^3}\right)$	Glycerol concentration
45%	1050	19%
20%	1035	14%
Blood Plasma	1025	10%

Table 4.1: *The table shows the concentration of glycerol for each value of the concentration of blood to obtain an equivalent density. All the values are taken at a temperature of* $20°C$.

half full of blood, while Figure 4.9 shows a photogram of the interface seen by the microscope and capturated by the high speed camera.

To study the position of the fluids interfaces we record the front moving inside the channel with the high speed camera, which captures images at rates between 50 and 1000 frames per second. The camera records the fluid front moving along a segment of the channel of $2.5\,mm$ or $5\,mm$ long. Each recording may be decomposed in photograms of the front at each time at a different position in the trail. The frame rate of capture is previously determined considering the expected velocity of the interface. In case of overestimating this frame rate, the camera software gives the option to skip extra frames. This is a useful tool since the frame rate needs to be adapted later to the precision error of the position (section 4.3).

This procedure is repeated along the whole channel at two different heights of the fluid column, a big height to achieve high injection pressures and a small height for small injection pressures. From this procedure we obtain the behavior of the fluid front throughout the microchannel length. The velocity of the fluid is obtained by tracking the mean fluid front position as a function of time between several contiguous images and averaging its values for each segment of the channel.

Once we have obtained the images of the position of the front along the whole length of the channel ($4\,cm$), we proceed to the calculation of the velocity of the interface at an specific position of the microchannel, usual position are $h = 10\,mm$, $h = 20\,mm$ and $h = 30mm$ from the channel inlet. We performed the measurements at different injected pressures, ranging from $P_{hyd} = \rho g H = 4320$ to $490\,[Pa]$ every $200\,[Pa]$ steps.

This measures are performed fixing an starting height for the fluid column and recording the motion of the front. The measurements are repeated 10 times or more until the standard deviation of the measures is lower than a 10%. Then we proceed to vary the height of the column lowering the container $2\,cm$. We vary this height to observe a significative variation of the velocity of the front. In the case of fluids with high viscosity (i.e. blood, glycerol dilutions) to obtain a significative variation of the behavior of the front we measure every 5 or $4\,cm$ of height which correspond to $P_{hyd} \approx 500$ to $400\,[Pa]$.

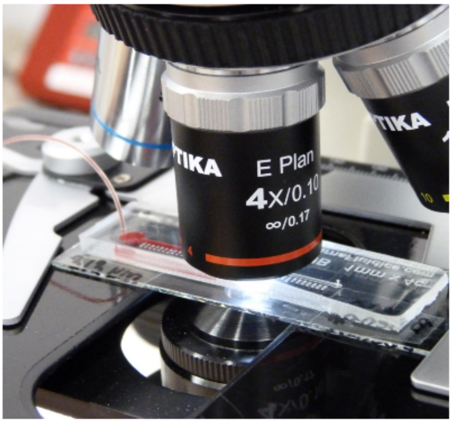

Figure 4.8: *Photograph of the microdevice half full of blood under the microscope.*

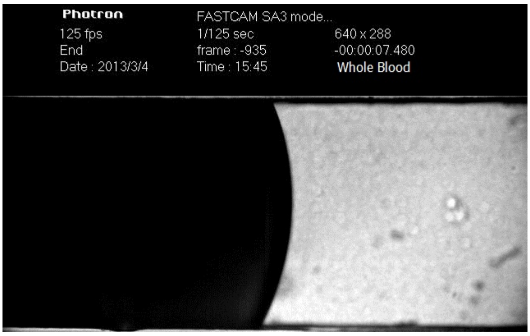

Figure 4.9: *Real time image of the blood-air interface through the microscope, image dimensions are* $640\times288\,pixel^2$. *This image was obtained using a* $10\times$ *objective capturing* $\approx 2.5\,mm$ *of channel length.*

4.3 Images Analysis

The images captured with the high speed camera are transformed into a matrices and analized using a computational code written in Wolfram Mathematica©based on a previous Matlab code [Queralt Martín, 2009]. The code can be separated in 3 different parts:

1. Image Processing: Transformation of images into matrices.
2. Calculation of the position and the velocity of the mean front.
3. Statistical analysis: elimination of spurious data.

Each part will be explained in detail in the following subsections. Details of the code functions are presented in Appendix F.

4.3.1 Image processing

Each photogram may be converted into a matrix $h_{N\times M}$, where each element $h_{i,j}$ of the matrix represents a pixel and its value represents a color. Since our camera gives images in grayscale, colors are range between 0 and 1 where 1 is white and 0 is black. In this case, pixels are easy converted in 1's and 0's using a color brightness criteria.

First, the images are cropped to eliminate unneeded information from the image, leaving a $636 \times 200\,(pixel)^2$ image for an objective of $10\times$ magnitude and $636 \times 100\,(pixels)^2$ for an objective of $4\times$ magnitude. Then, the background of the empty channel is subtracted from the image leaving only the fluid front as a feature. Some images need to be adjusted in contrast and brightness, especially those with narrow fronts. Later, the image is transformed into a binary image (black and white) by replacing all values above a globally determined threshold with 1's and others with 0's. Finally, the image is converted into a matrix of 1's and 0's. Figure 4.10a shows the steps to obtain the binary image from a captured front of a transparent fluid, while Figure 4.10b shows the same process for blood.

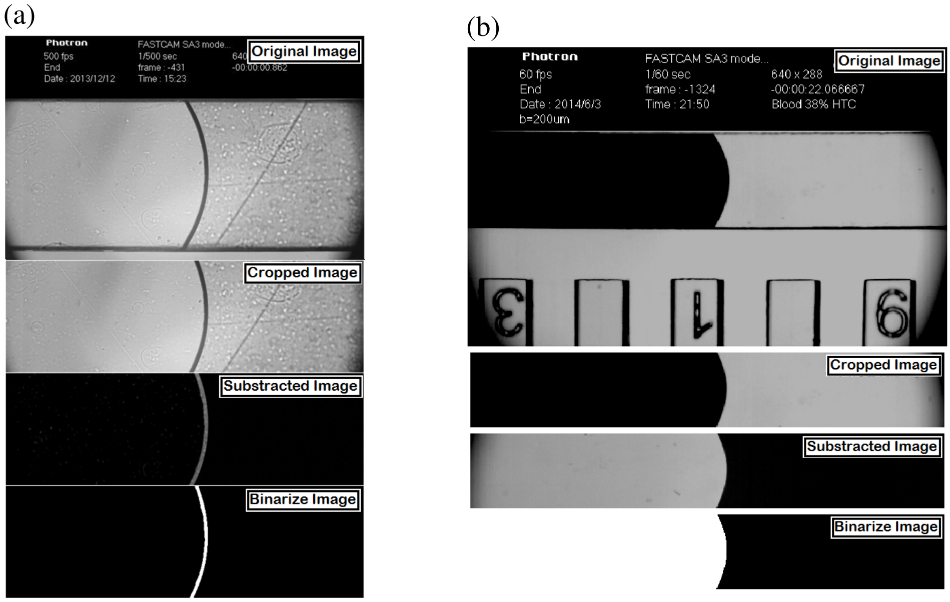

Figure 4.10: *Figure (a) shows the steps of the image processing for a transparent fluid using an objective of* $10\times$ *magnitude. Figure (b) shows the image processing for blood using an objective* $4\times$ *magnitude. When the image is transformed into a matrix white pixels become 1's and black pixels become 0's.*

4.3.2 Position and Velocity of the mean interface

The second part of the images analysis is to determine the position of the mean front and the calculation of the mean velocity of it along the captured length of the channel. In the case of transparent fluids, the original front is a black shadow which turns white at the binary transformation and it is translated into 1's in the matrix (Figure 4.10a). We calculate the average position of the 1's in every row on the matrix, $h_j(t)$, and then those positions are averaged to the total number rows, N, to obtain the mean position of the front, $h(t)$, as:

Microscope objective	Captured length of channel	μm per pixel	Sensitivity error $\delta h\,(\mu m)$
$4\times$	$5\,mm$	7.8	± 0.8
$10\times$	$2.5\,mm$	3.5	± 0.2

Table 4.2: *The table shows the equivalence of* $1\,pixel$ *in* μm *and the captured length of the channel, depending on the microscope objective used to performed the measurements.*

$$h(t) = \frac{1}{N}\sum_{j}^{N} h_j(t) \tag{4.1}$$

A modification to this process is performed when we are working with blood. Since the binary image is composed of full rows of 1's (Figure 4.10b), instead of averaging every 1's in the rows, we average the positions of the last 1 in each.

The raw data of the position is calculated in pixel. Since the microscope is calibrated to know the size in microns of a pixel we multiply by the number of microns and we obtain the position in μm of the front. This conversion from pixels to μm depends of the calibration of the camera and the microscope objectives, see Table 4.2. Our measure of position has an associated sensitivity error given by the resolution of the system which is $\delta h_j = 1\,pixel$. This error is translated into μm and averaged to the total number of rows use to calculate the mean position of the front:

$$\delta h = \frac{\delta h_i}{\sqrt{N}} \tag{4.2}$$

To calculate the instantaneous velocity of the moving front we use a simple relation of linear velocity between the position of the mean front and the time between 2 consecutive images, as follows:

$$\dot{h}_k = \frac{h_{k+1} - h_k}{t_{k+1} - t_k} = \frac{\Delta h}{\Delta t} \tag{4.3}$$

Here k corresponds to the image that is been analized at the moment, Figure 4.11 shows schematically how the images and time steps are considered. Since time is an intrinsic parameter of the measure given by the camera it does not provides an associated sensitivity error.

Therefore the velocity error is given only by the sensitivity error of the position which determine the adequate time steps for the measure.

The relation between the frame rate and the time steps is simply given by:

$$\Delta t = \frac{1}{frames\,per\,second} \tag{4.4}$$

If the images are captured at 1000 frame per second the time between 2 contiguous images is $\Delta t = 0.001\,s$ and so on for other frame rates.

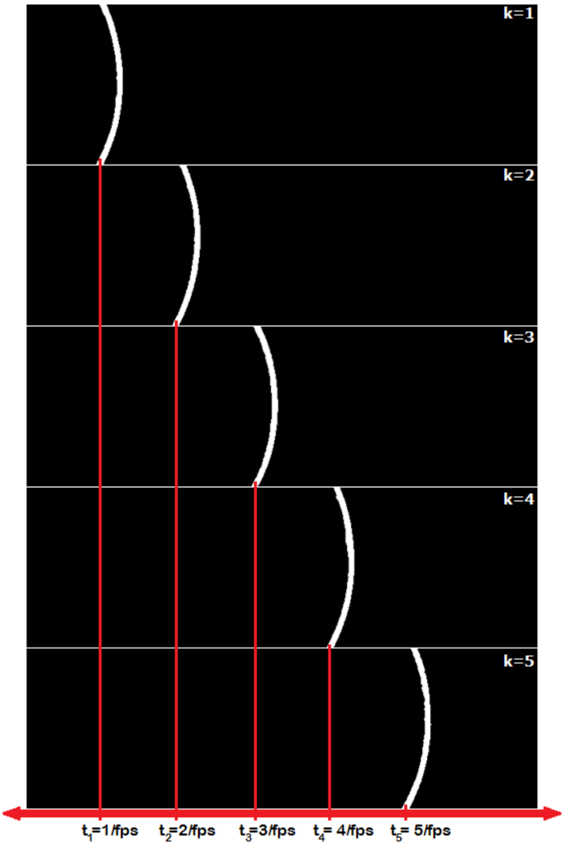

Figure 4.11: *Schematic representation of the calculation of the velocity and position of the fluid interface. Using Eq. (4.3) we obtain the instantaneous velocity between two images, k. Since this is an schematic representation, the intervals between 2 consecutive images are exaggerated in relation to the ones that are actually obtained though the measures.*

The mean velocity of the interface is simply averaged from the velocity profile of $\dot{h}_k$ given for the collection of analized images, by means of:

$$\dot{h} = \frac{1}{n-1} \sum_{k}^{n} \dot{h}_k \tag{4.5}$$

where n is the total number of images analized.

An important part to obtain an accurate analysis of the images it to take into account that the frame rate chosen is delivering a proper resolution of the position of the front, instead of spurious data or overlapped images. Figure 4.12 shows how different chosen time steps change the dispersion of the measures. The mean velocity value does not suffers a significant change even when the frame rate is reduced, however the dispersion or presicion error decreases significantly. Once the time steps for the measures are accurately defined, we proceed to extract the position and velocity data from the images correspondent to every measure performed.

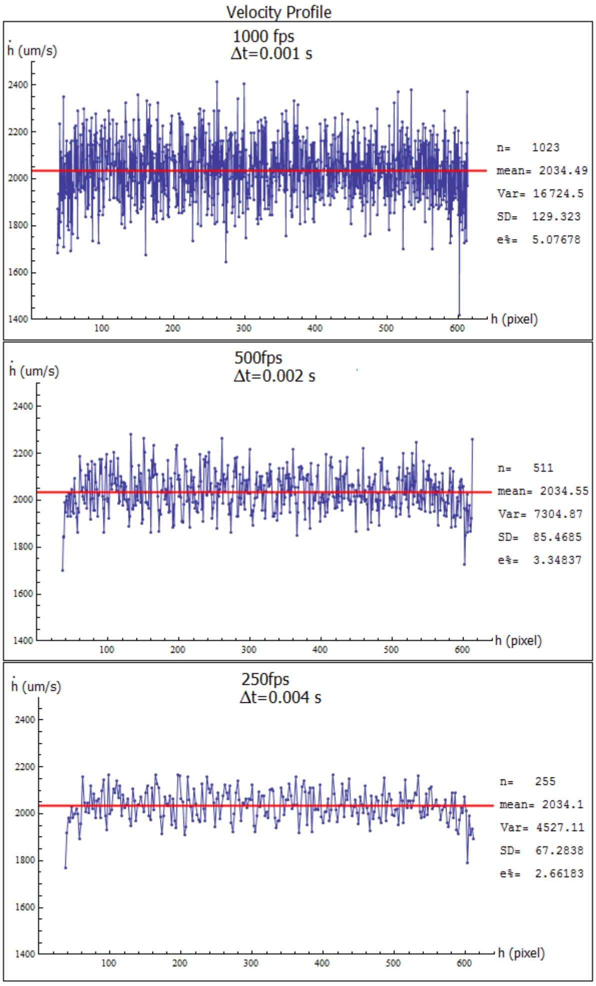

Figure 4.12: *Velocity profile for different time steps.The top image shows a time step of* $\Delta t = 0.001$ *s and a dispersion of 5.08%. The center image shows the same measure but analized with a time step of* $\Delta t = 0.002$ *s and the result dispersion is reduced to 3.34%. The bottom image shows a time step of* $\Delta t = 0.004$ *s and a dispersion of 2.66%.*

4.3.3 Statistical analysis of the data

In general, we perform from 10 to 20 experiments until the standard deviation of the measures was lower than a 10%. Once the data of the position and the velocity from all measures have been extracted, the results of every experiment are averaged (at each time step), to achieve a better statistics of the results. The final result for the velocity of the mean front is an spurious velocity profile with high dispersion which is not important to describe the overall behavior of the front. To properly eliminate unnecessary data we adjust a normal distribution to the probability density of the velocity:

$$f(x, \mu, \sigma^2) = \frac{1}{\sigma\sqrt{2\pi}} e^{\frac{-(x-\mu)^2}{2\sigma^2}} \tag{4.6}$$

where the parameter μ represent the mean velocity, σ^2 is the variance of the collection of data and σ is the standard deviation, as shown in Figure 4.13. The data situated away from 2σ is neglected. With this process we are able to decrease the dispersion error of the velocity.

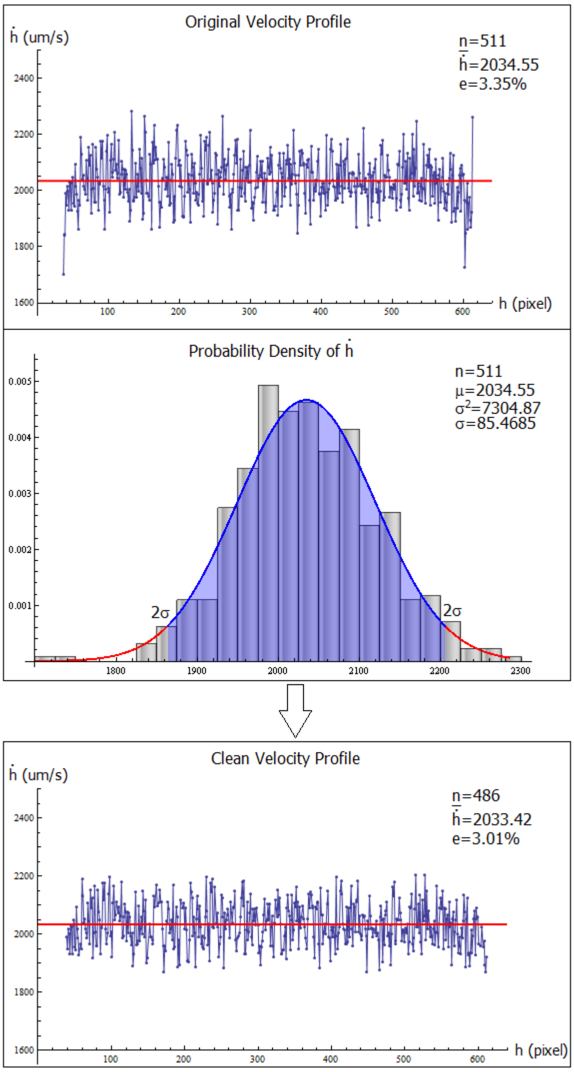

Figure 4.13: *Statistical treatment of the velocity measures. The top image shows a set of the average velocity profile for all the experiment performed. The center image shows an histogram of the data with its associated probability density of the normal distribution from Eq. (4.6). The lowest image show the final velocity profile, where the values outside 2σ from the normal distribution are eliminated.*

PART III

Newtonian Fluids

CHAPTER 5

One fluid system

The first step to check that our device and method accomplish our objectives, is to test these with simple fluids, i.e. Newtonian fluids. Each channel fabricated must be calibrated and test in order to go further into the study of blood. This part of the thesis will be dedicated to presents our results for Newtonian fluids. This chapter will be dedicated to describe the characterization and calibration of different channels and will present our viscosity results for water. Section 5.1, presents the results for water to characterize the device at various gaps $b\,\mu m$ of the microchannels. The viscosity results for water and the analytic steps to obtain it are shown in sections 5.2 and 5.3 respectively. Last, section 5.4 includes a summary and conclusions of the chapter.

5.1 Characterization of the Device

Water is a Newtonian fluid widely studied due to its abundance, easy manipulation and simple properties. At room temperature, $20-22°C$, its density is a thousand times the air density, $\rho = 1000\,kg/m^3$, and its viscosity is know to be $\eta = 1\,cP \equiv 10^{-3}\,Pas$. These features of water make it the primary calibration fluid for every viscometer.

At the clean room, we manufactured several rectangular microchannels with different geometrical parameters, where width ($w = 1\,mm$) was a constant parameter for each mold. Two different channel lengths were fabricated $l_c = 4\,cm$ and $l_c = 2\,cm$. For heights we tried many different options, from $b = 50\,\mu m$ to $350\,\mu m$ every $50\,\mu m$. Sometimes the mold does not accomplish the expected height and we have to make sure that the microchannels are accurately defined by their heights. The microchannels molds are measured using a micrometer caliper, with a sensitivity of $10\,\mu m$, to estimate their height. However, this method entail a high associated error, therefore, an alternative experimental measure must be performed.

To provide a backup value of the effective height of each microchannel, we used a syringe pump to fill the channel with water at a fixed flow rate of $Q = 10\,\mu l/min$. The time the fluid takes to travel the whole channel was measured several times to obtain an average velocity. Since the velocity of the fluid is related to the flow rate through the area of the channel as $Q = vA$, we calculate the height of the channel using the following relation:

$$b = \frac{Q}{w\,v} \tag{5.1}$$

Expected Height μm	Effective Height $b \pm \delta b \, \mu m$
50	51 ± 5
100	94 ± 6
150	148 ± 2
200	204 ± 9
250	250 ± 3
300	297 ± 7
350	352 ± 6

Table 5.1: *Effective values of the height of the channels obtained through Eq. (5.1). Each height measure was performed between 10-15 times and the error, δb, was calculated using the error propagation theory for the standard deviation of the time measures. Channel with an error $\delta b > 10 \mu m$ were not considered in these measures. Details on the channel dimension are address in Appendix E.1.*

The heights values obtained using Eq. (5.1) are shown in Table 5.1 along with their expected values and the associated error. The error in height, δb, was calculated using the error propagation theory for the standard deviation of the time measures.

It is important to make sure that the height of the micro-channel is homogeneous throughout it. To check its homogeneity, we measure the front velocities every $5 \, mm$ long and we compared it in every segment. If the velocity is approximately the same at each segment, then the channel is considered homogeneous. Microchannels with a difference in height over $10 \, \mu m$ along, were considered heterogeneous and were not used to perform the measurements.

5.1.1 Position against Time

The aim of our design is simplicity and constant velocity is the simplest way to characterize a fluid moving inside the channel. Based on a previous work developed at the microfluidics laboratory [Queralt Martín, 2009], we tested the advancing water-air interface along the whole channel for different microchannel gaps. The measurements were taken every $5 \, mm$ segments of the channel's length. We set the column height at $H = 200 \, mm$ which gives an approximate hydrostatic pressure of $P_{hyd} \approx 2000 \, Pa$. Using the Image Analysis Code (section 4.3, appendix F) we obtained the position of the water front for different channels as the fluid fills them.

Our first objective is to describe the position and the velocity of the fluid front, inside the microchannel, as a function of time. To achieve this, the data of the position as a function of time is fitted using the graphic fitting method of least square regression to a power law. Hence, we fit our data according to:

$$h(t) - h_0 = v(t - t_0)^{\nu} \tag{5.2}$$

Eq. (5.2) returns the fitted values of the parameters ν and v. The parameters t_0 and h_0 correspond to the minima time steps for each channel and the position at this initial time step $h_0 = h(t_0)$, respectively.

In Eq. (5.2) the parameter ν defines the behavior of the position of the front. If this value is $\nu \approx 1$ we have a situation where the position of the front is linear with time which implies that the velocity of the front is constant.

At the tested pressure we found that the exponent values from Eq. (5.2) vary from $\nu = 0.959$ to $\nu = 1.002$, see Figure 5.1. Since the slopes values from the tests are close to 1, we consider that the water front is moving at constant velocity. The time exponent for each microchannel height is shown in Table 5.2, as well as the fitted velocities of the fluid front inside the channels.

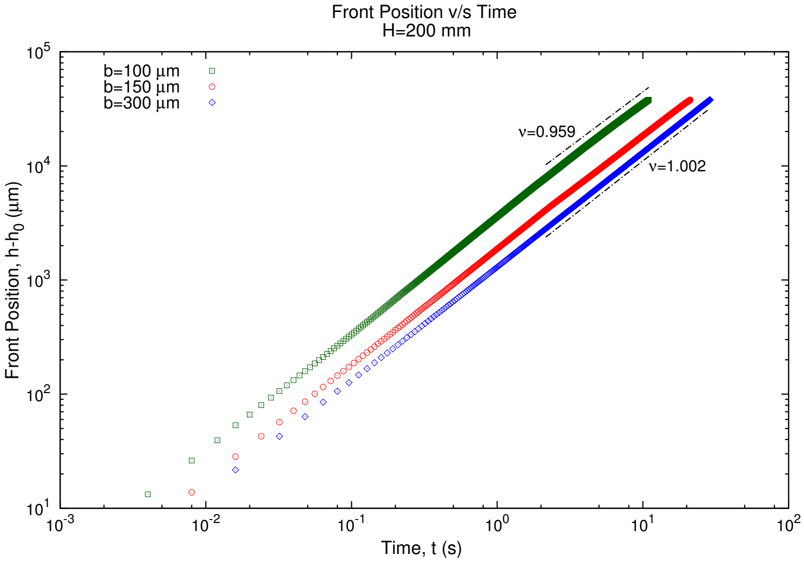

Figure 5.1: *Position as a function of time for water in microchannels of different heights: $b = 100\,\mu m$ (dark green), $b = 150\,\mu m$ (red) and $b = 300\,\mu m$ (blue). For a fixed hydrostatic pressure of $\rho g H = 1960\,Pa$. The fitted exponent for these featured heights varies from $\nu = 0.959$ to $\nu = 1.002$, therefore it can be considered $\nu = 1$ which correspond to a constant velocity.*

Even thought, we have been able to observe an approximate linear behavior of the position as a function of time for several microchannel heights, we can not infer what happens at different hydrostatic pressures. To extend the observations and develop a protocol for the conditions of the experiments, where the fluid front maintains its velocity constant through the channel, we need to perform the previous experiment at different hydrostatic pressures.

To discard the effects of hydrostatic pressure on the time exponent values, we performed the measure at a low column height and a high one for a channel of $b = 300\mu m$, since the results for this channel gap submitted to $H = 200\,mm$ shows a near 1 exponent. The selected fluid column heights were $H = 30\,mm$ and $H = 290\,mm$. The

Channel Height $b(\mu m)$	Minimum Time Step $t_0\,(s)$	Initial Position $h_0\,(\mu m) \pm 0.8$	Position Exponent ν	Mean Velocity from fit $v\,(\mu m/s)$
100	0.004	81.9	0.9587± 0.0003	3854±3
150	0.008	283.0	0.9761± 0.0002	1943±1
200	0.008	472.2	0.9899± 0.0001	1765.32±0.04
250	0.008	244.1	1.0016± 0.0002	1569.3±0.8
300	0.016	278.4	1.0019± 0.0001	1309.8±0.1

Table 5.2: *The table shows the parameters obtained from the fit using Eq. (5.2) for 5 different microchannel heights at an hydrostatic pressure of* $\rho g H = 1960\,Pa$.

position evolution in time at both heights, along with its fitted function, are shown in Figure 5.2 and the exponent values and initial conditions are shown in Table 5.3.

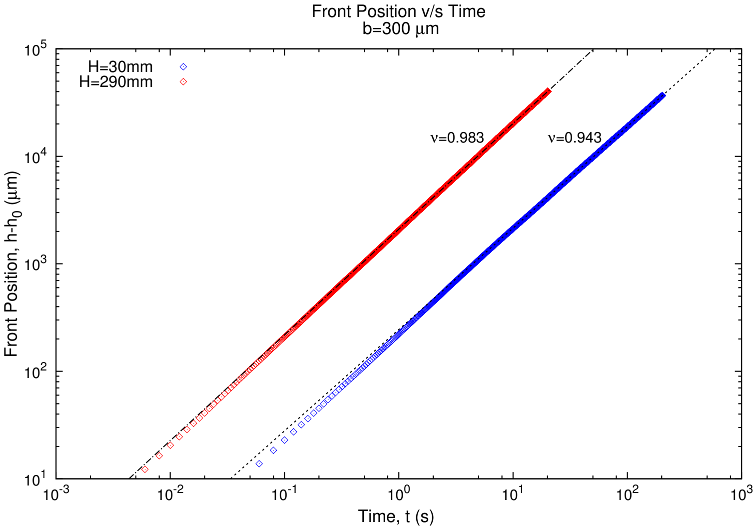

Figure 5.2: *Position of the mean front of water as a function of time moving inside a microchannel of* $b = 300\,\mu m$ *submitted to 2 different fluid column heights:* $H = 290\,mm$ *(blue) and* $H = 30\,mm$ *(dark blue). The lines are the correspondent fitted function from Eq. (5.2). The fitted exponents are* $\nu = 0.946$ *for* $H = 30\,mm$ *(dashed line) and* $\nu = 0.983$ *for* $H = 290\,mm$ *(dot dashed line). Additional parameters are shown in Table 5.3.*

Again we obtained a near 1 exponent for $H = 290\,mm$ which allow us to confirm the constant velocity behavior of the fluid front on a $b = 300\mu m$ height microchannel. However, for a $H = 30\,mm$ column height the exponent is far from the expected $\nu = 1$ that indicates constant velocity. Considering these values of the exponent, we need to clarify the conditions of constant velocity.

In order to test the accuracy of the exponents obtained for the position, we observed the velocity of the water front as a function of the position through the microchannel in order to appreciate if it remains constant.

Column Height $H\,(mm)$	Minimum Time Step $t_0\,(s)$	Initial Position $h_0\,(\mu m) \pm 0.8$	Position Exponent ν	Velocity from fit $v\,(\mu m/s)$
30	0.02	95.1	0.9458± 0.0004	241.82±0.05
290	0.002	98.9	0.9833± 0.0002	2097.6±0.1

Table 5.3: *The table shows the parameters of the fitted function of position against time from Eq. (5.2) for a microchannel of* $b = 300\,\mu m$ *at 2 different fluid column heights.*

5.1.2 Velocity against Position

We measure the mean velocity for each different microchannel along its length at a fixed injected pressure of $\rho g H = 1960\,Pa$. At each segment of $5\,mm$ we obtained a velocity profile as the one shown in Figure 5.3. The mean velocity of the fluid front is calculated using the expressions discussed in section 4.3 from the previous chapter. The represented position of the front corresponding to the segments of $5\,mm$ is the central position of the microchannel, $h = 20\,mm$.

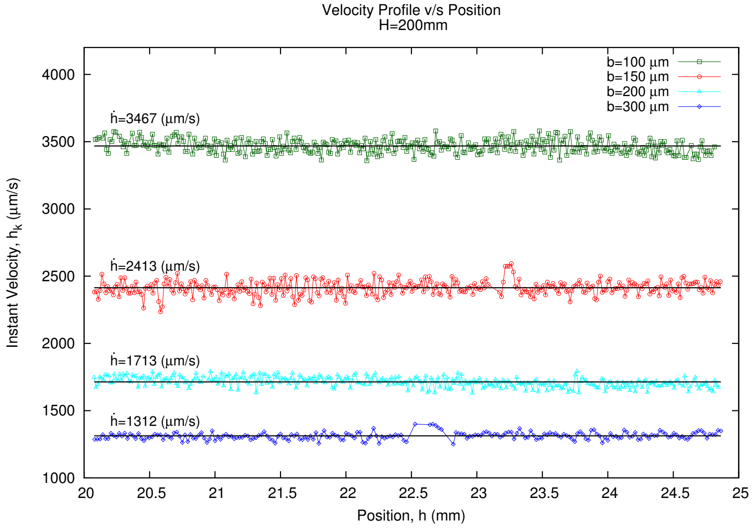

Figure 5.3: *Velocity profile as a function of the position of the water front, in channels of different heights. The exerted hydrostatic pressure is* $\rho g H = 1960\,Pa$. *The profile is shown for a segment of* $5\,mm$ *of the channel measured at* $h = 20\,mm$ *from the inlet.*

As seen in Figure 5.4, for the established exerted pressure, at channels heights larger than $b = 100\mu m$, the velocity values at each segment do not vary significantly above the experimental error. This allows us to ensure a constant velocity behavior for these conditions. To verify the front behavior, we performed the same measure for channels with distant feature heights, $b = 50$, 150 and $300\mu m$, at a higher hydrostatic pressure, $\rho g H = 2940\,Pa$ [**?**].

From Figure 5.5, we observe that if we increase the values of the injected pressure the small decay observed at $\rho g H = 1960\,Pa$ for the channel of $b = 150\mu m$, disappears. This give us a broader range of pressures to test. For each microchannel, it is then fundamental not to lower the pressure value down a threshold that varies for each channel height.

In order to evaluate the threshold value for the different pressures and heights of the fluid column, we calculated the mean velocity values at several segments of $2\,mm$ along the channel of length $l_c = 4\,cm$ and height $b = 300\mu m$, these values are shown in Figure 5.6. If we compared the velocities at the beginning and the end of the channel in both cases, we find that for an hydrostatic pressure of $\rho g H = 294\,Pa$ ($H = 30\,mm$) the decrease of velocity is 22% (close to the value for a microchannel of $b = 100\mu m$ at $\rho g H = 1960\,Pa$), whereas for $\rho g H = 2842\,Pa$ ($H = 290\,mm$) the decrease is 2.84%. We discard that these velocity reductions are due to heterogeneities along the microchannels, since these conditions have been already tested and heterogeneous microchannels were neglected.

Taking these features into account we may define a minimum height of the fluid column and pressures at which the velocity of the channel does not decrease more than a 10% from the beginning to the end of the microchannel, which corresponds to an exponent $\nu > 0.96$. In the case of channels of $b = 300\,\mu m$ the minimum column height which maintains the constant velocity behavior is $H = 50\,mm$ which correspond to $\rho g H = 490\,Pa$, for water.

The previous analysis was also performed for a channel of $b = 150\,\mu m$, and we established a minimum hydrostatic pressure to ensure the constant velocity regime, at least until the first half of the channel is filled. Accordingly to the "10% criteria", the minimum column height which holds the constant velocity of the fluid front is $H = 100\,mm$ that corresponds to an hydrostatic pressure for water of $\rho g H = 980\,Pa$. The upper limit of the hydrostatic pressures is given by the limitations of the experimental set up, which is $H \approx 420\,mm$ equivalent for water to $\rho g H = 4116\,Pa$ (see section 4.2).

To complete the characterization of the behavior of the velocities of the water front, which depend on the geometry of our microchannels, one last feature needs to be clarified. To acquire a broader understanding on how the hydrostatic pressure plays a role in the behavior of the water interface inside the microchannel, we measured the velocity of the water front for 3 different heights of the fluid column $H = 100\,mm$, $H = 220\,mm$ and $H = 300\,mm$. We performed the measure at the central position of the channel, $h = 20\,mm$ from the inlet. Supported by Figure 5.4, at this position the velocity of the front is constant for all channel heights.

In Figure 5.7, we observe the obtained velocities for 5 different microchannel heights, and for 3 different exerted hydrostatic pressures. From this figure, we can see that the relation between the velocity of the water front is not linear and it is more pronounced at high hydrostatic pressure values. The observed decrease of the velocity

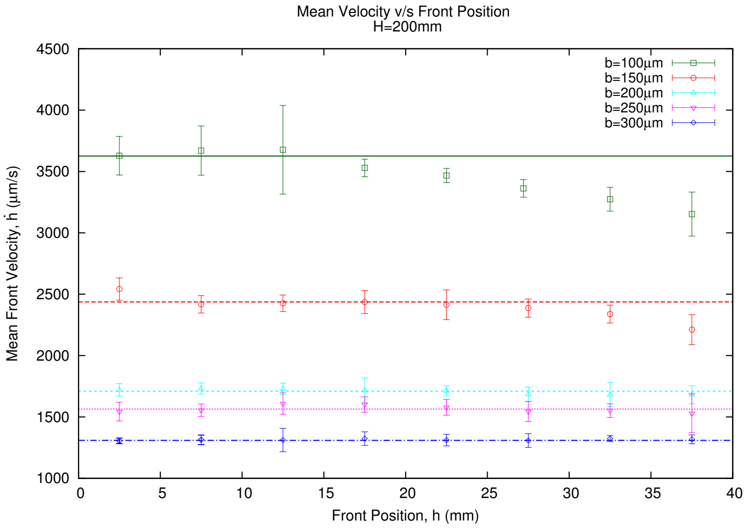

Figure 5.4: *Mean velocity as a function of the position of the water front in channels of different heights. The mean velocity is calculated for every* $5\,mm$ *segment, for a fixed exerted hydrostatic pressure of* $\rho g H = 1960\,Pa$*. The different lines represent the mean velocity along the whole channel.*

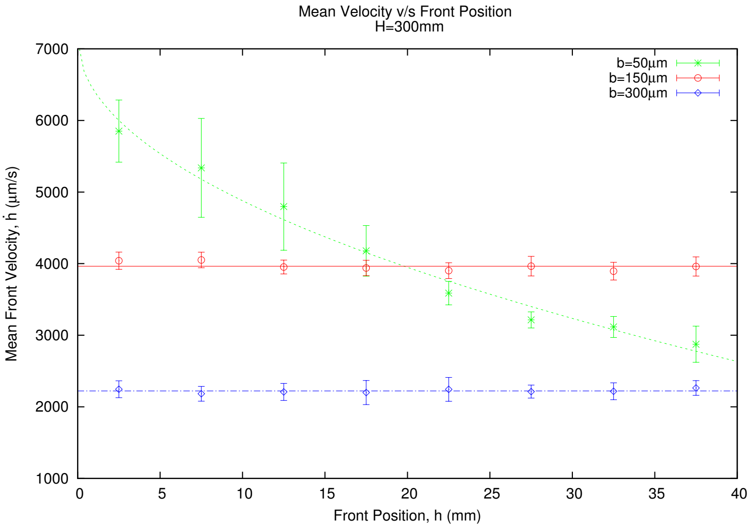

Figure 5.5: *Mean velocity as a function of the position for water in channels of different heights. The mean velocity is calculated every* $5\,mm$ *segment, for a fixed exerted hydrostatic pressure of* $\rho g H = 2940\,Pa$*. The different lines represent the estimated velocity along the whole channel. We can see from the figure how for a channel of* $b = 50\mu m$ *the constant velocity regime no longer remains.*

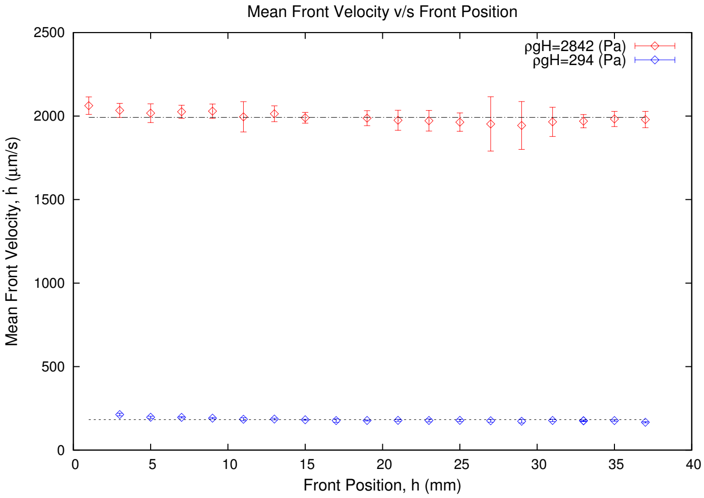

Figure 5.6: *Mean velocities of the water front at different positions inside a microchannel of* $l_c = 40\,mm$ *long. The mean velocities are taken for segment of* $2\,mm$ *for two different height of the fluid column* $H = 290\,mm$ *(red) and* $H = 30\,mm$ *(blue). This figure is the velocity representation of Fig. 5.2 as a function of the position of the mean front. From the data corresponding to this measures we can estimate the decrease in velocity at each column height. For* $H = 30\,mm$ *the velocity of the front is reduced on a 22% from the beginning to the end of the canal. In the case of* $H = 290\,mm$ *we estimate the velocity reduction is only a 2.83%.*

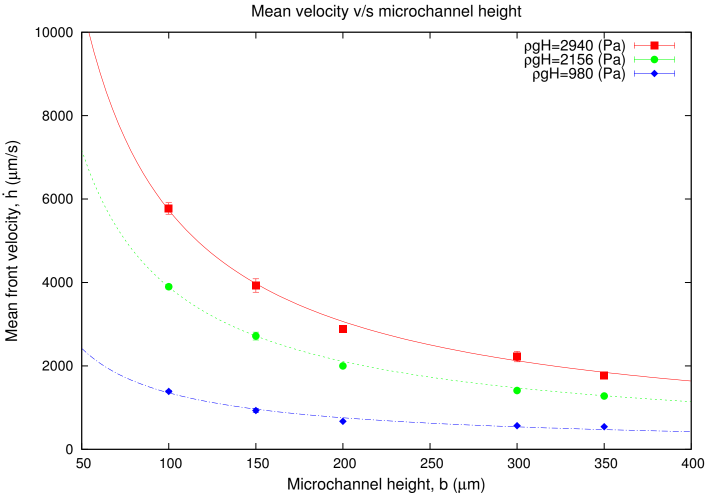

Figure 5.7: *Mean velocity of water front as a function of the microchannel height,* $b\,\mu m$*, for 5 different channels and 3 different fluid column heights,* $H = 300\,mm$*,* $H = 220\,mm$ *and* $H = 100\,mm$*, which correspond to the hydrostatics pressures:* $\rho g H = 2940$*,* 2156 *and* $980\,Pa$ *respectively. These velocities were measured at the center of the channel at* $h = 20\,mm$ *from the inlet.*

of the fluid front as the channel height increases arises several issues which will be address and explain in section 5.3.

5.1.3 Interface Curvature

Due to the hydrophobic properties of the material used to manufacture the microchannels, the fluid interface has associated a capillary pressure, ΔP_c, that depends on the surface tension, τ, of the fluid and the curvature, R of the fluid interface.

The capillary pressure is a pressure difference present across the interface of a nonzero surface tension calculated by means of the Young-Laplace equation:

$$\Delta P_c = \frac{2\tau}{R} \tag{5.3}$$

In the case of a rectangular geometry the curvature of the general surface is represented by two principal curvature radii and Eq. (5.3) takes the form:

$$\Delta P_c = \tau \left(\frac{1}{r_1} + \frac{1}{r_2} \right) \tag{5.4}$$

Our experimental setup does not allow us to obtain the secondary curvature of the interface but considering the geometrical parameters of the microchannel, height b and width w, and performing some trigonometric and geometrical ajustements, which are shown in Appendix D, we obtained an alternative expression for ΔP_c:

$$\Delta P_c = 2\tau cos\theta \left(\frac{1}{b} + \frac{1}{w} \right) \tag{5.5}$$

The values of the parameters τ, b and w from Eq. 5.5 are known. Analyzing the experimental images of the fronts we obtain an average contact angle θ, as shown in Figure 5.8 for a channel of $b = 300\mu m$. In this particular case, the contact angle does not suffers significative change when the pressure is increased and the value of the capillary pressure oscillates around $\Delta P_c = 200\,Pa$. Nevertheless, for smaller channels, $b < 150\mu m$, the variations of the contact angle become important and so does the value of the capillary pressure which varies from $\Delta P_c = 400$ to $800\,Pa$, for details refer to Appendix D.

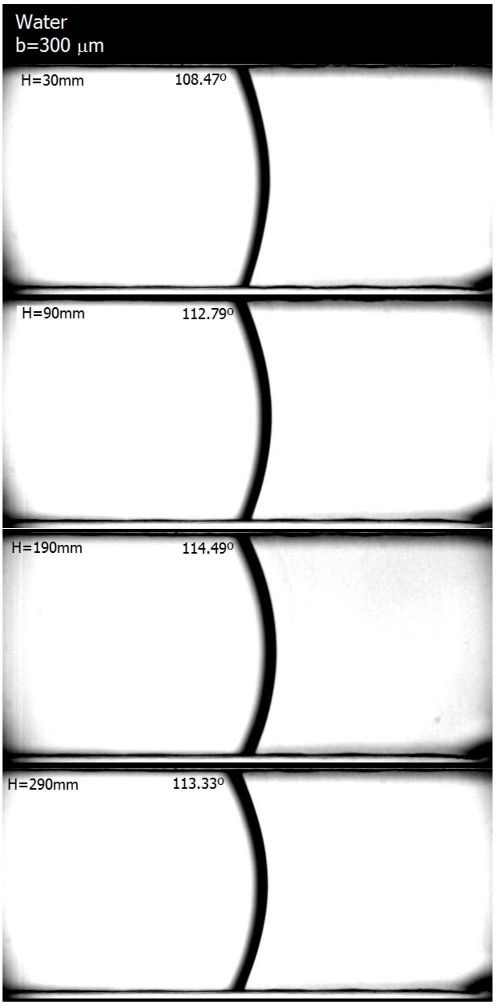

Figure 5.8: *Curvature of the water front for a channel of* $b = 300\,\mu m$ *at different hydrostatic pressures with its correspondent values of the contact angle with the side walls.*

5.2 Water Results

Once the device is well characterized for each channel height, $b\,\mu m$, we are able to start the velocity measures of the fluid front at different hydrostatic pressures. Since we have the advantage of having a constant velocity along the channel, meaning that $\dot{h}$ does not depend on the position h, we have chosen to measure the velocity in the center of the channel at $h = 20\,mm$ from the inlet. We chose this position to avoid instabilities caused by the entrance of the fluid inside the channel. We fix the microscope at the center on the channel and capture the images of the water front. We change the height of the fluid column and by analyzing the image of the front we calculate its velocity, at each different column heights, i.e., hydrostatic pressures.

5.2.1 Hydrostatic Pressure and Velocity

The velocity of the fluid front is measured at different heights of the fluid column. We star the measurements with a high hydrostatic pressure corresponding to a fluid column of height $H = 0.400\,m$ and lowered $0.020\,m$ until reaching the threshold height for each channel, between $H = 0.050$ and $0.10\,m$, depending on the channel height. As mentioned in the previous section at these low pressures the water-air interface position must still preserve the linear regime. At each height we obtain a velocity profile of the moving fluid front with a dispersion lower than 1.82%. These measures are performed for different channel heights as shown in Figure 5.9.

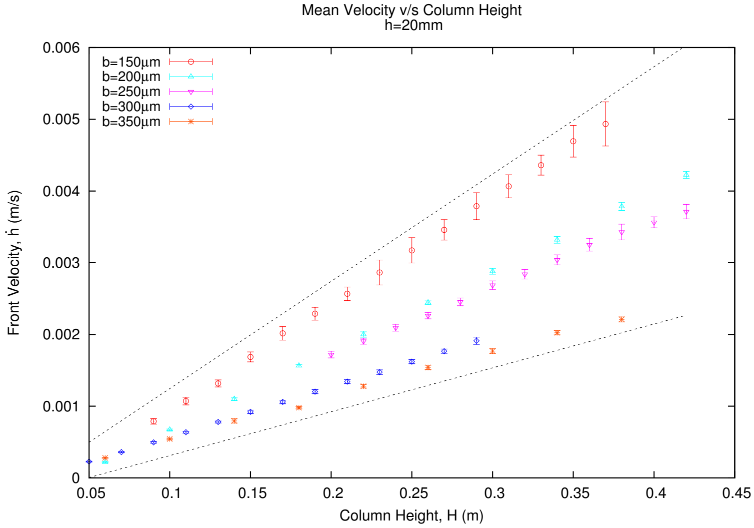

Figure 5.9: *Velocity of the water front as a function of the height of the fluid column for different microchannel gaps, from $b = 150$ to $350\,\mu m$. The dotted lines represent a linear fit with different values of the slope, a, of the function y=ax+b.*

We relate each height of the fluid column to an hydrostatic pressure by $P_{hyd} = \rho g H$ and we associate it to its corresponding velocity response, $\dot{h}$. Since our test fluid is water and therefore Newtonian, we assume the relation between the exerted pressure and the velocity to be linear and we fit a simple expression as:

$$\rho g H = A\dot{h} + P_L \tag{5.6}$$

The results obtained from equation (5.6), are shown in Figure 5.10 for different microchannel gaps with its respective linear fit and the associated dispersion error for each velocity.

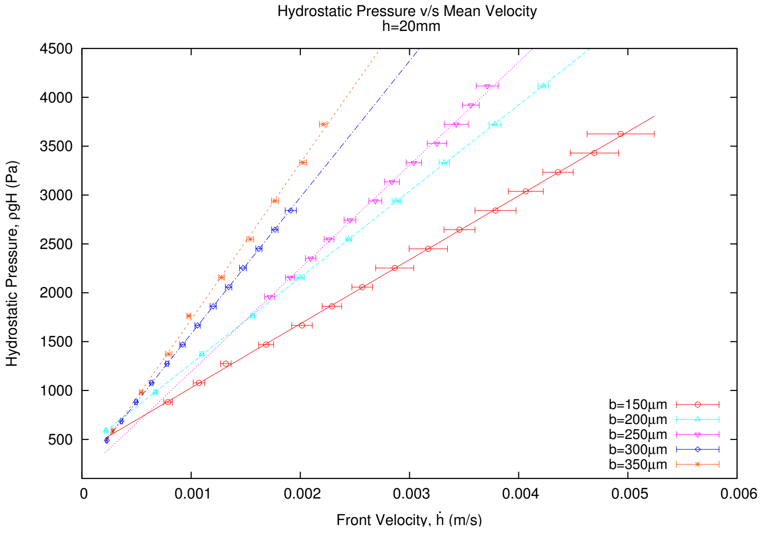

Figure 5.10: *Hydrostatic pressure as a function of the velocity of the water front for different gaps of the microchannels. The lines show the linear fit obtained for each microchannel gap using Eq. (5.6).*

From Eq. (5.6) the independent term is the pressure value at $\dot{h} = 0$, which is interpreted as the minimum value of the pressure for the fluid to start to move through the channel, i.e. the Laplace Pressure due to the curvature of the fluid front. We assume this, since experimentally we observed that while a pressure is increased from $\rho g H = 0\,Pa$, the fluid does not move immediately and it must acquire a minimum curvature before it star to advance through the channel. The values of the minimum pressure obtained from the linear fit are compared in Table 5.4 with the values of the capillary pressure obtained through the analysis of the curvature of the fluid front with Eq. (5.5) from subsection 5.1.3.

From Table 5.4 we highlight that for the microchannels of $b = 150$ and $300\,\mu m$ the values of the capillary pressure from the front curvature and the ones obtained from the fit for $\dot{h} = 0$ are similar.

As explained in section 2.2 from the introduction Chapter 2, we expect a behavior of the front compatible with a Darcy law with a permeability of a microrectangular cell, $\kappa = \frac{b^2}{12}$, as:

Channel Height μm	P_L (from fit) Pa	P_c (from image) Pa
150	372.669	381.786
200	393.639	298.789
250	138.063	224.964
300	184.782	194.962
350	125.412	173.544

Table 5.4: *Capillary Pressure for channels of different height obtained by means of two different method. P_L is the value obtained from the free parameter of the linear fit of $\rho g H$ v/s $\dot{h}$, while P_c is the capillary pressure obtained by means of the image analysis of the curvature of the water fronts.*

$$\dot{h} = \frac{b^2}{12\eta}\frac{\Delta P}{h} \tag{5.7}$$

We consider that the pressure drop ΔP has two main contributions, namely, the hydrostatic pressure generated by the column of liquid, $P_{hyd} = \rho g H$, and the capillary or Laplace pressure, P_L. Since both the container and the end of the channel are open and exposed to the atmosphere, the atmospheric pressure does not play a role. Therefore, combining with Eq. (5.7) we write and expression for the velocity of the fluid front inside the microchannel as:

$$\dot{h} = \frac{b^2}{12\eta}\frac{\rho g H - P_L}{h} \tag{5.8}$$

We notice that due to the constant velocity of the fluid front along the microchannel Eq. (5.8) is independent of time.

For a Newtonian fluid the viscosity is defined by the Newtonian Constitutive Equation:

$$\sigma = \eta\dot{\gamma} \tag{5.9}$$

As a general approach, a two-parameter power law expression is regularly used to determine the Newtonian or non-Newtonian behavior of a fluid [Morrison, 2001]:

$$\eta(\dot{\gamma}) = m\dot{\gamma}^{n-1} \tag{5.10}$$

Here n and m are constants characterizing the fluid. When the exponent from Eq. (5.10) is equal to 1, $n = 1$, the viscosity value, $\eta = m$, is constant and the fluid is Newtonian, compatible with Eq. (5.9).

So, rearranging Eq. (5.8) we define a shear stress, σ, and a velocity gradient or shear rate, $\dot{\gamma}$, as:

$$\sigma = (\rho g H - P_L)\frac{b}{h} \tag{5.11}$$

$$\dot{\gamma} = \frac{\dot{h}}{b} \tag{5.12}$$

We kept the parameter b is both definitions to obtain a scale independent expression for the stress as well as the shear rate.

Thus, rewriting Eq. (5.9) in term of definitions (5.11) and (5.12), we expected to obtain the viscosity of water, according to equation:

$$\frac{b}{12h}(\rho g H - P_L) = \eta\frac{\dot{h}}{b} \tag{5.13}$$

Plotting our experimental results with expressions (5.11) and (5.12) we obtained the relations shown in Figure 5.11 for different microchannel heights. The value of the exponent n in Eq. (5.10) is obtained by mean of a minimum square method fitting and the value m would represent the viscosity of the fluid.

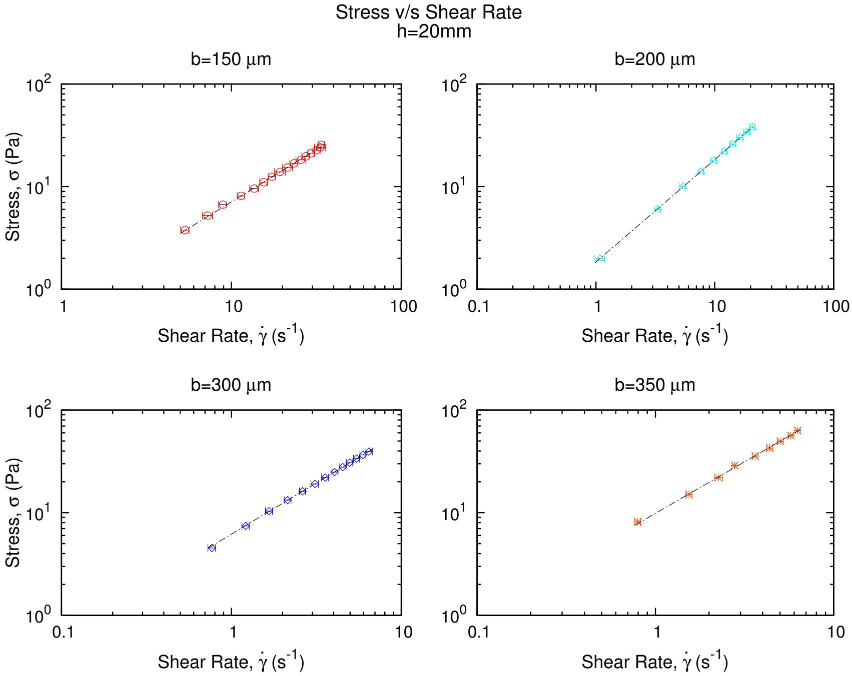

Figure 5.11: *Stress as a function of the shear rate for the water front, in microchannels with different gaps. The relation was obtained through the definitions in Eqs. (5.11) and (5.12). From the fit of Eq. (5.9) we obtained the parameter m and n from Eq. (5.10) which define the fluid as Newtonian. The values of this parameters are shown in Table 5.5.*

The values of the parameters obtained from the fit depend on the height of the channel and are shown in Table 5.5. From the fit we obtained the exponent values for every

Channel Height $b \mu m$	Prefactor m	Exponent n
150	0.67 ± 0.03	1.02 ± 0.01
200	1.84 ± 0.01	0.999 ± 0.003
250	3.2 ± 0.1	1.00 ± 0.01
300	6.18 ± 0.03	0.997 ± 0.003
350	9.8 ± 0.3	1.00 ± 0.02

Table 5.5: *The table shows the values of parameters m and n obtained from the power law fit for different channel height. The exponent n is for every channel gap $n \approx 1$ which according to Eq. (5.10) defines the Newtonian behavior of water.*

microchannel height close to 1, which according to Eq. (5.10) confirms the Newtonian behavior of water. However, the prefactor m does not give the expected value of the viscosity of water, hence, we define the parameter m from the fit as a calibration constant for water, $C_w(b)$, to obtain the viscosity of other fluids.

This observation raises two conditions. First, in order to verify the reliability of our device other fluids need to be considered, through the same method and considering the value of the constant for the used channel compared with the expected viscosity values of that fluid. Second, it is important to be sure that all conditions of the setup have been considered and that nothing in our experiments is been left out. In order to correct this last point the results were compared with a theoretical model of fluid dynamics which is explained in the next section.

5.3 Comparison with theoretical model

In the previous section, we have not obtained the known values of viscosity of water directly from the fit as we expected. Therefore, it had to be calibrated by means of a constant $C_w(b)$.

In order to correct this, an analogy with an electrical circuit was used to introduce the influence of the tube that connects the reservoir with the microchannel [Costa Miracle, 2014]. This model was then compared with our set up, considering the reservoir, the tube and the microchannel as a series of resistances, see Figure 5.12.

We consider a time t_0 when the fluid interface is at the beginning of the microchannel at a position h_0. Then after a time t the position of the front is $h(t)$.

The total pressure drop, ΔP from Eq. (5.7), now has three contributions, the hydrostatic pressure generated by the column of liquid, $P_{hyd} = \rho g H$, the capillary pressure, P_L, and the pressure drop generated by the resistance of the tube connecting the fluid container to the microchannel, ΔP_R, which was not considered in the previous approximation. Again the atmospheric pressure does not play a role and other contributions to the pressure drop, e.g. variations of the channel width and tube cross-section are assumed to be negligible.

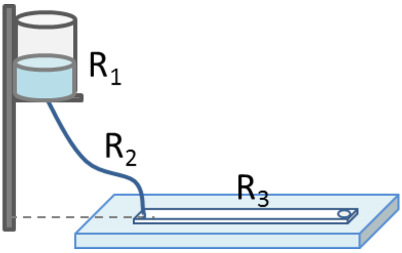

Figure 5.12: *Schematic representation (not on scale) of the system formed by the container which represents resistance R_1, the tube which represents R_2 and the microchannel representing resistance R_3.*

To estimate ΔP_R, we assume that the tube connecting the container and the microchannel has a circular cross-section and that the flow inside the tube obeys Poiseuille's law expressed by:

$$\Delta P_R = \frac{8\eta v_t l_t}{r^2} \tag{5.14}$$

where η is the viscosity of the fluid, l_t is the length of the tube, r is the radius of the tube, and v_t is the average flow velocity in the tube.

Under these assumptions the total driving pressure inside the microchannel is:

$$\Sigma P = \rho g H - \frac{8\eta v_t l_t}{r^2} - P_L \tag{5.15}$$

Taking into account that, due to mass conservation, $\dot{h}bw = v_t \pi r^2$, we can write the following equation for the velocity of the front inside the microchannel:

$$\dot{h}(t) = \frac{\rho g H - P_L}{\eta \left(\frac{12h(t)}{b^2} + \frac{8bwl_t}{\pi r^4} \right)} \tag{5.16}$$

Eq. (5.16) shows that if our experimental setup is such that the resistance associated to the fluid flow in the microchannel is much smaller than the one associated to the tube, then we can assume that $\frac{12h(t)}{b^2} \ll \frac{8bwl_t}{\pi r^4}$ and Eq. (5.16) can be simplified to:

$$\dot{h}(t) \approx \frac{\pi r^4 (\rho g H - P_L)}{\eta 8bwl_t} \tag{5.17}$$

This relation implies that the front velocity does not depends on the position, $h(t)$, and it is approximately constant as has been proven experimentally for different channel heights in section 5.1. This approach also explains, what we see in Figure 5.7, where the velocity is inversely proportional to the microchannel heights.

Notice that, as time progresses and $h(t)$ increases, this approximation becomes less accurate, which implies that this linear regime is valid for either short microchannels or early times. Similarly the constant velocity approximation may fail for microchannels with small gaps, b, such as the cases shown in Figures 5.4 and 5.5 for channels with gaps of $b = 100$ and $50\,\mu m$ respectively.

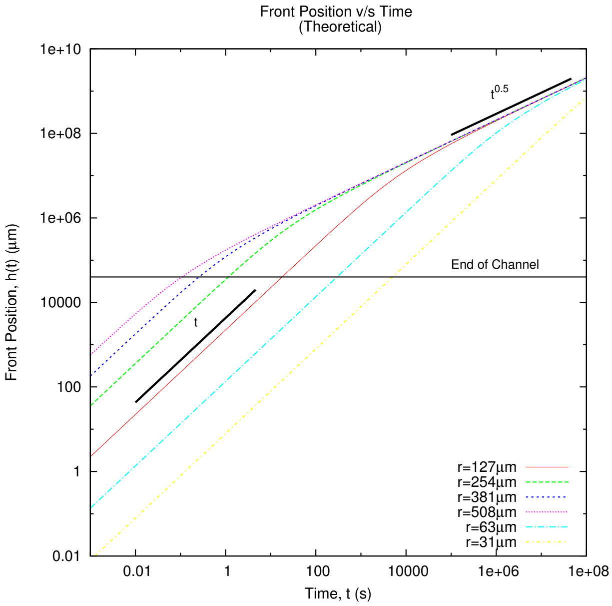

Figure 5.13: *Theoretical front position $h(t)$ for different values of the radius of the tube r, Eq. (5.18). The value of $r = 127\mu m$ corresponds to the radius used in the experimental setup. The thick lines represent $t^{0.5}$ and t growth exponents. The geometrical parameters used in the plot are those of the experimental setup with a pressure of $\rho g H - P_L = 3000\,Pa$ and the viscosity of water, $\eta = 1\,mPas$. This image is courtesy of Enric Costa and was taken from [Costa Miracle, 2014].*

In the general case, when the above assumption does not apply, integration of Eq. (5.16) provides the following expression for the average position of the front, $h(t)$:

$$\begin{aligned} h(t) = &-\frac{2}{3}\frac{b^3 l_t w}{\pi r^4} + \\ &+ \left[\left(h(t_0) + \frac{2}{3}\frac{b^3 l_t w}{\pi r^4} \right)^2 + \frac{b^2(\rho g H - P_L)}{6\eta}(t - t_0) \right]^{\frac{1}{2}} \end{aligned} \tag{5.18}$$

In Figure 5.13 we observe the crossover between both regimes. The early evolution of the front is dominated by a regime where the velocity is approximately constant, whereas for longer times the system decays to the Washburn regime where $h(t) \approx t^{1/2}$ [Washburn, 1921].

From Eq. (5.17), we can obtain the following relation between the hydrostatic pressure and the (constant) front velocity:

$$\rho g H = \eta \frac{8 b w l_t}{\pi r^4} \dot{h} + P_L \tag{5.19}$$

Comparing Eqs. (5.6) and (5.19), we measure the viscosity of water from our experiments using:

$$\eta = A\frac{\pi r^4}{8bwl_t} \tag{5.20}$$

where A is fitted from experimental data. The values obtained for different channels are shown in Table 5.6 along with the viscosity values obtained for different channel heights, through Eq. (5.20).

Channel Height μm	A	η (from fit) $mPas$
150	655160	1.050
200	882122	1.048
250	1055780	1.003
300	1395320	1.105
350	1600290	1.087

Table 5.6: *Fit parameters obtained for water for different channel heights. The table shows the slope values, A, and the viscosity values obtained from Eq. (5.20).*

The accuracy of these results compared with the expected values for water viscosity is a proof that combining our device and method with the proper theory we have developed a viscometer which may not need calibration, but still needs to be proven with other fluids.

5.3.1 Effects of the capillary height b

We performed measurements in channels of different heights, which give us the opportunity to scale our viscosity results for an extended range of shear rate. Equation (5.19) can be written in scaling form as:

$$\frac{\pi r^4(\rho g H - P_L)}{8wb^2 l_t} = \eta\frac{\dot{h}}{b} \tag{5.21}$$

By using the definition of the shear rate, $\gamma = \dot{h}/b$, and defining the rescaled shear stress, σ_{rs}, as:

$$\sigma_{rs} = \frac{\pi r^4(\rho g H - P_L)}{8wb^2 l_t} \tag{5.22}$$

In analogy with Eq. (5.9), Eq. (5.21) can be rewritten, independently of the geometrical parameters of the microchannel, as:

$$\sigma_{rs} = \eta\dot{\gamma} \tag{5.23}$$

Combined with Eq. (5.10), the previous expression may be expressed as a function of a shear rate exponent, n, as:

$$\eta = \frac{\sigma_{rs}}{\dot{\gamma}^n} \tag{5.24}$$

Using the definition of the rescaled stress in Eq. (5.22) and the shear rate definition, $\dot{\gamma} = \frac{h}{b}$, we fit our experimental data to Eq. (5.24) for different channel heights, as displayed in Figure 5.14. If the exponent $n = 1$, then we assume that the fluid is Newtonian. The fitted values obtained for the viscosity and the shear rate exponent are shown in Table 5.7.

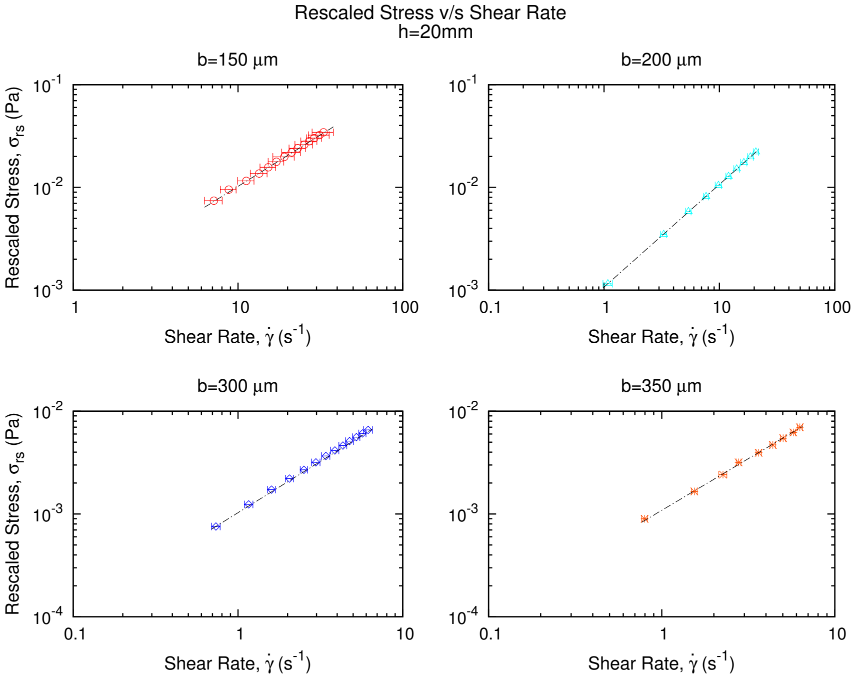

Figure 5.14: *The figure shows the rescaled stress as a function of the shear rate for 4 channels of different height, $b = 150, 200, 300$ and $350\,\mu m$. The dashed lines for each height correspond to the power law fit. The values of the parameters obtained from the fit are shown in Table 5.7.*

Channel Height μm	Viscosity $\eta\,(Pas)$	Viscosity Exponent n
150	0.00102± 0.00002	1.001± 0.006
200	0.00107±0.00001	0.999 ± 0.003
250	0.00099±0.00003	1.00 ± 0.01
300	0.00102±0.00001	0.997 ± 0.003
350	0.00108±0.00003	1.00 ± 0.02

Table 5.7: *Fit parameters obtained from Eq. (5.24), for the viscosity, η, and the shear rate exponent, n, of water for channels of different height. The error values are given from the fitting method. This results are presented in Figure 5.14 for 4 different channel heights.*

The viscosity of the fluid for each value of the shear rate is obtained rearranging

Eq. (5.16) in terms of the velocity of the fluid inside the microchannel, obtaining the following viscosity expression:

$$\eta = \frac{\rho g H}{\dot{h}} \frac{8bwl_t}{\pi r^4} \tag{5.25}$$

The whole experimental set up system is considered in Eq. (5.25). This expression allows us to calculate the viscosity of the fluid for every independent value of the shear rate, see Figure 5.15. This converts our method from a simple device that give a single viscosity values for a fluid, to a system that allow us to obtain the viscosity values of the fluid for different values of the shear rate, transforming a microviscosimeter into a microrheometer.

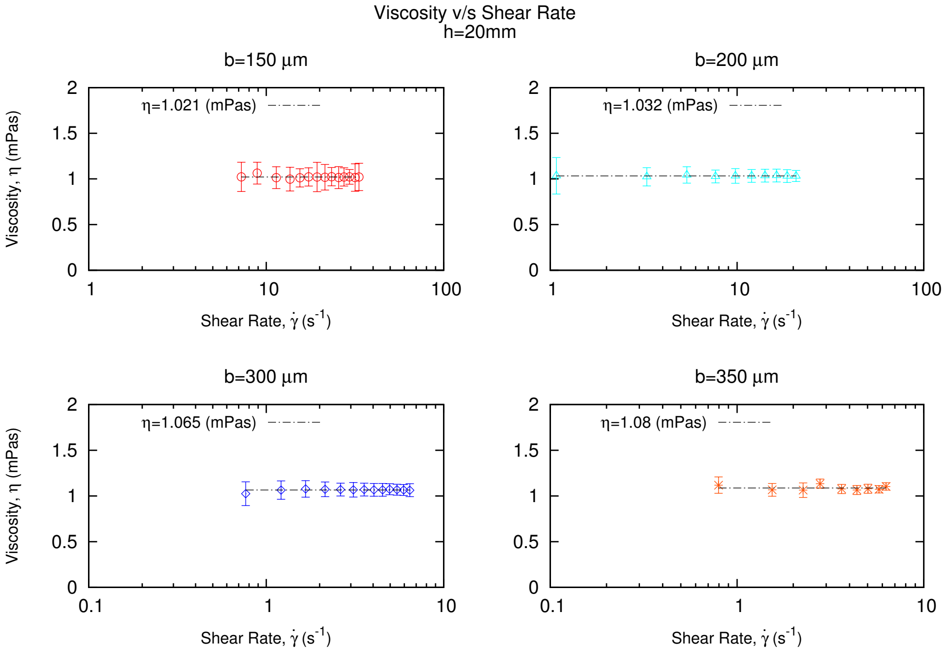

Figure 5.15: *The figure shows the viscosity of water as function of the shear rate for four channels of different height,* $b = 150,\ 200,\ 300$ *and* $350\,\mu m$. *In this figure we can appreciate how we obtain a values of the viscosity for each value of the shear rate, which is what rheometers do.*

From Figures 5.14 and 5.15 we observe that the results for channels with high gaps are complemented with the results for channels of lower gaps. This is the advantage of the scaling which enable us to perform experiments with different channel heights, b, and still have a consistent and complementary result in both cases.

Combining the results for various channels, we are able to extend the viscosity estimation for almost 2 decades. Figures 5.16 and 5.17 display the combined results for the channels of $b = 300$ and $150\,\mu m$.

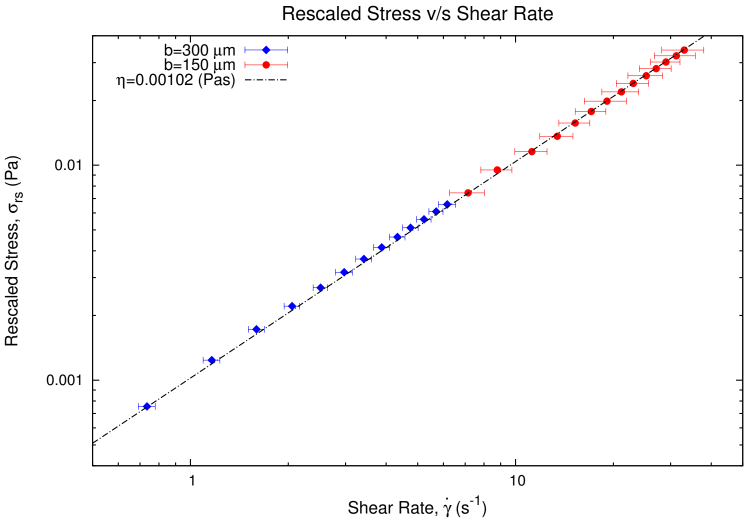

Figure 5.16: *Rescaled stress as a function of the shear rate for 2 channels of different height,* $b = 300$ *and* $150\,\mu m$*, with its corresponding power law fit with an exponent* $n = 1.006$*, which depicts the Newtonian behavior of water and the viscosity value* $\eta = 1.02 \pm 0.02\, mPas$*, which is the expected water viscosity of water.*

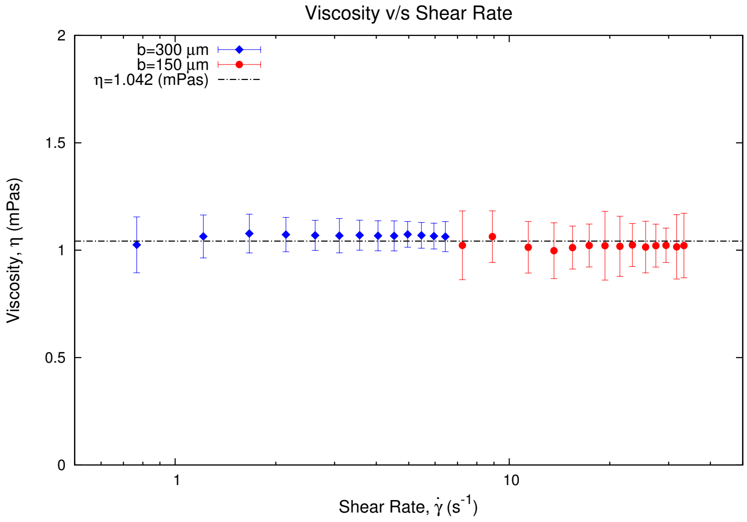

Figure 5.17: *Viscosity as function of the shear rate for 2 channels of different height,* $b = 300$ *and* $150\,\mu m$*, with its viscosity value considering both channel* $\eta = 1.042 \pm 0.005\, mPas$ *according to a constant value fit, which is consistent with the value obtained using the power law fit shown in Figure 5.16.*

5.4 Conclusions

We have tested several microchannel of different heights, or gaps, with water in order to characterize them. We first ensure the heights of the channels using a syringe pump which gave us the effective values of the microchannel gaps. This were the values used along the whole chapter.

By means of the insertion of a tube of radius $r = 127\,\mu m$, that connects the fluid container with the microchannel, we were able to control the advancement of the front inside the microchannels, obtaining a linear regime between its position as a function of time, which results in a water-air interface that moves at a general constant velocity along the channel.

We developed two method for measuring the viscosity of the fluid. The first one does not consider the tube influence in the system. Even though, by means of a power law fit, we obtained a confirmation of the Newtonian behavior of water, the viscosity values had to be calibrated according to a constant which depends on the height of the channels, $C_w(b)$. On the other, hand we compared with a theoretical model which includes the tube influence in the system, in this case the viscosity values of water were obtained directly from the linear fit of the relation between the pressure and the velocity of the fluid inside the channel, but considering the geometrical parameter of the tube, Table 5.6 displays this results. The viscosity values obtained using this theoretical approach are in good agreement with the literature, refer to Appendix C.

By means of the scaling theory developed in subsection 5.3.1 we established a relation between a rescaled stress at which the fluid is submitted and the shear rate response of the fluid inside the channel. Using a power law fit, again we obtained confirmation of the Newtonian behavior of water and the viscosity values obtained for microchannels of different heights are comparable with the general viscosity results obtained with the previous approach, this results are shown in Table 5.7 along their corresponding fitting errors. The biggest advantage of the scaling is that we are able to combined the results for channels with different gaps, extending the shear rate ranges to study the behavior of the fluid. As well, we define a viscosity expression, Eq. (5.25), which allows our method to determine a viscosity values at each different shear rate response of the water front, which is an approach to how rheometers work.

However, all this method need to be tested with other Newtonian fluids to ensure that the viscosity values obtained with our device and method are reliable and comparable with other viscometers and rheometers. This matter will be address in the next chapter.

Viscosity of Newtonian fluids

In order to extend the results obtained for water and verify the reliability of our device and method, to measure the viscosity of fluids, we decided to test other Newtonian fluids as Ethylene-glycol and Glycerol at low volume concentrations. We chose these fluids because they are well characterized in literature and at a certain volume concentration its density is the same as blood. Since our aim is the understanding of blood viscosity in addition to these fluids we have obtained the viscosity of Blood Plasma which is known to present Newtonian behavior.

The first section of this chapter, section 6.1 will describe the behavior inside the microchannel observed for these three Newtonian fluids. Ethylene-glycol at 2 different volume concentrations, Glycerol at 20% volume concentration and finally Blood Plasma. This will also be compared with the data obtained for water in the previous chapter. Section 6.2 is dedicated to present the results for the viscosity values of these fluids using the calibration constant $C_w(b)$ and the viscosity values obtained with the theoretical modelling which includes the tube in the system, both presented in the previous chapter in sections 5.2 and 5.3 respectively. In section 6.3 the results from our device will be compared with those obtained with of a macroscopic rheometer to show its feasibility. Last section 6.4 will present a summary and conclusions of this chapter.

6.1 Newtonian fluids

We have analized the moving front along microchannels of $b = 300$ and $150\,\mu m$ for Ethylene-Glycol at a 40% volume concentration and Blood Plasma and we have obtained a value for its viscosities. Just as for water in the previous chapter, the first step was to confirm the constant velocity behavior along the channel. This is shown in Figure 6.1 for ethylene-glycol and blood plasma compared with water. Here the data points are drawn along with the theoretical behavior of the position expected from:

$$\begin{aligned} h(t) = & -\frac{2}{3}\frac{b^3 l_t w}{\pi r^4} + \\ & + \left[\left(h(t_0) + \frac{2}{3}\frac{b^3 l_t w}{\pi r^4} \right)^2 + \frac{b^2(\rho g H - P_L)}{6\eta}(t - t_0) \right]^{\frac{1}{2}} \end{aligned} \tag{6.1}$$

The value of the viscosities in Eq. (6.1) of these two fluids, were taken from literature, $\eta_{et40} = 2.86\,mPas$ for ethylene-glycol 40% and $\eta_{BP} = 1.81\,mPas$ for blood plasma, references to the values of the fluids properties are shown in Appendix C.

The time exponents from equation $h(t)-h_0 = v(t-t_0)^\nu$ are $\nu = 1.01$ for ethylene-glycol 40% and $\nu = 0.98$ for blood plasma. These value of the exponents are consistent with the expected constant velocity behavior observed for water.

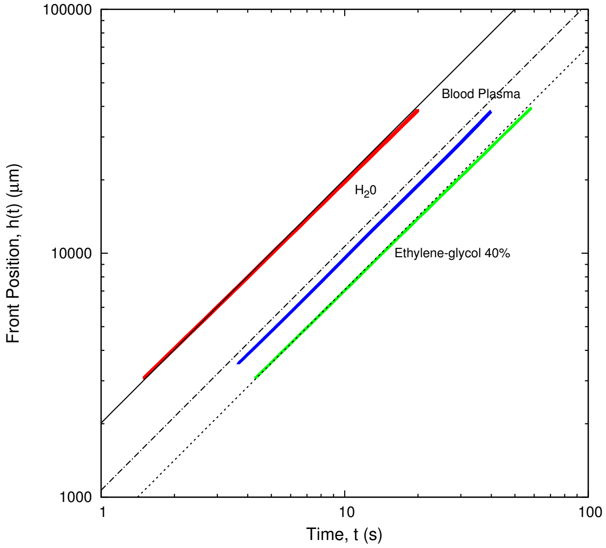

Figure 6.1: *Position as a function of time for Water (red), Ethylene-glycol 40% (green) and Blood Plasma (blue) measured at* $\rho g H \approx 3000\,(Pa)$*. The lines represent the expected behavior of the position of each fluid front from Eq.(6.1) using the bibliographical values of the viscosity of each fluid at 20°C:* $\eta_w = 1.002$*,* $\eta_{et40} = 2.86$ *and* $\eta_{bp} = 1.81\,(mPas)$*. The time exponent values are* $\nu = 1.01$ *for ethylene-glycol 40% and* $\nu = 0.98$ *for blood plasma.*

This behavior is displayed for the fluid front velocities in Figure 6.2, where we may observe a constant behavior of the mean velocity of the fluids at the center of the microchannel along $\Delta h = 2\,mm$. From Figure 6.2, we infer that for fluids with higher viscosities the velocity of the front is smaller than for lower viscosities fluids. We can deduce this observing how the velocity of the most viscous fluid in the plot (ethylene-glycol 40%) has the lowest mean velocity, while water which has the lowest viscosity of the tested fluids, has the highest mean velocity. We can also deduced from this figure, that for fluids with a higher viscosity, the dispersion of the velocity profile decreases.

With these new test fluids, we have developed the same steps that we perform with water in the previous chapter. Since our knowledge of these fluids tells us that they are Newtonian, we first obtained the linear fit to the data of the hydrostatic pressure exerted as a function of the velocity response of the fluid. We have done this for two microchannel heights $b = 150$ and $300\,\mu m$, and we have compared this behavior with the one obtained for water. The results for the microchannels gaps are shown in Figure 6.3. From these representation fits, we obtain the capillary pressure values, P_L, see Table 6.1, which will allow us to define the effective pressure, $\rho g H - P_L$.

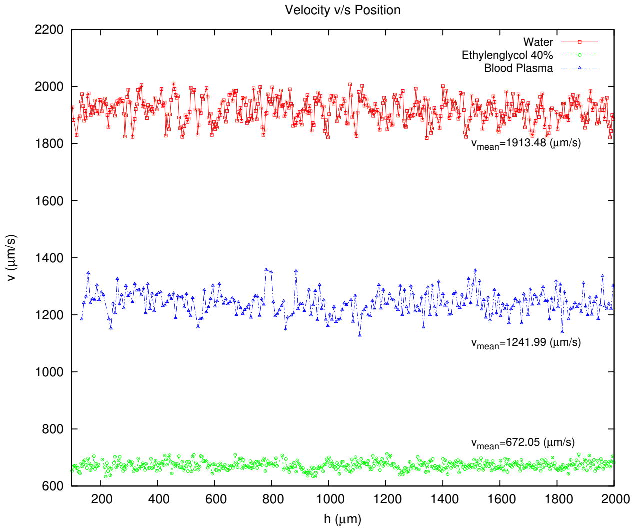

Figure 6.2: *Velocity profile at the center of the channel in a* $2\,mm$ *observation window, at a fluid column height* $H = 0.290\,m$*. The values of the mean front velocity in this interval are: Water (red)* $\dot{h} = 1913.48\,\frac{\mu m}{s}$*, Ethylenglycol 40% (green),* $\dot{h} = 672.054\,\frac{\mu m}{s}$ *and Blood Plasma (blue),* $\dot{h} = 1241.99\,\frac{\mu m}{s}$*. We infer from this figure that the velocity of the mean front decreases with higher viscosity fluids. As well, we observe that for higher viscosity fluids, the dispersion of the velocity profile decreases.*

Channel Height Fluid	$b = 150\,(\mu m)$ $P_L\,(Pa)$	$b = 300\,(\mu m)$ $P_L\,(Pa)$
Water	355.03	184.78
Etgl. 44%	236.67	145.90
Gl. 14%	165.43	216.23
Gl. 20%	256.01	334.24
Plasma A	356.94	201.60
Plasma B	221.85	340.26

Table 6.1: *The table presents the capillary pressure values obtained from a linear fit from Figure 6.3 for various Newtonian fluid.*

6.2 Viscosity Results of Newtonian Fluids

6.2.1 Viscosity using the calibration constant C_w

To compared the viscosity approximation by means of the calibration constant $C_w(b)$, we first need to define our parameters. As explained in the previous chapter the shear rate is defined as:

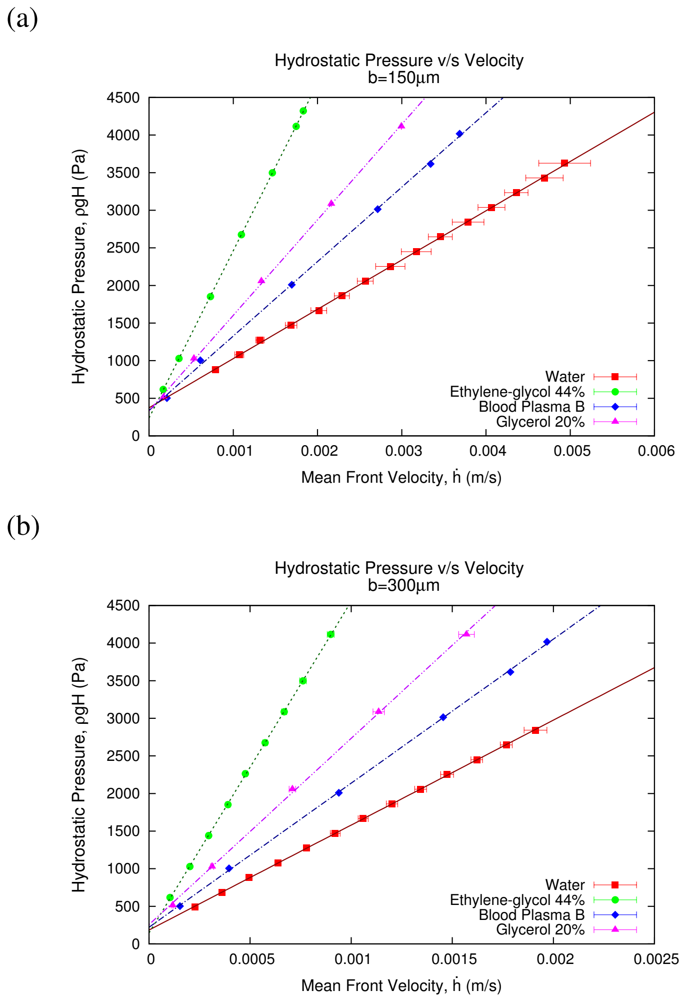

Figure 6.3: *Hydrostatic pressure as a function of the velocity for Ethylene-glycol 44%, Glycerol 20% and Blood Plasma, sample B compared with Water. Figure a) shows the results for a channel gap of* $b = 150\ \mu m$ *and figure b) for a microchannel of* $b = 300\ \mu m$. *From the linear fit we may obtained the values correspondent to the capillary pressure associated with each fluid, shown in Table 6.1.*

$$\dot{\gamma} = \frac{\dot{h}}{b} \tag{6.2}$$

On the other hand, the stress is defined as:

$$\sigma = (\rho g H - P_L)\frac{b}{\dot{h}}, \tag{6.3}$$

The stress values are calculated for each column height, H, and its associated shear rate and for the two microchannel gaps b. Plotting the stress definition from Eq. (6.3)

Channel Height μm	Calibration Constant $C_w(b)$
150	0.67
300	6.18

Table 6.2: *The table shows the values of the calibration constant $C_w(b)$ of the viscosity of water for two different channel heights. This calibration values were obtained in the previous chapter.*

as a function of the shear rate, Eq. (6.2) on a logarithmic scale, Figures 6.4 and 6.5, we determine the values of the exponent n for the studied fluids which would confirms their Newtonian behavior, according to:

$$\sigma = \eta \dot{\gamma}^n \tag{6.4}$$

In agree with our results the exponents are close enough to $n = 1$ for every Newtonian fluid tested. The viscosity of the tested fluids corresponding to each microchannel height are obtained normalizing the term that accompanies $\dot{\gamma}$ with the value of $C_w(b)$ shown in Table 6.2 correspondent to each height of the microchannel. For the three studied fluids, using this process we obtained the viscosity values shown in Table 6.3.

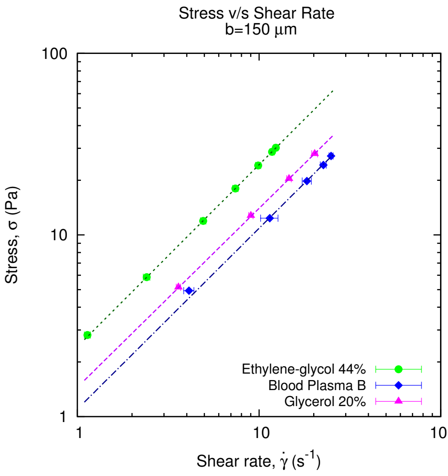

Figure 6.4: *Stress as a function of the shear rate for Newtonian fluids at a channel of height $b = 150\,\mu m$. Fitting Eq. (6.4), The exponent values are $n = 1.001 \pm 0.003$ for ethylene-glycol 44%, $n = 0.98 \pm 0.02$ for glycerol 20% and $n = 0.99 \pm 0.03$ for blood plasma B.*

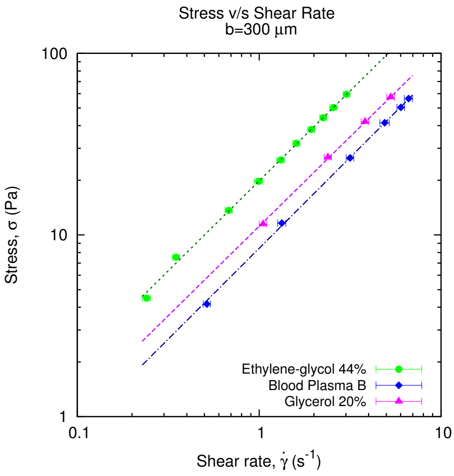

Figure 6.5: *Stress as a function of the shear rate for Newtonian fluids at a channel of height $b = 300\,\mu m$. Fitting Eq. (6.4), the exponent values are $n = 0.99 \pm 0.01$ for ethylene-glycol 44%, $n = 0.98 \pm 0.02$ for glycerol 20% and $n = 1.00 \pm 0.01$ for blood plasma B.*

Fluid	Viscosity, $\eta\,(mPas)$ $b = 150\,\mu m$	$b = 300\,\mu m$
Ethylene-glycol 44%	3.66 ± 0.02	3.21 ± 0.03
Glycerol 20%	2.16 ± 0.1	1.81 ± 0.05
Blood Plasma B	1.64 ± 0.1	1.37 ± 0.03

Table 6.3: *Viscosity values of various Newtonian fluids using the calibration with the values $C_w(b)$ for two channel of different height. With $C_w(b = 150) = 0.67$ and $C_w(b = 300) = 6.18$.*

We see that there is a high gap between the viscosity values corresponding to different channel heights. To ensure that this is not an extensive problem of the device, but instead of the calibration method that depends on the height of the microchannel, we calculate the viscosity values using the theoretical approach of the rescaled stress developed in section 5.3.

6.2.2 General viscosity using a linear approximation

Adjusting a linear fit to the results shown in Figure 6.3 we have that from equation $\rho gH = A\dot{h}+P_L$, the independent term represents the capillary pressure and the term A with $\dot{h}$ contains the viscosity of the fluid, which is obtained through the expression $\eta = A\frac{\pi r^4}{8bwl_t}$. These general viscosity values are presented in Table 6.4 for both microchannel gaps studied, $b = 150$ and $b = 300\,\mu m$.

Channel Height Fluid	$b = 150\,(\mu m)$ $\eta \pm \delta\eta\,(mPas)$	$b = 300\,(\mu m)$ $\eta \pm \delta\eta\,(mPas)$
Water	1.05 ± 0.02	1.105 ± 0.006
Etgl. 44%	3.52 ± 0.01	3.49 ± 0.02
Gl. 14%	1.68 ± 0.03	1.61 ± 0.02
Gl. 20%	2.01 ± 0.01	1.96 ± 0.02
Plasma A	1.75 ± 0.01	1.77 ± 0.02
Plasma B	1.57 ± 0.01	1.52 ± 0.02

Table 6.4: *General viscosity values for several Newtonian fluids using the expression $\eta = A\frac{\pi r^4}{8bwl_t}$, where the value m is obtained from the linear fit of equation $\rho gH = A\dot{h} + P_L$.*

The viscosity values shown in Table 6.4 demonstrate that the model gives a good approximation to the viscosity of the fluids compared with literature.

6.2.3 Viscosity using the rescaled stress

Even though we have obtained accurate values of the viscosity for both microchannel heights, we are interested in determine the viscosity values for each different shear rate at which the fluid is submitted inside the microchannel. As we did with water in the previous chapter, if we rescale the stress with respect to the channel height we have:

$$\sigma_{rs} = \frac{\pi r^4(\rho g H - P_L)}{8wb^2 l_t} \tag{6.5}$$

which will allow us a broader analysis of the viscosity unifying both channels.

Considering expressions in Eqs. (6.2) and (6.5), we obtain mean values of the viscosity for Ethylene-glycol 44% and Blood Plasma A, combining the results for both channels simultaneously has shown in Figure 6.6, compared with water.

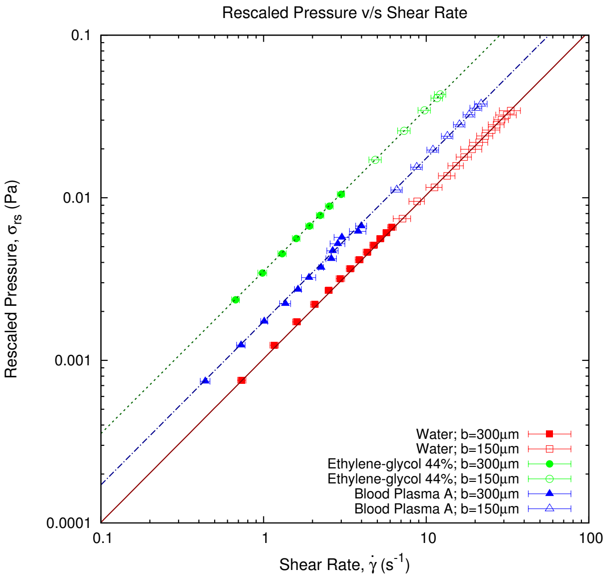

Figure 6.6: *Rescaled pressure as a function of the shear rate for Newtonian fluids displayed in logarithmic scale. The values of the slopes for each fluid are:* $n = 1.006$ *for water (red),* $n = 0.998$ *for Ethylene-glycol at 44% (green) and* $n = 1.004$ *for Blood Plasma A (blue). According to Eq. (6.4) the viscosity values, from the fit, for these fluids are:* $\eta_w = 1.04 \pm 0.01$, $\eta_{et44} = 3.52 \pm 0.01$ *and* $\eta_A = 1.72 \pm 0.01$.

The viscosity values of the studied Newtonian fluids are obtained using:

$$\eta = \frac{\rho g H}{\dot{h}} \frac{8bwl_t}{\pi r^4} \tag{6.6}$$

Averaging the values of the viscosities we have the general viscosity values shown in Table 6.4. The viscosity results for Ethylene-glycol 44% and Glycerol 20%, compared with water, are shown in Figure 6.7, using the rescaled stress value for different microchannel heights extending the shear rate spectrum in almost two decades.

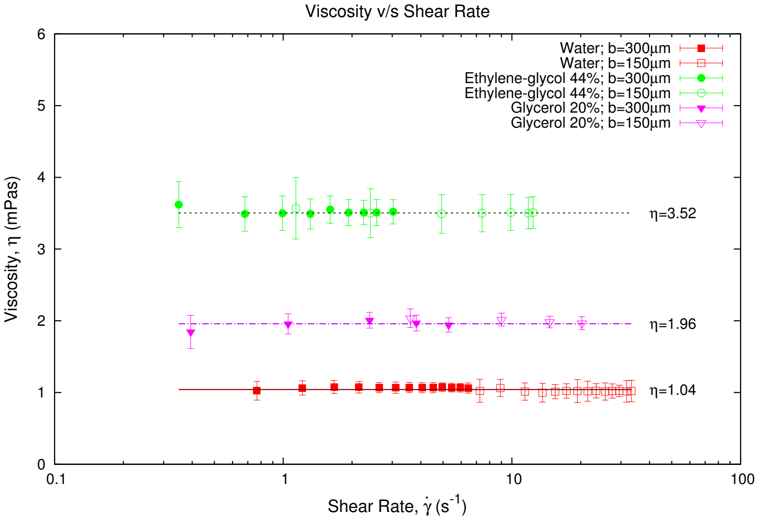

Figure 6.7: *Viscosity as a function of the shear rate for Newtonian fluids displayed in semi-logarithmic scale. For Ethylene-glycol 44% (green)* $\eta_{et44} = 3.52 \pm 0.01\, mPas$ *and Glycerol 20% (magenta)* $\eta_{gl20} = 1.96 \pm 0.03\, mPas$*, compared with the viscosity results for water. measure with our device and method at two different microchannel heights* $b = 300\,\mu m$ *(solid points) and* $b = 150\,\mu m$ *(empty points)*

.

Human Blood Plasma

We have determined the viscosity of Human Blood Plasma using different blood plasma samples. The samples were obtained from the Hematology Department of the Hospital Clinic Barcelona. These have been referred along the chapter as Sample A and B. We have measure the viscosities of this two samples using two different channels of $b = 150$ y $b = 300\,\mu m$ and we obtained the viscosities using the rescaled expressions for stress Eq. (6.5) and its relation to the shear rate Eq. (6.4). We have also obtained the viscosities of both plasma samples using the viscosity expression from Eq. (6.6) which are well distinguished between them as shown in Figure 6.8.

6.3 Comparison with the Rheometer Results

Our results are already in agree with the literature, but in order to ensure the accuracy of the viscosity values we measured the tested fluids with a rheometer. In this case, we used a typical cone-plate rheometer, which is a classical type of rheometer usually used in industry. The measurements were taken with a Malvern Company Rheometer at the Complex Fluids Laboratory at the Centre de Recerca Matemàtica. We performed the measures using a flat surface at the bottom and an a cone-shaped geometry in the upper surface. The upper geometry is $5\,cm$ diameter and 1° of inclination. The test fluid is set over the flat surface and the tip of the upper conical surface is set at a gap of $30\,\mu m$

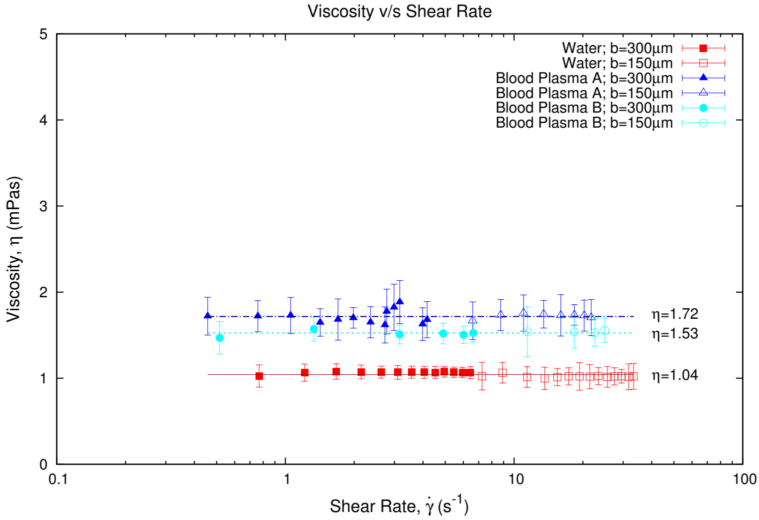

Figure 6.8: *The figure shows the viscosity of two different blood plasma samples: sample A (blue) and sample B (cyan) compared with water (red). The viscosity values are obtained by mean of Eq. (6.6) as function of the shear rate for two different channels heights. The viscosity values for each samples are* $\eta_A = 1.72 \pm 0.01\ (mPas)$ *and* $\eta_B = 1.53 \pm 0.01\ (mPas)$.

from the lower surface, while the fluid extends along the whole upper surface.

The fluid, between the bottom and upper surface, is submitted to a rotational stress by the upper surface which generate a shear rate response. The viscosity of the fluid is obtained by means of the relation between the rotational stress applied and the shear rate response from the fluid.

We decided to test first fluids with high viscosities, ethylene-glycol at 100% volume concentration and glycerol at 50% volume concentration, Figure 6.9 shows the viscosity response of these two fluid given by the rheometer.

From Figure 6.9, we see that for low shear rates (less than $1s^{-1}$) the results obtained with a cone-plate rheometer are not stable and show a sort of shear thinning behavior for these Newtonian fluids, which is misleading, if we want to measure at low shear rates.

Now that we understand the fails of the rheometer we are able to compare its viscosity values with those obtained with our microrheometer. Figure 6.10 shows the results for three of the studied fluids comparing between the viscosity values obtained with our microrheometer device and the the values obtained from the cone-plate rheometer.

We observe that at low shear rate our results are more stable than with the cone-plate rheometer. However, some differences in the values of the viscosity are observed once the measure with the cone-plate rheometer is stable. The viscosity values obtained, through both devices, are compared in Table 6.5 with the bibliographical values of the studied fluids viscosities. Although the range of operation of the cone-plate rheometer is wider than the one of our device, we may establish that the viscosity results from our device are consequent with literature and considering the error from our device its are

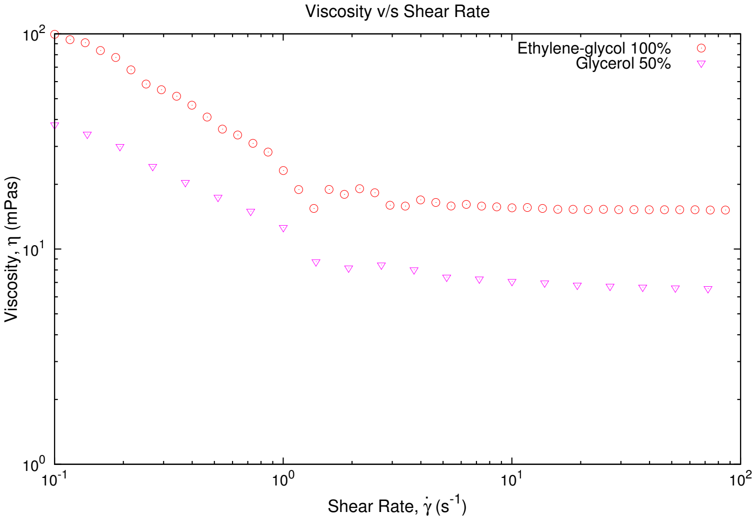

Figure 6.9: *Viscosity as a function of the shear rate for 2 Newtonian fluids of constant viscosity, Ethylenglycol at 100% and Glycerol 50%. These results were obtained using a cone-plate rotational rheometer. We see that there is a stabilization and convergence to a fixed viscosity value from* $\dot{\gamma} > 1\,s^{-1}$*. Using the Newtonian model fit provided by the software of the rheometer we obtained the viscosity values of* $\eta_{et} = 17.4028\,(mPas)$ *for ethylene-glycol and* $\eta_{gl50} = 6.593\,(mPas)$ *for glycerol 50%.*

also consistent with the stable viscosity results from the rheometer.

Fluid	Microdevice	Rheometer	bibliog.
Ethylene-glycol 44%	3.52 ± 0.01	3.3	3.34
Ethylene-glycol 40%	2.87 ± 0.02	2.7	2.86
Glycerol 20%	1.96 ± 0.03	1.93	1.76

Table 6.5: *Viscosity comparison of the Newtonian fluids using different devices in* $mPas$*. References can be addressed in Appendix C*

Fluid	Microdevice	Rheometer	bibliog.
Blood plasma A	1.72 ± 0.01	1.84	1.50-1.81
Blood plasma B	1.53 ± 0.02	1.62	1.50-1.81

Table 6.6: *Viscosity comparison of the two different blood plasma samples in* $mPas$*. References can be addressed in Appendix C*

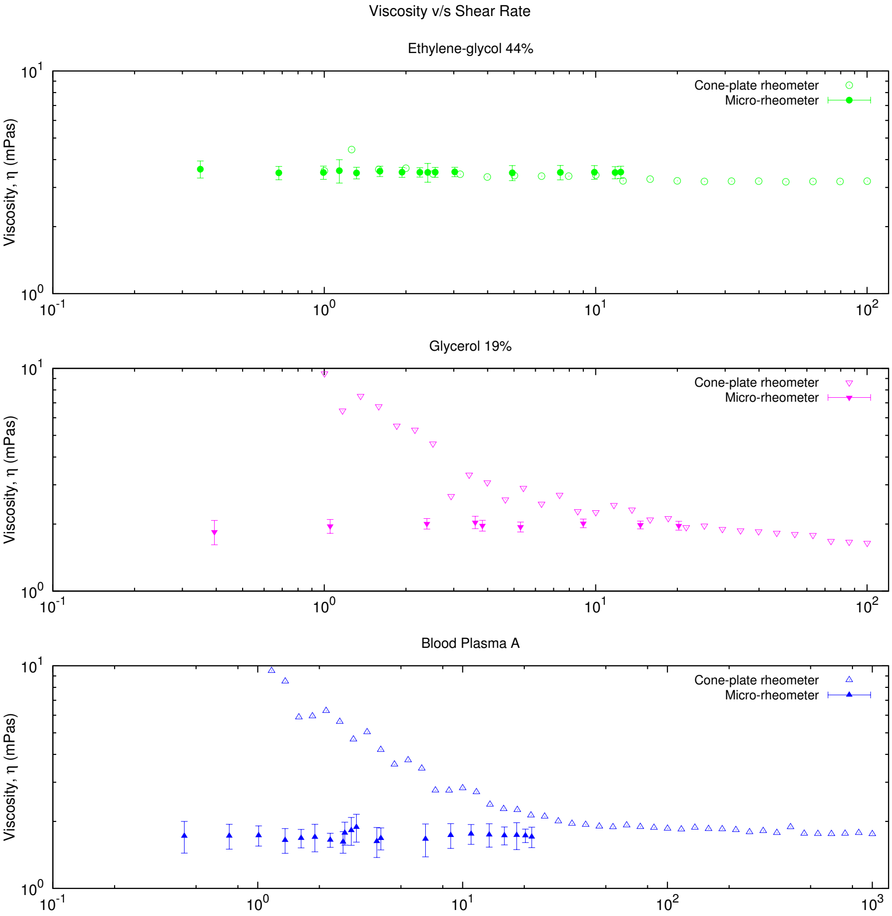

Figure 6.10: *Comparison of Newtonian fluids viscosity between a cone-plate rheometer and our microrheometer. The top image shows the viscosity results for ethylene-glycol 44%, the center image the glycerol 20% viscosity results and the bottom image shows the viscosity results for blood plasma sample A.*

6.4 Conclusions

We have been able to extend our results for water to other Newtonian fluids, by means of 3 different methods. First, we used the calibration constant $C_w(b)$ obtained for water in Chapter 5, although, this method presented remarkable differences between the height of the microchannels. Second, since we used Newtonian fluids we obtained a general value of the viscosity of the test fluids using a linear fit from the representation of the effective pressure, $\rho g H - P_L$ as a function of the velocity of the fluid front, $\dot{h}$, using the geometrical parameters of the experimental setup. Last, we determined the viscosity of the fluids from the Newtonian Constitutive Equation, $\sigma_{rs} = \eta\dot{\gamma}$, using a rescaled values of the stress, Eq. (6.5), and the definition of the shear rate, Eq. (6.2). With these definitions we defined a viscosity equation, Eq. (6.6) which delivers a values of the viscosity of the fluid for each value of the shear rate.

We chose as test fluids: Ethylene-glycol and Glycerol, since they are well characterized in literature, making easier to compared our results, we successfully determined the viscosity for these fluid at different volume concentrations. We compared our results with the ones obtained using a cone-plate rheometer. This comparison exhibits that our result at low shear rates and low viscosities are more accurate that the ones delivered by the rheometer. The rheometer, instead of showing a steady constant behavior of the viscosity, shows a sort of shear thinning for Newtonian fluids at $\dot{\gamma} < 1\,s^{-1}$, see Figures 6.9 and 6.10.

We were also capable to determine the viscosity of different blood plasma samples without observing overlap on its values which gives us a good accuracy of our device and method.

The results obtained with our device and method are shown in Tables 6.5 and 6.6, compared with the values obtained with the values from cone-plate rheometer and from the values taken from literature. All details regarding to the fluids properties are presented in Appendix C.

CHAPTER 7

Dynamics of front advancement in a immiscible two-fluids system

When the experiment with blood started, we encounter difficulties controlling the sedimentation at the bottom of the recipient that contained the blood sample. In order to correct this, we performed a modification to the setup, explained earlier in section 4.2 of Chapter 4. In this modification, the hydrostatic pressure was exerted by a fluid of the same density of blood set in the container and the tube was filled with the blood sample. We used Glycerol at 19%, since its density is approximate the blood density, ($\approx 1050\, kg/m^3$).

This situation justifies the analysis of the dynamics of front advancement in a system consisting of an immiscible two-phase flow. This chapter will be dedicated to explain and analyze the simplest situation for this modification, in which both fluids are Newtonian and with non-zero viscosity contrast.

This chapter is organized as follows. Section 7.1, presents our experimental results for the velocity of the front in the case of immiscible two-phase flow. Section 7.2 is devoted to compared with theoretical framework [Costa Miracle, 2014], that allows to interpret these observations and calculate the unknown viscosity of the fluid inside the microchannel. Last, section 7.3 presents the discussion and conclusions of this chapter.

7.1 Experimental results

We analyze and explain experimental observations regarding the two-phase system, which cannot be understood in terms of the theory developed in Chapter 5. These new phenomenology includes the result that the advancement of the capillary fluid flow undergoes an initial acceleration, in contrast to the constant front velocity we observed in the case of a single phase flow.

The basic experimental setup is described in section 4.2 and the modification to the experimental setup described in this chapter is shown in Figure 7.1. The main variation with respect to the experiments described in Chapters 5 and 6, is that now we fill the deposit with a liquid of known viscosity, a glycerol dilution at 19% of volume concentration which viscosity values were presented in the Chapter 6 and its bibliographical references can be addressed in Appendix C. . We then study the properties of the dynamics of the fluid front of a second fluid which is being pushed into the microchannel by the column of glycerol solution. We have used two Newtonian fluids to measure their viscosity using our micro capillary device: water and ethylene-glycol at 44% volume concentration. We have used glycerol at this dilution because its density is then practically identical to ethylene-glycol at 44% volume concentration and blood, see Table 4.1). The values of the geometrical parameters of the microchannels were $b = 300\,\mu m$ and $b = 200\,\mu m$.

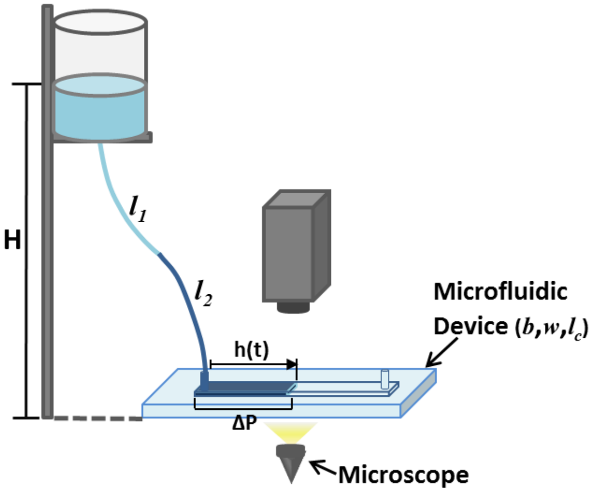

Figure 7.1: *Schematics representation of the experimental setup for the two-fluid system.*

7.1.1 Velocity and Position of the fluid front

Our experiments with the two-fluid system consist of measuring the velocity of advancement of the front of the fluid being pushed, $\dot{h}$, which fills the capillary as a function of its position, h. In Figure 7.2 we show the experimental results for a two-fluid system consisting of ethylene-glycol at 44% pushed by glycerol at 19% compared with the results from the system with one fluid. We observe that, as the front of ethylene-glycol advances through the microchannel pushed by a liquid column of height $H = 420\,mm$, its front velocity suffers a slight increase. By contrast, if the experiment is done with one fluid (ethylene-glycol at 44%), we do not observe such an acceleration. Rather, consistent with our results in Chapter 6, its front velocity remains constant as it fills the capillary. The increase of the velocity of the front of ethylene-glycol at 44% inside the microchannel is of a 12% from the first position measured, $h = 10\,mm$ to the last position measured $h = 30\,mm$.

This result has non-trivial implications in the way we measure the viscosity of the fluid which fills the capillary. In Chapter 5, we describe a method for measuring the viscosity with a single fluid, based on the fact that the advancement of the front occurs at constant velocity. Since this is no longer true for the two-fluid system, we must develop an alternative method.

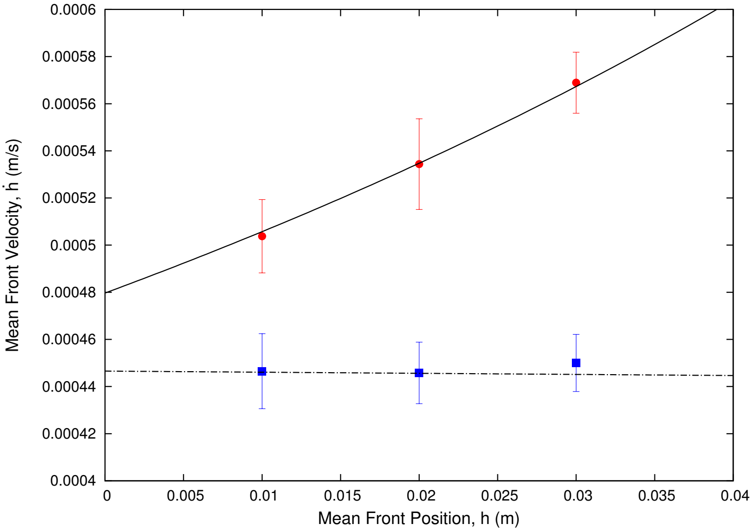

Figure 7.2: *Experimental results showing the increase of the mean front velocity observed in a two-fluid system as the front advances through the microchannel of* $b = 300\,\mu m$. *We are considering a two-fluid system composed by ethylene-glycol at 44% pushed by glycerol at 19% (red circles). The increase in the velocity of the front from the first to the last point measured is of a 12%. We compare this behavior to that of a single fluid system consisting of ethylene-glycol at 44%, where no such acceleration is observed (blue squares). Solid and dashed lines are our theoretical results obtained by using Eq. (7.4) for the two-fluid system (with* $\eta_1 < \eta_2$*) and the single-fluid system (*$\eta_1 = \eta_2$*), respectively. If we consider the theoretical value of the two-fluids system curve the total increase from* $h = 1\,mm$ *to* $h = 40\,mm$ *is 25% for ethylene-glycol at 44%.*

7.2 Comparison with a theoretical modelling

The theoretical modelling presented in this section has been carried out by Enric Costa [Costa Miracle, 2014]. Here we consider a time t_0 when the fluid interface is at the beginning of the microchannel in a position h_0. Then after a time t the position of the front is $h(t)$. Assuming Darcy's law with a permeability of a microrectangular cell, $k = \frac{b^2}{12}$, we write the velocity of the fluid front inside the microchannel as:

$$\dot{h}(t) = \frac{b^2}{12\eta_2} \frac{\Delta P(t)}{h(t)} \tag{7.1}$$

Here in difference with Chapter 5, $\Delta P(t)$, which is the total pressure drop depends on time and has three contributions. Again, the hydrostatic pressure generated by the column of liquid, $P_{hyd} = \rho g H$ which is unaltered since the density of the fluids is similar, the pressure drop generated by the resistance of the tube connecting the fluid container to the microchannel, $\Delta P_R(t)$, which is now time-dependent, due to the presence of a second fluid of known viscosity, η_1, which progressively fills the tube, and, last, the capillary pressure, P_L. Since both the container and the end of the microchannel are open and exposed to the atmosphere, the atmospheric pressure does not play any role. As in the previous case, other contributions to the pressure drop are assumed to be negligible.

To estimate $\Delta P_R(t)$, we assume that the tube connecting the container and the microchannel has a circular cross-section and that the flow inside the tube obeys Poiseuille's law, and therefore

$$\Delta P_R = \frac{8v_t(\eta_1 l_1(t) + \eta_2 l_2(t))}{r^2} \tag{7.2}$$

where η is the viscosity of the fluid, l_t is the length of the tube length, r is the radius of the tube, and v_t is the average flow velocity in the tube. Under these assumptions the total driving pressure inside the microchannel is:

$$\Delta P = \rho g H - \frac{8v_t(\eta_1 l_1(t) + \eta_2 l_2(t))}{r^2} - P_L \tag{7.3}$$

Taking into account that, due to mass conservation, $\dot{h}bw = v_t \pi r^2$, we can write the following equation for the velocity of the front inside the microchannel:

$$\dot{h}(t) = \frac{\rho g H - p_L}{\left(\frac{12\eta_2}{b^2} + \frac{8b^2w^2}{\pi^2 r^6}\left(\eta_1 - \eta_2\right)\right) h(t) + \eta_2 \frac{8bwl_t}{\pi r^4}} \tag{7.4}$$

Equation (7.4) provides a qualitative explanation for the behavior observed in the experiments reported in Figure 7.2. If the two-fluid system is such that the fluid that fills the capillary is more viscous than the one which pushes it into the microchannel (i.e. $\eta_1 < \eta_2$), then Eq. (7.4), for a fixed value of H, implies that, $\dot{h}$ is an increasing function of h (in other words, $\dot{h}$ is an increasing function of time). In the particular case of a one-fluid system, i.e. $\eta_1 = \eta_2$, we recover the situation described in Chapter 5, namely, since $\dfrac{12h(t)}{b^2} \ll \dfrac{8bwl_t}{\pi r^4}$ we have that $\dot{h}$ =constant.

7.2.1 Viscosity measurements in the two-fluid system

We now describe a procedure to measure the viscosity of the fluid that fills the capillary, based on the experimental determination of the velocity and position of its front within the microchannel. We start by defining the quantity, $h_r(t)$, according to:

$$h_r(t) \equiv Ch(t) + D \tag{7.5}$$

where C is given by:

$$C = 1 + \frac{1}{E}\left(\frac{\eta_1}{\eta_2} - 1\right), \tag{7.6}$$

$E = 3\pi^2 r^6/2b^4w^2$ and $D = 2b^3wl_t/3\pi r^4$. Using the definition $h_r(t)$ and Eq. (5.16), we obtain the following relation:

$$h_r(t)\dot{h}(t) = \rho g H - p_L = a > 0 \tag{7.7}$$

where a is a positive constant. Using the fact that $h_r\dot{h} \equiv a$ takes a constant value over the length of the capillary, we can derive the value of the unknown viscosity η_2 by measuring the front velocity at two different points of the microchannel. Consider two positions on the microchannel, h_1 and h_2, and the associated (experimentally determined) velocities, $\dot{h}_1$ and $\dot{h}_2$. Then $h_r(h_1)\dot{h}_1 = h_r(h_2)\dot{h}_2$, which, by means of the definition of h_r (Eq. (7.5)), we have that:

$$C = \frac{D(\dot{h}_1 - \dot{h}_2)}{h_1\dot{h}_1 - h_2\dot{h}_2} \tag{7.8}$$

From Eqs. (7.6) and (7.8), we can explicitly calculate the value of η_2:

$$\eta_2 = \frac{\eta_1}{1 + E\left(\frac{D(\dot{h}_1 - \dot{h}_2)}{h_1\dot{h}_1 - h_2\dot{h}_2} - 1\right)}. \tag{7.9}$$

Equation (7.9) provides the value of the unknown viscosity η_2 in terms of the (known) viscosity of the pushing fluid, the geometric characteristics of the experimental setup and experimental measurements of $\dot{h}$ at two different positions along the capillary.

For this method of measuring the unknown viscosity of the capillary-filling liquid to be consistent, the viscosity η_2 should be independent of both the height of the liquid column, H, and the height of the capillary, b. To check that our method satisfies these consistency criteria, we have performed measurements for different values of H and b. In order to proceed further, we first fix b and we study the behavior of η_2 as H varies. Figure 7.3 shows the results for the viscosity of water and ethylene-glycol for different values of H. We further compare the viscosities obtained from the two-fluid model, Eq. (7.9), with the estimation obtained at Chapter 5 for water and in Chapter 6 for ethylene-glycol at a 40% volume concentration. We observe that, as expected, η_2 is independent of the height of the liquid column, H. We also observe an excellent agreement between the estimates of η_2 associated to our two-fluid method and those of Chapter 5.

We also studied the behavior of the viscosity η_2 as b varies. We change the height of the microchannel to $b = 200\,\mu m$, just as we did with the one fluid system and we obtained the viscosities of the fluids using Eq. (7.9). The viscosity values obtained for both channel heights are shown in Table 7.1.

Fluid	$b = 300\,\mu m$	$b = 200\,\mu m$
Water + Gl.30%	0.98 ± 0.03	1.02 ± 0.04
Etgl.40% + Gl.20%	2.9 ± 0.1	3.0 ± 0.2

Table 7.1: *Viscosities of water and ethylene-glycol 40% using the two-fluids system for 2 different microchannel gaps. Slight variations between both sets of values are due to small temperature variations from* 19 *to* $22°C$

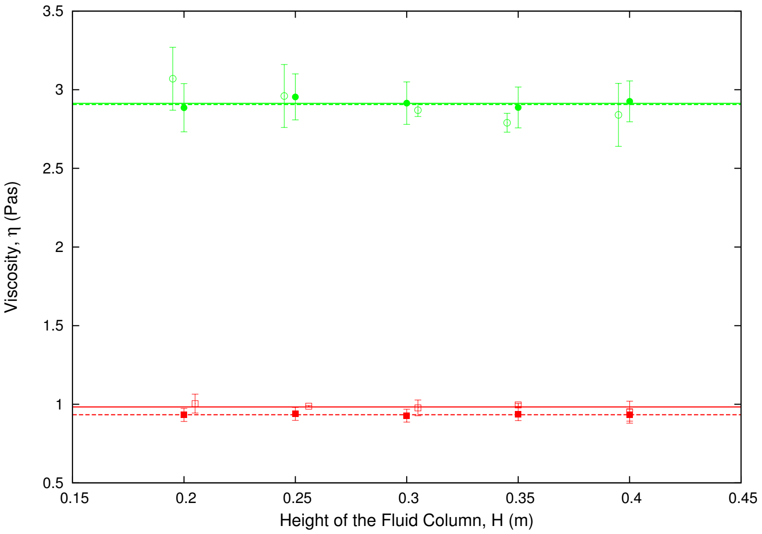

Figure 7.3: *Experimental results for a capillary height* $b = 300\,\mu m$ *showing that the value of the viscosity according to our methodology is independent of the height of the liquid column,* H*. We are considering two-fluid systems composed by water pushed by glycerol at 30% and ethylene-glycol at 40% pushed by glycerol at 19%. We compare this behavior to that of the associated one-fluid system (water and ethylene-glycol at 40%). Solid and dashed lines are our theoretical results obtained by using Eq.(7.9) for the two-fluid system* ($\eta_1 < \eta_2$) *and the one-fluid system* ($\eta_1 = \eta_2$)*, respectively. The values of the viscosities of water and ethylene-glycol measured using the different setups (i.e. one- and two-fluids) are given in Table 7.1. Solid symbols correspond to results obtained with the one fluid system. Empty symbols are associated to measures obtained with the two-fluid setup.*

7.3 Conclusions

We have presented an experimental and theoretical methodology that allows us to determine the viscosity of a fluid in a systems of two immiscible liquids by analysing the propagation of the front within a microchannel. This methodology has the advantage of allowing for the use of very small samples of potentially expensive or rare liquids, as we do not need to fill the container with such liquid. By using our device and methodology, and the associated theoretical model, we have been able to explore a non-Washburn regime in which the fluid front within the capillary accelerates or decelerates depending on the viscosity contrast between both liquids: if the fluid that fills the capillary is more viscous than the liquid that pushes it into the capillary, then the front accelerates, and viceversa. Under these conditions we can not use the methodology proposed in section 5.3 from Chapter 5 to measure viscosities of Newtonian fluids, so we have developed a new method. This new method is based on, for a fixed height of the liquid column, measuring the front velocity at two different positions within the microchannel. We have checked that the viscosity obtained does not exhibit spurious dependencies on experimental factors such as the height of the liquid column, H, or the value of the capillary gap, b. Using this method, we obtain results consistent with those reported in the literature. The flow regime studied in this chapter, in which we can observe both acceleration and deceleration of the fluid front, may induce to misinterpret the data regarding the properties of the fluid flow regime being observed. The theoretical approach that we have presented in this chapter allows us to reliably measure the viscosity of Newtonian fluids regardless of the fluid regime introduced by our experimental setup. This theoretical framework is the stepping stone towards studying more complex fluids such as blood and other non-Newtonian fluids, as it allows to separate spurious dependencies produced by experimental artifacts from genuine non-Newtonian effects.

PART IV

Non Linear Rheology

Blood Experiment

The objective of this thesis has always been the study of the blood-air interface moving inside a microchannel, and thus, understand blood rheological properties. In order to achieve this, we had first analized Newtonian fluids and its behavior inside the microchannels, which has been done in Part III of this thesis. Now that we have defined and understand the behavior of Newtonian fluid with our device and method, it is time to move forward to the study of blood.

From a rheological point of view, blood has many interesting features. Related to its viscosity it is known that it presents shear thinning [Cokelet et al., 1963; Merrill, 1969; Thurston, 1972] and yield stress [Picart et al., 1998]. These hemorheological properties have many causes... the formation of red blood cells aggregates and their deformation properties cause the viscosity of blood to increase and to be very dependent on the shear rate [Lowe et al., 1988], promoting its characteristic shear thinning behavior given that as the shear rate increases shear forces disperse the rouleaux, decreasing its general viscosity value.

In this chapter I will present in the first section blood protocols, sample preparation and explain the measure methods and its particular changes due to blood compared with Newtonian fluids. In the next section, section 8.2, I will present previous results for blood behavior inside the microchannel without imposing any particular model.

8.1 Sample Preparation

A healthy adult blood sample has an hematocrit that varies from 35% - 48%, although this values may vary whether the donor is female or male. We have performed experiment for several samples of blood using different red blood cells concentrations, fresh and old samples and healthy and ill blood. We have been able to obtain its viscosities using diverse non-Newtonian viscosity models and depicted its non-Newtonian shear thinning behavior.

Blood samples are delivered for our experiments from the Hematology Department of Hospital Clinic Barcelona in tubes of 10 or $5\,ml$ on an heparine based anticoagulant. In order to preserve the state of the samples, they are stored on a refrigerator at $4°C$. In general a blood sample is used in one or two days. If the sample gets older its composition changes and the results may be altered due to the formation of aggregates, the emergence of echynocytes or the rupture of cells which may decreased the effective value of the hematocrit.

Before any intervention on the sample, it is set under a chemical fume hood to avoid contamination and to acquire room temperature, between 20 to $25^\circ C$. When the sample reaches room temperature, it is carefully mixed to separate aggregated cell and mixed them with blood plasma. To separate aggregated red blood cells we tap the tube smoothly and then we mix with blood plasma using a pipette to accomplish an homogeneous mixture.

If we required to separate the sample in different hematocrit concentrations we centrifuge the sample to separate the plasma from the cellular fraction. The blood sample in the tube is set on a centrifuge and spun for 5 minutes at $2500\,rpm$. When the spinning has finished, the cellular fraction (RBC's, WBC's and platelets) is confined at the bottom of the tube and the plasma on the top. Under the extraction hood, to avoid contamination of the sample, the plasma is extracted using a pipette and separated equitably in different sterilized eppendorf tubes, figure 8.1. The number of separations would depend on the total amount of plasma and the number of different sample that we want to attain. Once all the sample are separated by different hematocrit, they are carefully mixed to get an homogeneous sample.

By means of a $1\,ml$ syringe, a small amount of the homogeneous mixture, $V \approx 600\,\mu l$, is introduced inside the tube that communicates a fluid recipient with the microchannel, until it is completely filled with the sample. To avoid the effects of RBC's sedimentation inside the recipient, the container is filled with glycerol diluted in distilled water, where the resultant dilution has the approximate density of the blood sample. The values of the concentration of glycerol that correspond to the density of the blood sample are shown in table 8.1. A representation of the setup is show in figure 8.2.

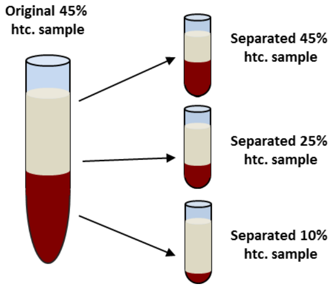

Figure 8.1: *Schematic of the blood sample separation in different hematocrit % samples.*

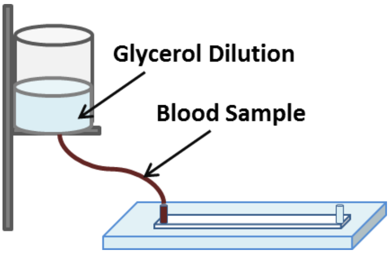

Figure 8.2: *Schematic of the blood setup.*

Rheological measurements of whole blood at high shear rates is relatively simple as it behaves as an homogeneous and Newtonian fluid. However, at low shear rate, sedimentation and formation of clear plasma phase may easily ruin the intended measure or give misleading results, see figure 8.3. In capillary rheometry this effects may be attenuated through carefully mixing the sample and a clear and speeded execution of the experiments. The sedimentation inside the micro-channel may alter significantly the measures, this is why blood it is not allowed to stand in the capillary for more than a few second considering that sedimentation rates of healthy blood is $\approx 1\mu m/s$. To

RBCs concentration	Density, ρ $\left(\frac{kg}{m^3}\right)$	Glycerol concentration
45%	1050	19%
20%	1035	14%
Blood Plasma	1025	10%

Table 8.1: *The table shows the concentration of glycerol for each value of the concentration of blood to obtain an equivalent density. All the values are taken at a temperature of* $20°C$.

avoid sedimentation effects in our measures at low shear rates we have perform the velocity measures of blood at $3\,mm$ from the beginning of the channel. Although, some measures were taken at 3 different positions in the channel: 10, 20 and $30\,mm$ from the micro-channel inlet. This was made to observe how the sample evolved along the channel.

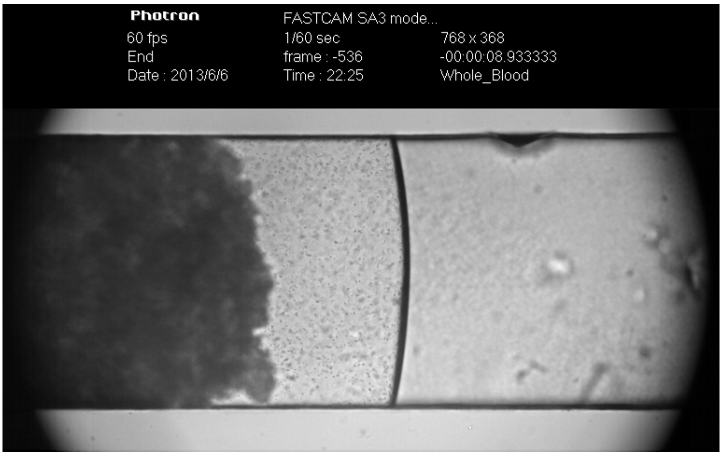

Figure 8.3: *The figure shows a live image of the sedimentation effects inside the channel. To achieve low shear rates, the injected pressure must be low, thus the velocity of the blood-air interface is slow. This causes the sample to stay inside the channel for too long allowing red blood cells to sediment and a separation of faces is observe.*

8.2 Blood in the micro-channel

The experiments were performed for blood at different red blood cells concentrations taken from different subjects (donors). The experiments have been performed with samples of 48%, 42% and 38% of hematocrit. The 38% sample has been separated in 30%, 20% and 10% samples. The 48% sample was also separated in a 25% hematocrit sample. Blood plasma corresponding to each sample was also measured alone to set a based viscosity value of the sample.

Just as it was made for water and other fluids it is important to understand how blood behaves along the channel to appreciate if the sedimentation effects or the two fluids setup affects the velocity response of the blood sample.

The velocity profile obtain for blood is shown in figure 8.4 for a 48% hematocrit sample. The velocity profile is measured for different heights of the fluid column throughout a $\approx 5\,mm$ trail starting at $h_0 = 3\,mm$ from the channel inlet. This way we avoid red blood cells sedimentation inside the channel and the acceleration effects due to the glycerol solution at the beginning of the tube. The mean velocity for the blood front, $\dot{h}$, is obtained averaging the velocity profile values.

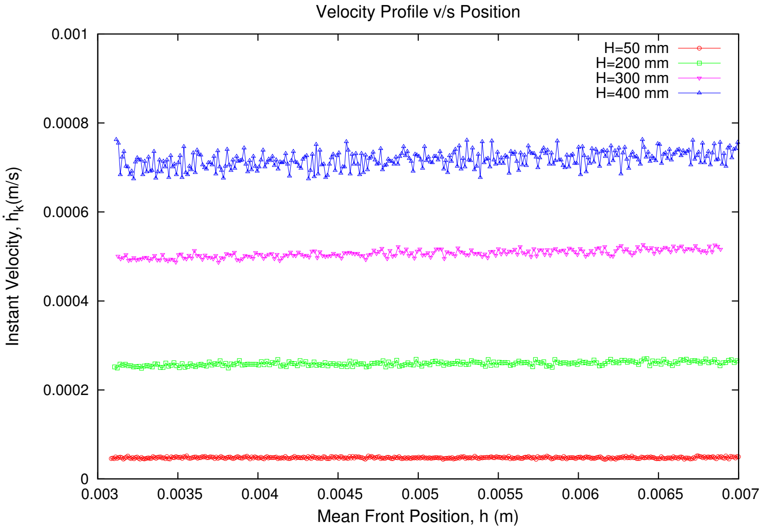

Figure 8.4: *Velocity profile for blood at a 48% of hematocrit for different heights of the fluid column measured at $h_0 = 3\,mm$ from the channel inlet. We observe a slight acceleration at high heights but it is inside the mean velocity error so it is neglected.*

Even though a slight acceleration is observe along the trail, is it not significant compared with the one obtained for other fluids, see chapter 7. Besides, the mean velocity values at this position of the channel is kept inside the velocity profile dispersion which makes this effect negligible for a position at the beginning of the channel and for short travelled distances, Δh. To state this last point we measured the velocity of blood at three point inside two channels of different gap. The measures were taken $1\,cm$ apart, in figures 8.5a and 8.5b these results were overlapped with the velocity function for a two viscosities system equation (7.4). Comparing both figures, we observe that in the higher microchannel the effect of a second fluid is more relevant than in the channel with smaller gap. This may drawn us to chose the channel with smaller gap to avoid misleading effects, but if we seek low shear rates ranges to calculate the viscosity of blood it is recommendable to use microchannels with high gaps, but in this case we need to carefully avoid the effect of the two fluids system. In order to achieved a reliable value of the velocity, the function for a channel of $b = 300\,\mu m$ is extrapolated to closer positions from the inlet, we obtained that the difference in velocity at $h = 3\,mm$

is 1% and until the front reaches $h = 8\,mm$ the increased in velocity does not overcomes a 5% and we may consider it negligible.

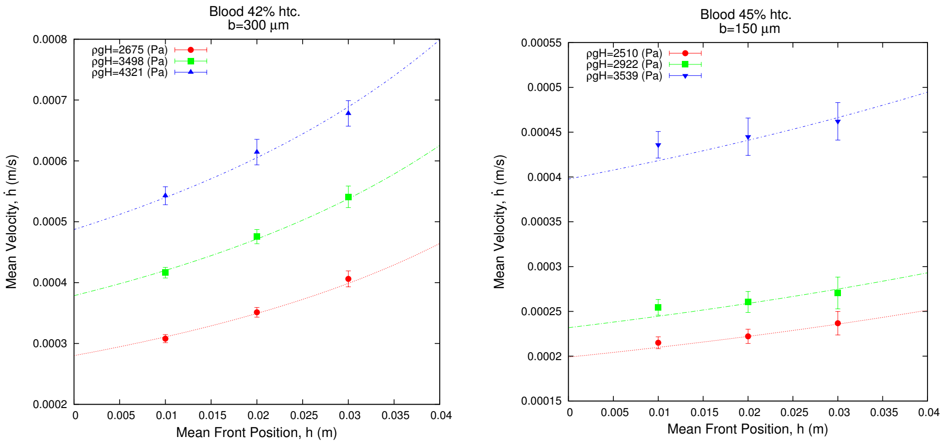
(a) (b)

Figure 8.5: *The figure shows the velocity of a two blood samples at different positions of a channel. The mean velocity is calculated over $\Delta h \approx 2\,mm$. The dotted lines correspond to the velocity functions using a two fluids setup, eq. (7.4) from chapter 7. Figure (a) shows the velocity of a 42% htc. sample in a microchannel of $b = 300\,\mu m$, for 3 different injected pressures. Figure (b) shows the velocity of a 45% htc. sample in a microchannel of $b = 150\,\mu m$. Comparing both figures, it is clearly appreciated that at a microchannel with higher gap, b, the effects of a second fluid becomes more relevant.*

It is widely know that the viscosity of blood is highly dependent on the hematocrit concentration, as the cellular fraction increases the viscosity also does [Pries et al., 1992]. This must be a key feature of a viscometer intended for blood. Figure 8.6 shows this effect of the hematocrit for the separated 38% sample as function of the blood interface velocity. Here we can observed, as expected, that the velocity of the blood sample is very dependent on the RBC concentration decreasing to almost half the value from the blood plasma alone to the 38% htc sample. It can be seen that this effect is also repeated at different injected pressures and in each case this effect does not follows a linear relation. With this result one of the basics features of the rheological aspect of blood is described by our device and method.

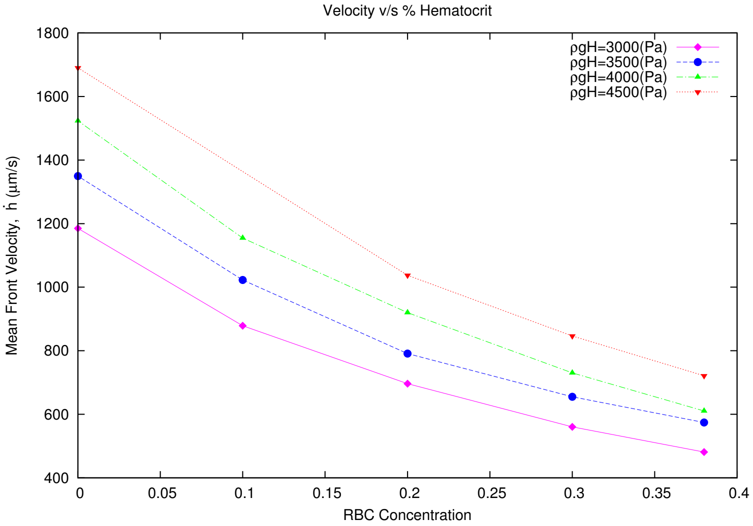

Figure 8.6: *The figure shows the velocity respond of the blood sample against the RBC concentration, for 4 different injected pressures. The measures were taken at* $20\,mm$ *from the inlet of the channel. This measures were performed using an original sample of 38% of hematocrit separated in 30%, 20% and 10% hematocrit and blood plasma (0 RBC Concentration).*

Now that we have selected a position to measure the velocity of the blood sample, in order that the acceleration due to the glycerol dilution does not affect the captured velocity of the front, we proceed to measure the velocity response of the blood front to different exerted hydrostatic pressures. This raw results of the measure are shown in Figure 8.7 and 8.8 for two different blood sample compared with its correspondent blood plasma.

We can see that in both cases, at high hematocrit 38% and 48% respectively, the relation between the pressure exerted and the velocity has a different value of the slope n, compared to the ones obtained for plasma, which is Newtonian with $n = 1$. Thus, we can infer that the behavior of the blood samples at higher hematocrit is non-Newtonian. In the next chapter we will present different non-Newtonian models to estimate the viscosity of these blood samples and understand its non-Newtonian behavior.

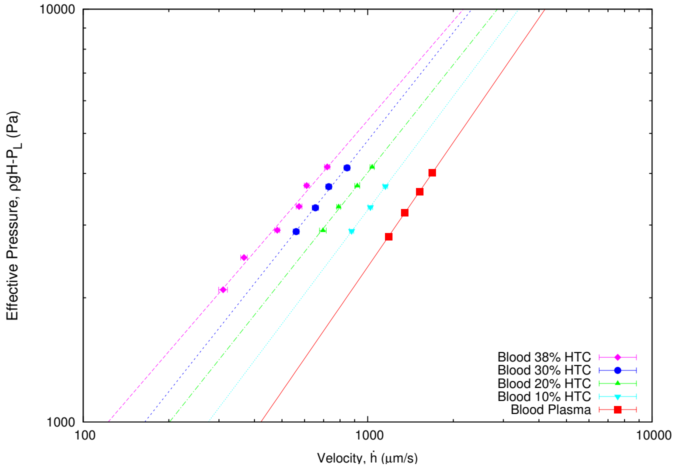

Figure 8.7: *The figure shows the relation between the Effective Pressure and the Mean Front Velocity of a blood sample at 4 different hematocrit concentrations and blood plasma. Blood at 38% (magenta)* $n = 0.80$*, Blood at 30% (blue)* $n = 0.87$*, Blood at 20% (green)* $n = 0.87$*, Blood at 10% (cyan)* $n = 0.92$ *and Blood Plasma (red)* $n = 1.001$

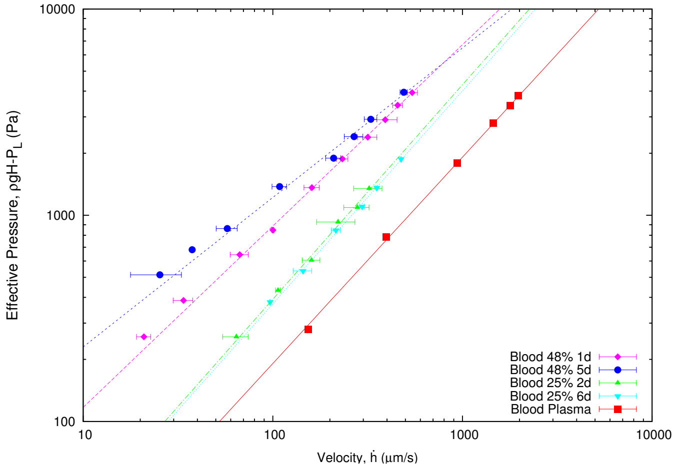

Figure 8.8: *The figure shows the relation between the Effective Pressure and the Mean Front Velocity of a blood sample at 2 different hematocrit concentrations but different ages (days old from extraction) and blood plasma. Blood at 48% 1 day old (magenta)* $n = 0.88$*, Blood at 48% 5 days old (blue)* $n = 0.74$*, Blood at 25% 2 days old (green)* $n = 1.04$*, Blood at 25% 6 days old (cyan)* $n = 1.03$ *and Blood Plasma (red)* $n = 1.00$

Blood Viscosity

Through the years several models have been developed in order to attain a proper approximation to non-Newtonian fluids viscosity. In the particular case of blood models as the Power Law Model and the Carreau are the most used [Larson, 1999; Morrison, 2001]. The aim of this thesis has always been, to obtain a reliable values of the viscosity of blood by mean of a device and setup designed to accomplish this objective.

A whole blood sample of 38% RBC's concentration was decomposed in lower hematocrit concentrations: 30%, 20% and 10%. The blood plasma of this sample was also separated and measured. To simplified this measures we only made them at high injected pressures, meaning high shear rates, and the values of the Laplace pressure was obtained through the measure of the front curvature. Another sample of 48% of hematocrit was, as well, decomposed in lower hematocrit of 25% but we perform the measures at different days from the extraction of the sample. This way we have a 48% hematocrit fresh sample of 1 day old and a 5 days old sample and a 25% hematocrit samples of 2 days and 6 days old[1].

In this chapter I will first described some typical models to measure blood viscosity and compare them with our results. Later I will review this results using the correction for non-Newtonian viscosity obtained by means of capillary rheometry. Finally I will present a new model which describes blood as segmented regimes of behaviors.

9.1 Power Law Model for non-Newtonian fluids applied to Blood

The simplest model developed for non-linear viscosities is the Ostwald-de Waelle Model also known as Power Law. This model relates the stress at which the fluid is submitted with the shear rate at which it responds, through a viscosity that depends on shear rate:

$$\eta(\dot{\gamma}) = m\dot{\gamma}^{n-1} \tag{9.1}$$

As shown in equation (9.1), the viscosity of the fluid depends on the shear rate and an viscosity exponent $n - 1$. When $n = 1$ we recover the linear relation that characterizes Newtonian fluids as previously shown in chapters 5 and 6. If the value of the exponent is $n < 1$ we observe Shear Thinning behavior and when $n > 1$ we

---

[1] The older samples were stored on a refrigerator at 4^{o}C

observe Shear Thickening. The quantity m represents a constant base viscosity which in the case of Newtonian fluids corresponds to the viscosity of the fluid.

From the solution to the Stokes equation with a shear rate-dependent viscosity and considering the coupled system tube-microchannel [Costa Miracle, 2014] a relation between the velocity and the pressure is defined in equation (9.2). The value of the variable P_L is obtained according to the calculation of the capillary pressure inside the microchannel using the curvature of the blood interface and $A(n)$ is a geometrical parameter defined in equation (9.3), see chapter 2.

$$\rho g H - P_L = A(n)\dot{h}^n \tag{9.2}$$

$$A(n) = m \cdot \frac{2l_t\left(\frac{1}{n}+3\right)^n}{r^{n+1}}\left(\frac{bw}{\pi r^2}\right)^n \tag{9.3}$$

The value of the parameter n is taken from the relation between the effective pressure, $(\rho g H - P_L)$, against the velocity, $\dot{h}$, of the fluid inside the channel. Fitting our experimental results to equation (9.2) as shown in figures 9.1 and 9.2 we obtain the values for n and $m \cdot A(n)$ which are used to calculate the viscosity of the blood sample.

In both cases (both samples) we fit a Power Law to the data of the relation between pressure and velocity inside the channel we can obtain an approximate value for high shear rate of the viscosity exponent $n \neq 1$ which establish that the behavior is not longer Newtonian for the blood sample and it different hematocrit concentrations. Figure 9.1 shows this behavior for the different hematocrit concentrations and blood plasma and figure 9.2.

The shear rate is defined as function of the velocity of the interface, $\dot{h}$, and the micro-channel gap, b, for a rectangular micro-channel as shown in equation (9.4). Combining this definition with equation (9.3) the relation between the effective pressure and the velocity of the blood-air interface can be re-written as a function of the shear rate as equation (9.5). Finally the prefactor m from the viscosity definition (eq. 9.1) is calculated by mean of the values for $A(n)$ and n obtained from the power law fit to the data shown in Figures 9.1 and 9.2.

$$\dot{\gamma} = \frac{\dot{h}}{b} \tag{9.4}$$

$$\rho g H - P_L = m\frac{2lt\left(\frac{1}{n}+3\right)^n}{r^{n+1}}\left(\frac{b^2 w}{\pi r^2}\right)^n \dot{\gamma}^n \tag{9.5}$$

$$m = \frac{A(n)}{\frac{2lt\left(\frac{1}{n}+3\right)^n}{r^{n+1}}\left(\frac{b^2 w}{\pi r^2}\right)^n} \tag{9.6}$$

With no more unknown variables we can now calculate the viscosity, η, as a function of $\dot{\gamma}$ of the blood samples. The viscosity values associated to this model are shown in table 9.1 and represented in figures 9.3 and 9.4.

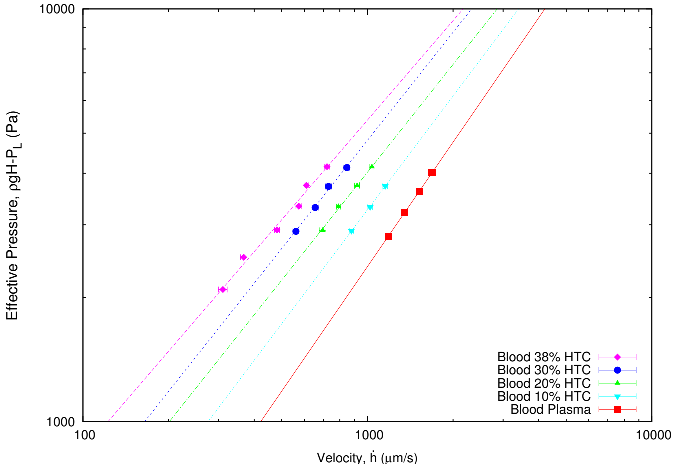

Figure 9.1: *The figure shows the relation between the Effective Pressure and the Mean Front Velocity of a blood sample at 4 different hematocrit concentrations and blood plasma. Blood at 38% (magenta)* $n = 0.80$*, Blood at 30% (blue)* $n = 0.87$*, Blood at 20% (green)* $n = 0.87$*, Blood at 10% (cyan)* $n = 0.92$ *and Blood Plasma (red)* $n = 1.001$

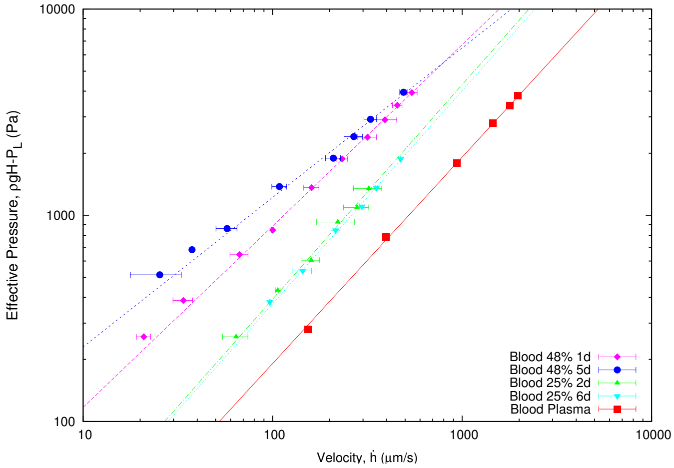

Figure 9.2: *The figure shows the relation between the Effective Pressure and the Mean Front Velocity of a blood sample at 2 different hematocrit concentrations but different ages (days old from extraction) and blood plasma. Blood at 48% 1 day old (magenta)* $n = 0.88$*, Blood at 48% 5 days old (blue)* $n = 0.74$*, Blood at 25% 2 days old (green)* $n = 1.04$*, Blood at 25% 6 days old (cyan)* $n = 1.03$ *and Blood Plasma (red)* $n = 1.00$

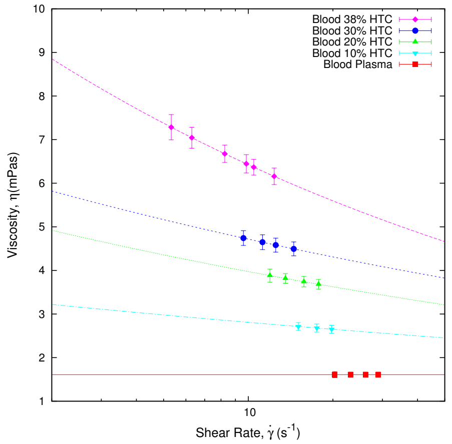

Figure 9.3: *Viscosity as a function of shear rate for Blood at 4 different hematocrit and Blood Plasma. Blood at 38% (magenta), Blood at 30% (blue), Blood at 20% (green), Blood at 10% (cyan) and Blood Plasma (red).*

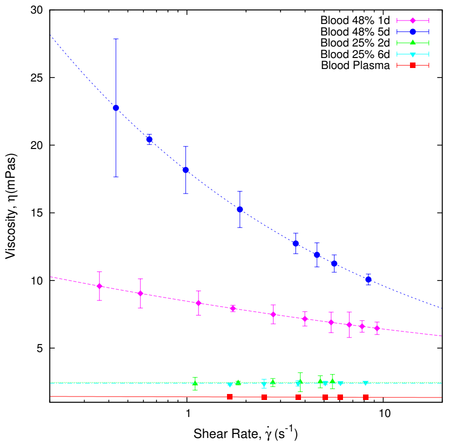

Figure 9.4: *Viscosity of Blood at two different hematocrit and Blood Plasma at different times since extraction. Blood at 48% (magenta) fresh sample (1 day), Blood at 48% (blue) old sample (6 days), Blood at 25% (green) 2 days, blood at 25% (cyan) 6 days and Blood Plasma (red).*

Hematocrit %	Exponent $(n-1)$	m
38	-0.199	0.010164
30	-0.131	0.006371
20	-0.133	0.005393
10	-0.085	0.003413
BP	0.001	0.001609
48 1d	-0.12725	0.008469
48 5d	-0.2751	0.01809
25 2d	0.040	0.00246
25 6d	0.032	0.00240
BP	0.004	0.001404

Table 9.1: *The table shows the values of the viscosity exponent n and the prefactor m obtained using the Power Law Model for Blood at different hematocrit concentrations and different ages. Using this parameters in eq. (9.1) we may calculate the viscosity values of the sample at a given shear rate.*

9.2 Weissenberg-Rabinowitsch Correction

According to the Weissenberg-Rabinowitsch-Mooney equation for non-Newtonian fluids in a capillary rheometer (chapter 2, section **??**) we have defined a “true” shear rate, equation (9.7), as a function of a wall stress and a wall shear rate

$$\dot{\gamma}_t = \frac{1}{4}\dot{\gamma}_w \left[3 + \frac{d\,lnQ}{d\,ln\sigma_w} \right] \tag{9.7}$$

Due to our setup the wall shear rate at the tube, $\dot{\gamma}_w$, is define as a function of the flow rate of the fluid moving inside the microchannel, equation (9.8). The flow rate of the fluid is obtained from the velocity, $\dot{h}$, of the interface inside the channel through $Q = \dot{h} \times A = \dot{h}wb$, where w is the width and b the depth of the microchannel.

$$\dot{\gamma}_w = \frac{4Q}{\pi r^3} \tag{9.8}$$

Using the expression in equation (9.7) we define a viscosity for the non-Newtonian fluid as:

$$\eta = \frac{\sigma_w}{\dot{\gamma}_t} \tag{9.9}$$

In the particular case of our setup the quantity σ_w, is the shear stress in the tube due to the pressure drop and it is defined in equation (9.10), where $r = 127\,(\mu m)$ is the tube radius and $l_t = 0.43\,(m)$ is the tube length. The value of the variable P_L is obtained according to the calculation of the capillary pressure inside the microchannel using the curvature of the blood interface.

$$\sigma_w = \frac{r}{2}\frac{\rho g H - P_L}{l_t} \tag{9.10}$$

Considering the definitions in equations (9.7) and (9.10) we may rewrite an expression for the viscosity as a function of the geometrical parameters of the tube and the channel and the measured flow rate inside the channel.

$$\eta = \frac{\pi r^4}{2 l_t Q} \frac{\rho g H - P_L}{\left[3 + \frac{d\,lnQ}{d\,ln\sigma_w} \right]} \tag{9.11}$$

9.2.1 Correction for blood hematocrit

In order to obtain the viscosity of the fluid from equation (9.11) we first need to find an expression for the term $\frac{d\,lnQ}{d\,ln\sigma_w}$. Through the fit of our experimental results, figure 9.7, to equation (9.12) and differentiating we obtain the value $B = \frac{d\,lnQ}{d\,ln\sigma_w}$.

$$\ln Q = A + B\,ln\,\sigma_w \tag{9.12}$$

This relation is an analog to a Power Law model for a non-Newtonian fluid, $\eta = m\dot{\gamma}^{n-1}$ where $n = \frac{1}{B}$. We now are able to compared the value of the viscosity exponent n in both approximations, this are shown in table 9.2. Here we see that the value of the

Hematocrit	Power Law		WRM Correction	
%	n	$\pm\delta n$	$n = \frac{1}{B}$	$\pm\delta n$
38	0.80	0.05	0.80	0.07
30	0.87	0.05	0.88	0.06
20	0.87	0.03	0.88	0.04
10	0.91	0.02	0.91	0.03
BP	1.001	0.007	1.002	0.007
48 1d	0.88	0.01	0.84	0.01
48 5d	0.72	0.03	0.67	0.04
25 2d	1.04	0.05	1.02	0.03
25 6d	1.03	0.02	1.01	0.02
BP	1.00	0.01	1.01	0.01

Table 9.2: *Viscosity of Blood at shear rate of* $\dot{\gamma} = 180\,(s^{-1})$ *for different hematocrit of a whole blood decomposed sample of 38% of hematocrit.*

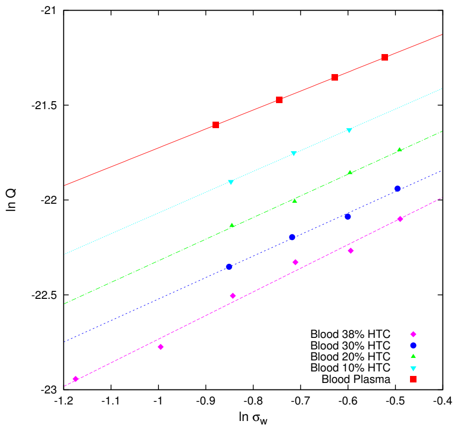

Figure 9.5: *lnQ v/s ln*σ_w *for 4 different hematocrit and blood plasma. Blood at 38% (magenta)* $B = 1.24$*, Blood at 30% (blue)* $B = 1.13$*, Blood at 20% (green)* $B = 1.14$*, Blood at 10% (cyan)* $B = 1.09$ *and Blood Plasma (red)* $B = 0.997$

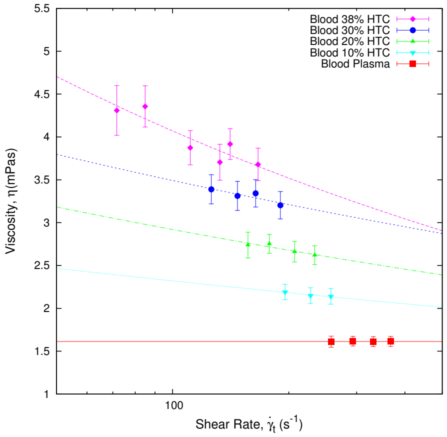

Figure 9.6: *Viscosity v/s Shear rate for Blood at 4 different hematocrit and Blood Plasma. Blood at 38% (magenta), Blood at 30% (blue), Blood at 20% (green), Blood at 10% (cyan) and Blood Plasma (red).*

exponent does not vary significantly with the model and the viscosity values are much alike.

Then, the viscosity expression in equation (9.11) is then reduced to the one shown in equation (9.13) which is used to obtain the viscosities of the blood samples, figure 9.8. Table 9.3 shows the values of the exponents $n - 1$ and viscosities for $\dot{\gamma} =$

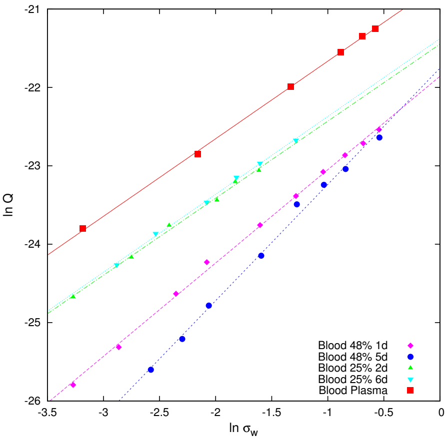

Figure 9.7: *lnQ v/s $ln\sigma_w$ for 4 different hematocrit and blood plasma. Blood at 38% (magenta) $B = 1.24$, Blood at 30% (blue) $B = 1.13$, Blood at 20% (green) $B = 1.14$, Blood at 10% (cyan) $B = 1.09$ and Blood Plasma (red) $B = 0.997$*

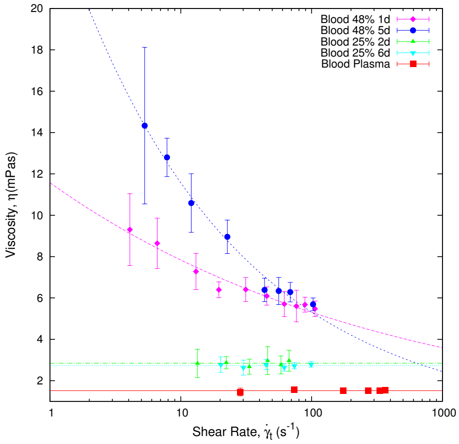

Figure 9.8: *Viscosity v/s Shear rate for Blood at 4 different hematocrit and Blood Plasma. Blood at 38% (magenta), Blood at 30% (blue), Blood at 20% (green), Blood at 10% (cyan) and Blood Plasma (red).*

$180\, s^{-1}$.

$$\eta = \frac{\pi r^4}{2 l_t w b} \frac{\rho g H - P_L}{\dot{h}\left[3 + \frac{1}{n}\right]} \tag{9.13}$$

Hematocrit %	Exponent $(n-1)$	$\eta\,(cP)$ $180\,(s^{-1})$
38	-0.209	3.599
30	-0.121	3.252
20	-0.124	2.720
10	-0.088	2.203
Blood Plasma	0.001	1.614

Table 9.3: *Viscosity of blood at shear rate of $\dot{\gamma} = 180\,(s^{-1})$ for different hematocrit of a whole blood decomposed sample of 38% of hematocrit.*

Hematocrit %	Exponent $(n-1)$	$\eta\,(cP)$ $100\,(s^{-1})$
48 1d	-0.169	5.3 ± 0.4
48 5d	-0.338	5.3 ± 0.7
25 2d	0.014	2.84 ± 0.04
25 6d	0.005	2.72 ± 0.02
Blood Plasma	0.001	1.51 ± 0.01

Table 9.4: *Viscosity of blood at shear rate of* $\dot{\gamma} = 180\,(s^{-1})$ *for different hematocrit of a whole blood decomposed sample of 38% of hematocrit.*

9.3 n-dependent Model for Blood

Power Law Model or a WRM Model are useful in presence of a single value of the viscosity exponent n, but in some particular cases a 2 regimes behavior is spotted in the results and instead of considering the previous models, something new needs to be developed. In the previous section we calculated the viscosity values of a 48% sample at a wide spectre of shear rates (which was not appreciated for the 38% sample). For the 48% sample we may distinguish a regime at low shear rate and a different one at high shear rates. This way, figure 9.2 may be depicted as shown in figure 9.9.

Here the effective pressure, P_{eff}, is defined as $P_{eff} = \rho g H - P_L$. This figure shows results for the behavior of the fluid front for different values of the hematocrit (volume fraction occupied by the RBC's) and for different values of age of the sample (time elapsed since extraction). We observe that whole blood (48% hematocrit) exhibits non-Newtonian behavior regardless of age. Non-Newtonian behavior is here characterized in terms of a non-linear dependence of the front velocity on the effective pressure: $P_{eff} \sim \dot{h}^n$. Our experiments detect two regimes: one at low velocity with $n \simeq 0.70$, where the fluid is non-Newtonian, and another at higher velocity with $n \simeq 1$, where blood behaves as a Newtonian fluid, as observed when comparing the measurements for plasma. By contrast, blood with reduced hematocrit (25%) shows Newtonian behavior in all the range and regardless of age.

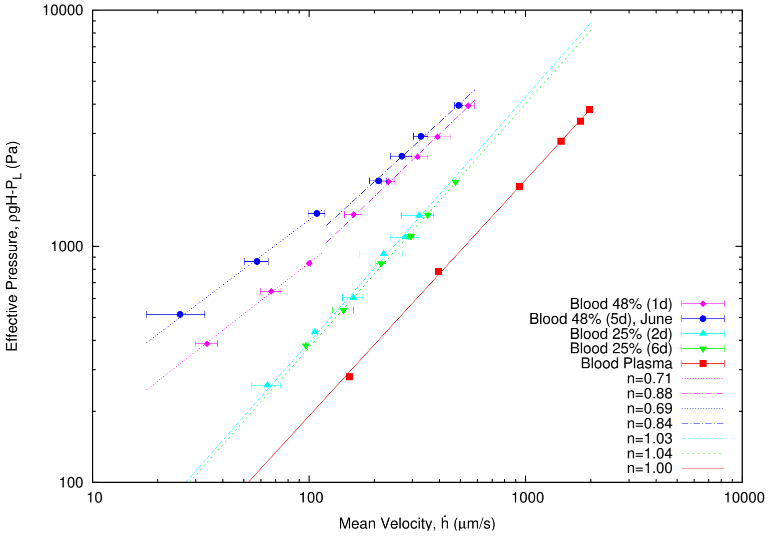

Figure 9.9: *Plot showing the dependence of the pressure on the mean front velocity for blood at different values of hematocrit (48% and 25%) and for different post-extraction times. We observe that, in the case of whole blood (48% hematocrit), two regimes are present: a non-Newtonian regime with* $n \simeq 0.70$ *for small velocity (dotted lines) and a Newtonian regime with* $n \simeq 1$ *(dashed line) for larger velocities. The behavior of blood at 25% hematocrit is observed to be Newtonian in the whole range of measured velocities, regardless of the age of the sample (2 or 6 days). For comparison, we add the results for plasma.*

9.3.1 Model

In proceed further to analyze the properties of blood viscosity, we need to formulate a model which allows us to derive the expression of the viscosity as a function of the setup parameters. In particular, we consider power-law non-Newtonian fluids, i.e.

$$\eta(\dot{\gamma}) = m\dot{\gamma}^{n-1} \tag{9.14}$$

where $\dot{\gamma} = \dfrac{\partial v_x}{\partial z}$ is the shear rate and m and n are constants which depend on the fluid. The Stokes equation associated to such fluid is:

$$\frac{d}{dz}\left(\eta(\dot{\gamma}(z))\dot{\gamma}(z)\right) = \frac{\Delta P}{h(t)} \tag{9.15}$$

where ΔP is the total pressure drop and $h(t)$ is the position of the front. Integrating Eq. (9.15) we obtain that $\dot{\gamma}(z) = \left(\dfrac{\Delta P}{mh(t)}z\right)^{1/n}$. By integrating this expression between $\pm b/2$ with non-slip boundary conditions, we obtain $v_x(z)$ from which we can derive an expression for the flow rate, Q. Moreover, $Q = bw\dot{h}$ where b and w are, respectively, the gap and the width of the capillary, and $\dot{h}$ is the average front velocity. Exploiting the relation between Q and $\dot{h}$, we derive an equation for the dependence of ΔP on $\dot{h}$:

$$\rho g H - \Delta P_t = \frac{2m}{b}\left(\frac{2}{b}\left(2 + \frac{1}{n}\right)\right)^n h\dot{h}^n \tag{9.16}$$

where $\Delta P = \rho g H - \Delta P_t - P_L$ with P_L being the capillary pressure and ΔP_t, the pressure drop across the inlet tube (see Fig. ...). Using the same procedure for the inlet tube in cylindrical coordinates, we obtain an explicit expression for ΔP_t in terms of the average flow velocity within the tube, v_t. Flow conservation across the whole tube-microchannel system, $bw\dot{h} = \pi r^2 v_t$, allows us to couple both fluid systems to obtain a global expression which relates the front velocity with the pressure drop:

$$\dot{h}(t)^n = \frac{(\rho g H - P_L)}{\left[\dfrac{2l_t\left(\frac{1}{n}+3\right)^n}{r^{1+n}}\left(\dfrac{bw}{\pi r^2}\right)^n + \dfrac{h(t)\left(2+\frac{1}{n}\right)^n}{\left(\frac{b}{2}\right)^{1+n}}\right]} \tag{9.17}$$

We assume that for, all t, the second term in the denominator of Eq. (9.17) is much smaller than the first term, i.e. the resistance in the microchannel is much smaller than in the tube. Under these conditions $\dot{h} \simeq$cnt. and we obtain a relation between $\rho g H$ and $\dot{h}$ given by:

$$\rho g H - P_L = m\frac{2l_t\left(\frac{1}{n}+3\right)^n}{r^{1+n}}\left(\frac{bw}{\pi r^2}\right)^n \dot{h}^n \tag{9.18}$$

We can now define a rescaled pressure, σ, by means of the following relation with the viscosity: $\sigma = \eta(\dot{\gamma}_F)\dot{\gamma}_F = m\dot{\gamma}_F^n$, where $\dot{\gamma}_F$ is the shear rate associated to the advancement of the front. By comparing this expression with Eq. (9.18), we derive explicit definitions of both σ and $\dot{\gamma}_F$:

$$\sigma = \frac{r}{2l_t}(\rho g H - P_L),$$
$$\dot{\gamma}_F = \frac{b^2 w}{\pi r^3}\left(3 + \frac{1}{n}\right)\left(\frac{\dot{h}}{b}\right) \tag{9.19}$$

In Fig. 9.10 we show how the blood viscosity varies as the shear rate, $\dot{\gamma}_F$, changes. These results are associated to the ones shown in Fig. 9.9. We observe that our experimental results fit within our power-law Ansatz Eq. (9.14).

Hematocrit	Exponent 1 $(n-1)$	Prefactor m
48% 1d NN	-0.29	0.01190
48% 5d NN	-0.31	0.02030
48% 1d N	-0.12	0.00830
48% 5d N	-0.16	0.01096
25% 2d	-0.004	0.00265
25% 6d	-0.01	0.00256
plasma	0	0.00152

Table 9.5: *Viscosity parameters from Eq. (9.14) for different blood sample hematocrit and ages. The term "NN" denotes the parameters for the Non-Newtonian regimes while "N" is meant for the Newtonian regimes.*

9.4 Conclusion

We have estimated the viscosity of different blood samples using three different models and each model has delivered a non-Newtonian behavior of the blood samples. The viscosity values obtained are consistent with literature at the estimated shear rates, see Appendix C.

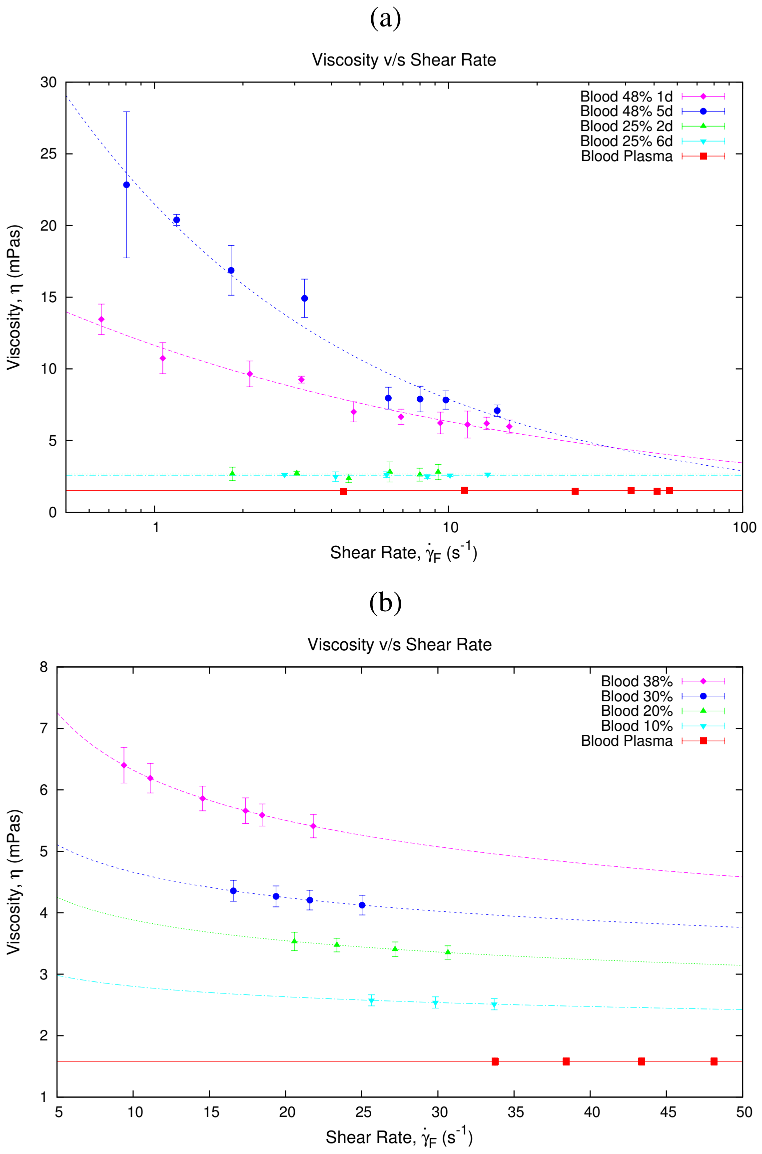

Figure 9.10: *Plots showing how the viscosity of blood varies as the shear rate, $\dot{\gamma}_F$, increases. These results are associated to the experiments shown in Fig. 9.9. They have been obtained using eqs. (9.14) and (9.19). Fig.* ***(a)*** *shows the viscosity obtained for the 48% htc sample. Fig.* ***(b)*** *shows the viscosity values obtained for a sample at different hematocrit concentrations. Even though, in this last case we do not have two regimes, we used the n-dependent method in order to compared the viscosity values obtained using the previous method.*

Viscosity Scaling

10.1 Aggregation Scaling by Aging

Red blood cells aggregation is the major determinant of the in vitro rheological properties of blood. In vivo, aggregation affects flows dynamics and flow resistance. There is now a general agreement regarding the correlations between elevated levels of fibrinogen or other large plasma proteins, as macroglobuline, and enhanced RBC aggregation. However other factors, such as the aging of the sample, also causes this aggregation phenomenon.

These red blood cells aggregates have a large influence in the viscosity of blood and it is important to understand its effect. Figure 10.1, show the formation of aggregates in a blood sample. Fig. 10.1a) show a picture taken the same day of the blood extraction, while Fig. 10.1b) shows the same sample of blood 5 days after its extraction.

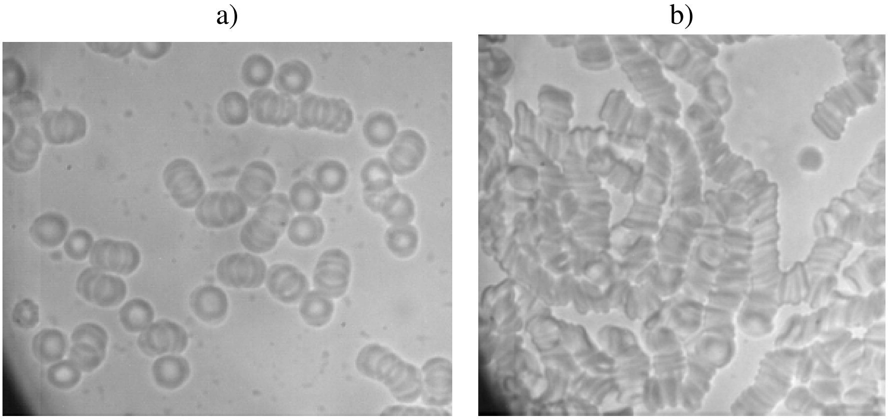

Figure 10.1: *Red Blood Cells on a 48% hematocrit blood sample at rest. Figure a) shows blood on the same day of the extraction of the sample and Figure b) shows blood at the 5th day from the extraction of the sample. We can see how a higher amount of rouleaux are formed after 5 days. The image was taken with an inverted microscope Optika XDS-3 and a* $100\times$ *objective.*

As mention before rouleaux formation has several causes, but based on what it is seen in Figure 10.1 we will center in the changes of the viscosity of blood based on the aging of the sample.

From a computational point of view several models to define the aggregation of red blood cells have been developed [Neu and Meiselman, 2002; Liu and Liu, 2006; Fedosov et al., 2011] but these have not been able to extrapolate well to experiments.

This chapter will be dedicated to introduce a scaling theory for red blood cells aggregation, due to the aging of the sample, based on some of the computational model developed.

10.1.1 Aggregation by a Morse Potencial

In the previous chapter we have obtained the viscosity values for different blood samples and hematocrit concentrations using 3 non-Newtonian models. In order to further understand our experimental results, we proceed to formulate a scaling theory for the viscosity. This theory is carried out by the introduction of a scaling parameter.

In order to introduce such parameter, we consider an aggregation number, C, defined as:

$$C = \frac{\eta_0 \dot{\gamma}_F a^3}{D_e} \tag{10.1}$$

where D_e is the well-depth of the potential of the energy associated to the aggregation forces between RBC's [Liu and Liu, 2006].

The scaling basis is that if we plot the non-Newtonian viscosity of the blood sample, η, as a function of the aggregation number, all curves should collapse onto a single universal scaling law. The aggregation energy can be approximated by a Morse potential, U_a, as:

$$U_a = D_e \left(e^{2\beta(r_0 - r)} - 2e^{\beta(r_0 - r)} \right), \tag{10.2}$$

where r is the separation between RBC's, r_0 is the zero-force distance and β characterizes the interaction range [Fedosov et al., 2011].

Assuming that non-Newtonian behavior at these scales is associated to aggregation of RBC's, we can use this scaling argument to characterize aggregation within our experimental blood samples.

Since the quatity C is written as a function of η_0, we simplifies the expression for the viscosity as a function of the blood plasma as:

$$\eta_{eff} = \frac{\eta(\dot{\gamma}_F)}{\eta_0} \tag{10.3}$$

We will refer to Eq. (10.3) as effective viscosity, since it is normalized with the blood plasma viscosity η_0. To visualize this scaling we compared two blood sample of the same hematocrit (same donor) but different ages. Figure 10.2, shows the normalized viscosity of both samples for 1 and 5 days old.

We clearly appreciate that the viscosity of the 5 days sample is higher than the effective viscosity of the 1 day sample. Since both sample have the same hematocrit this increase is solely due to RBC aggregation. In order to quantify how aggregation

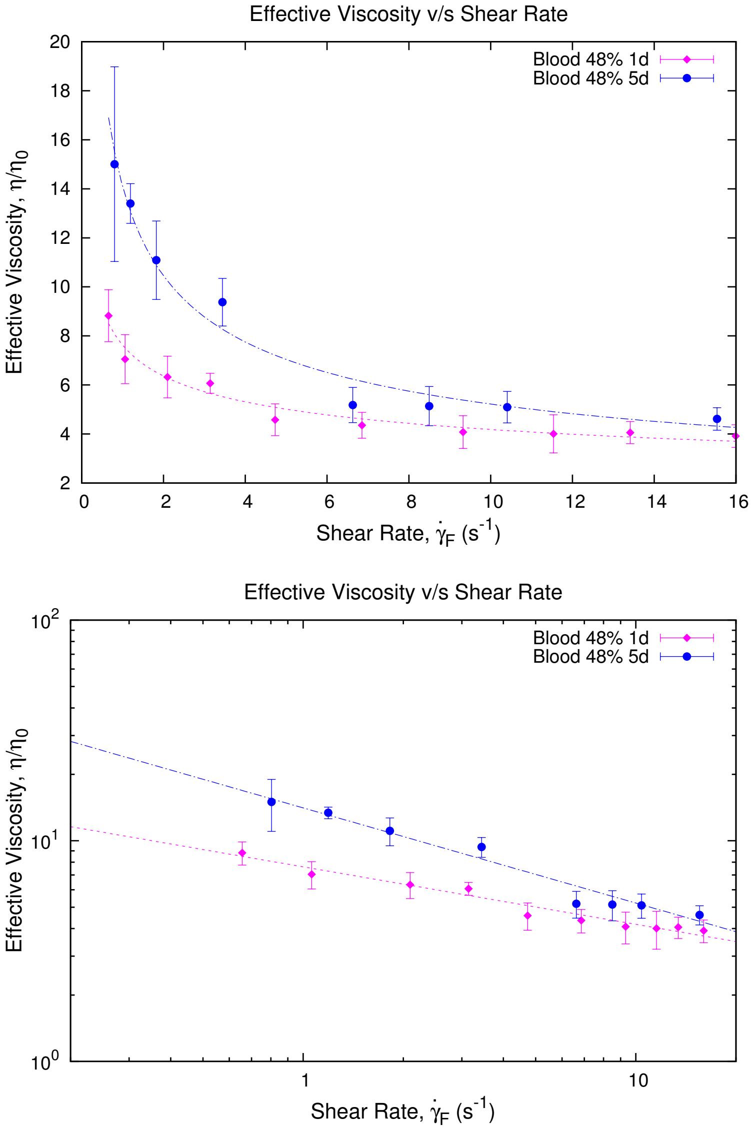

Figure 10.2: *The figure shows the effective viscosity* ($\frac{\eta}{\eta_0}$) *against shear rate* ($\dot{\gamma}_F$) *for a blood sample of 48% hematocrit, measured at* $20°C$ *in 2 different days, 1 day old sample in magenta and 5 days old sample in blue.*

induces this viscosity increment we establish a relation between the sample viscosities by means of an aging factor, k_a, defined as:

$$k_a = \left(\frac{\eta_{e5d}}{\eta_{e1d}}\right)^2 \tag{10.4}$$

Since shear rate is n-dependent, the Non-Newtonian and Newtonian regimes are considered separately. The last step of the scaling consist of writing the normalized viscosity of blood as a function of the capillary number which depends on the aggregation energy correspondent to each sample. For an unaggregated sample, $D_e \approx 2\times10^{-20}(J)$ which is increased by $k_a = 2.96$ in the non-Newtonian regime and $k_a = 1.37$ in the Newtonian regime, for the 5 days aggregated sample. In this case the viscosity of both regimes, show changes which are assumed a consequence of the aggregation of RBC's due to the aging of the sample.

10.1.2 Scaling theory of aging effects

We start our analysis by addressing the effects of aging on blood viscosity Figure **??** show that, as the sample ages, RBCs organize themselves into structures called rouleaux. Simulation results reported in have showed that the aggregation of RBCs into such structures affects the rheological properties of blood.

Our experimental results Figures 10.1a) and 10.1b) show that rouleaux appear due to aging of the samples, whereby we put forward that aging also affects blood viscosity.

To analyse the effects of aging, we fix the value of the haematocrit and study the behaviour of the blood sample as it ages. We introduce a new, non-linear scaling parameter, the adhesion scaling number, A, which quantifies the effects of aging on RBC aggregation. This quantity is defined as:

$$A = \frac{\eta_0 \dot{\gamma}_F(n) d^3}{E(\dot{\gamma_F}, a, E_0)} \tag{10.5}$$

where η_0 is the viscosity of plasma, E is the energy scale associated to the aggregation forces between RBCs [Fedosov et al., 2011], which depends on the shear rate, $\dot{\gamma_F}$, the age of the sample, a, and a reference value of RBC aggregation, $E_0 \approx 500 k_B T$. d is the average diameter of a red blood cell, $d \approx 7.8 \mu m$. A can be interpreted as the ratio between the characteristic viscous energy scale and the aggregation energy.

Our scaling Ansatz claims that the viscosity, η depends on the adhesion scaling number, A, alone:

$$\eta \approx \eta_0 A^{-\alpha} \tag{10.6}$$

with $E(\dot{\gamma}_F, a, E_0)$ where the scaling factor k_a is a function of $\dot{\gamma}_F$ and a. The scaling factor is obtained by collapsing the curves for the variation of the viscosity as the shear rate changes, see Figure 10.2 corresponding to 48% hematocrit. Results shown in Figure 10.3 shows that our scaling Ansatz can accurately account for the variation of viscosity with age. We also note that our scaling Ansatz leads to larger aggregation for older blood samples, as it should be expected. Similarly, as we increase the shear rate, we observe that k_a also changes. This change is associated with the presence of rouleaux at lower shear rates.

In figure 10.3 we appreciate how this scaling enables the collapse of the normalized viscosity curves which supports our hypothesis.

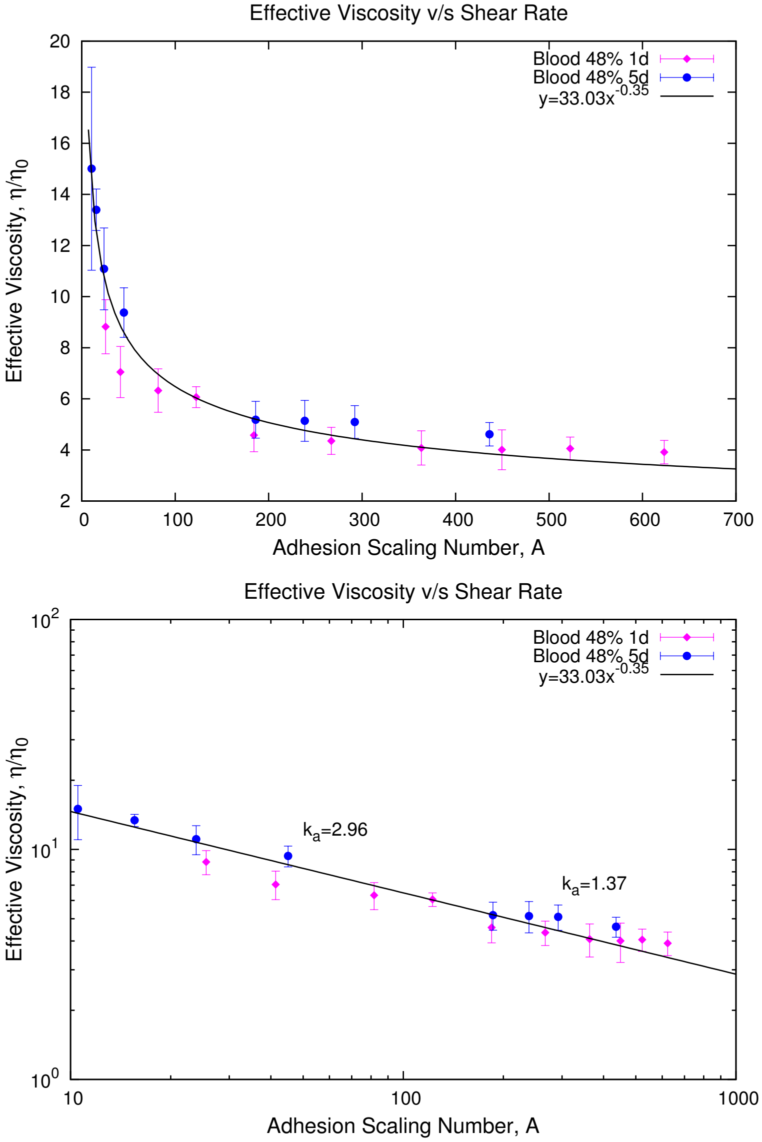

Figure 10.3: *The figure shows the effective viscosity of the blood samples against the Adhesion Energy, A, correspondent to the non-Newtonian ($k_a = 2.96$) and Newtonian ($k_a = 1.36$) regimes. We appreciate the collapse of the viscosity curves as a result of our scaling method.*

10.2 Bending Scaling

As mention before in this tesis, there are several features of red blood cells that affect blood viscosity. One is aggregation of RBC's which we analized in the previous chapter using a sample of different ages. Another feature is red blood cell deformability and membrane elasticity, this feature is particular to each blood sample and may define some specific diseases related to RBC's bending modulus of the membrane [Fedosov et al., 2010; Lázaro, 2014]. As it was done in the previous chapter we base this analysis in computer simulation [Lázaro et al., 2014a].

Red blood cells mechanics are very sensitive to the elastic properties of their membrane. The elasticity energy is described by the Helfrich bending energy [Helfrich, 1973] which depends on the bending rigidity and the curvature of the RBC membrane. Since experimentally we are not capable of determine the real features of the RBC membrane of our blood samples we need to find a simpler way of determined the differences in rigidity of different samples.

In order to the incorporate our experimental results to see how blood viscosity is affected by RBC's, we first need to obtain an effective viscosity value of the blood sample as a relation with its solute. In this particular case blood plasma. By means of the Darcy equation for a fluid inside a microchannel we define this effective viscosity as:

$$\eta_{eff} = \frac{\frac{A\Delta P}{v}}{\frac{A\Delta P_0}{v_0}} = \frac{v_0 \Delta P}{v \Delta P_0} \tag{10.7}$$

where A is a constant value that depends on geometrical parameter of the experimental setup, The effective viscosity, η_{eff}, is obtained for each hematocrit comparing with the blood plasma viscosity, η_0, of the sample. Figure 10.4 shows the effective viscosity for a blood sample separated in different red blood cells concentrations. We can observe how the effective viscosity values are different for each and so are the viscosity exponents of the fitted functions.

10.2.1 Hematocrit Normalization

In this case, the sample have been divided in different red blood cell concentration and the difference in the effective viscosity values is due to each concentration. In order to discard that the hematocrit is playing a role in the viscosity respond of the sample we had to come up with a normalization strategy for the sample. So, to normalized the samples with respect to their hematocrit we consider the value of the original hematocrit of the sample ϕ_{max}, and the hematocrit of the reduced RBC's concentration of the sample ϕ [Pries et al., 1992]. The relation for the normalization of a blood sample at different hematocrits is given by:

$$\eta_{norm} = 1 + \left(\frac{\eta}{\eta_0} + 1 \right) \frac{\phi_{max}}{\phi} \tag{10.8}$$

Figure 10.5 shows how the different values of the viscosity, at high shear rates and low hematocrit, collapsed using the normalization rule from Eq. (10.8). We can

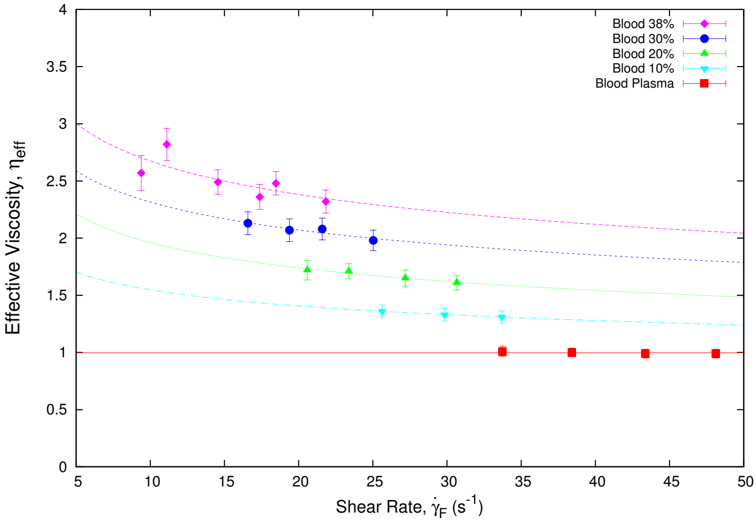

Figure 10.4: *The figure show the efective viscosity, η_{eff}, as a function of the shear rate, $\dot{\gamma} = \dot{h}/b$, of a blood sample at different hematocrit.*

infer from this result that the viscosity differences are due solely to the difference in the RBC's concentration. Thus, if we developed the same normalization process for different samples (different donor) and no collapse is observe, the differences in the effective viscosity should be given by other features of blood, such the difference in their red blood cells properties.

To check this hypothesis we have obtained the effective viscosity as a function of the channel shear rate, $\dot{\gamma} = \frac{v}{b}\,(s^{-1})$ of two healthy blood samples, 48% and 38% htc. and two anemia blood samples of 25% and 33% with αthalassemia, see figure 10.6a. . Since the samples do not share the same RBC's concentration we need to perform the normalization process of the viscosity. This way to be certain that the feature differences in the viscosity between the samples is not due to their different hematocrit but to their difference in red blood cells. Figure 10.6b, shows how after the normalization of their hematocrit the differences in viscosity still exist and a new parameter needs to me added to make the curves collapse.

10.2.2 Bending Coefficient

We define this new parameter as an adimensional capillary number, C_a. The capillary number is defined as the ratio between the elastic and the viscous relaxation time of the RBC membrane[Lázaro et al., 2014a]. The definition is given in equation (10.9), as a function of the viscosity of the sample's plasma η_0, the average size of the red blood cell a, and the shear rate.

$$C_\kappa = \frac{\tau_k}{\tau_\eta} = \frac{\eta_0 a^3}{\kappa}\dot{\gamma} \qquad (10.9)$$

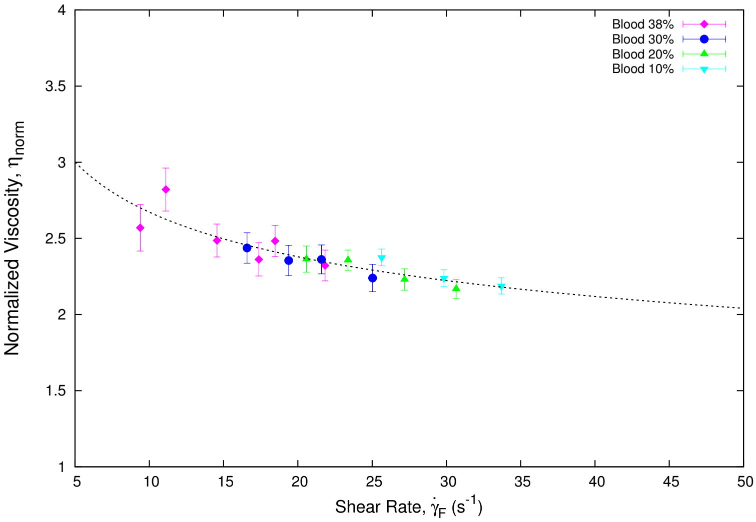

Figure 10.5: *The figure show the normalized viscosity, η_{norm}, as a function of the shear rate, $\dot{\gamma} = \dot{h}/b$, of a blood sample at different hematocrit. We observe the collapse of the high shear rate viscosity values for low percentage of hematocrit.*

Comparing the normalized viscosity of the blood samples with respect to the pressure (see figure **??**) we may be able to established a relation between the viscosity and a control parameter, C_k, which depends on the bending coefficient as shown in equation 10.10. Here $B = \eta_0 a^3$ is a constants parameter, κ is the red blood cells bending coefficient and $\dot{\gamma}$ is the shear rate.

$$C_\kappa = \frac{B}{\kappa}\dot{\gamma} \tag{10.10}$$

Comparing shear rates for the different samples at the same injected pressure we may use the definition in equation 10.10 to establish a relation between the bending coefficients from the anemia blood sample with respect to the healthy blood sample. For $\Delta P_a = \Delta P_h$ we have:

$$\begin{aligned} C_{\kappa_h} &= C_{\kappa_a} \\ \frac{B}{\kappa_h}\dot{\gamma}_h &= \frac{B}{\kappa_a}\dot{\gamma}_a \\ \frac{\kappa_h}{\kappa_a} &= \frac{\dot{\gamma}_h}{\dot{\gamma}_a} \\ \frac{\kappa_h}{\kappa_a} &= 0.66 \end{aligned}$$

Figure **??** shows the collapse of the normalized viscosity curves due to the rescaling of the bending coefficient $\kappa_a \approx \frac{3}{2}\kappa_h$.

Using the definition of the capillary coefficient in eq. 10.10 and considering that the bending coefficient, κ, of a healthy blood sample is $\kappa_h \approx 2 \times 10^{-19}\,(J)$ we may

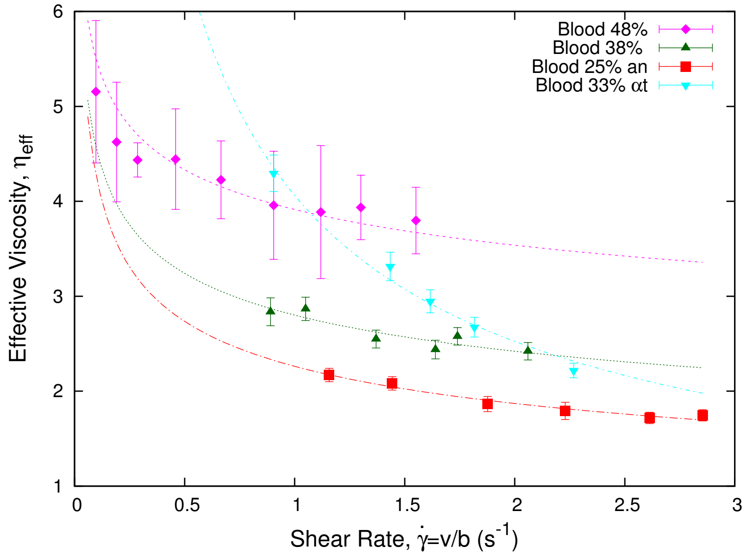

(a)

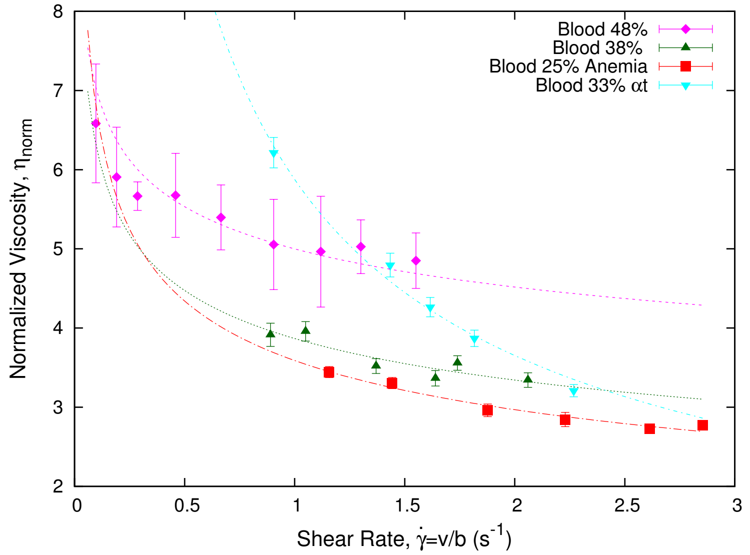

(b)

Figure 10.6: *Figure (a) shows the effective viscosity against shear rate and figure (b) the normalized viscosity of different blood samples. A 48% hematocrit, 38% htc., Anemia Blood at 25% htc. (red) and Alphatalasemia Blood of 33% htc.*

plot the normalized viscosities of the blood samples as a function of their bending coefficients. These viscosities values are then define in equations 10.11 and 10.12 and show in figure 10.7.

$$\eta_h = \eta_{h\,norm}\frac{\kappa_h}{\kappa_h} \tag{10.11}$$

$$\eta_a = \eta_{a\,norm}\frac{\kappa_a}{\kappa_h} \tag{10.12}$$

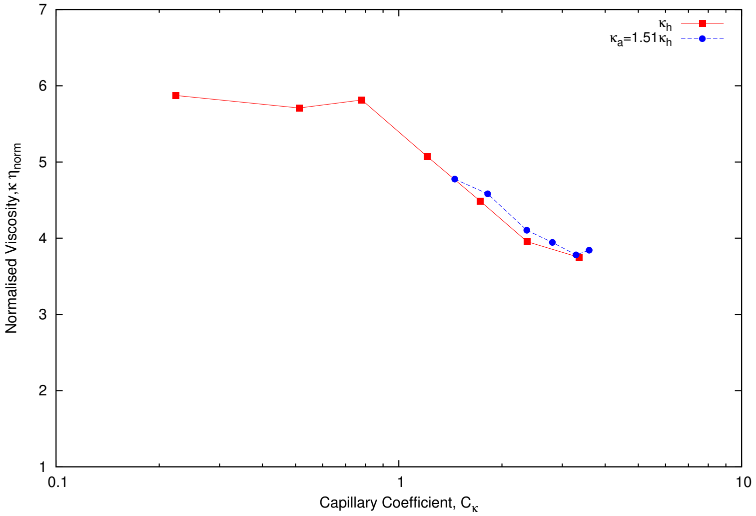

Figure 10.7: *Normalized Viscosity v/s C_κ, for the healthy blood sample, κ_h, compared with the anemia blood sample, κ_a. We use a re-scaled value of the viscosities as a function of the bending coefficient from equations 10.11 and 10.12.*

10.3 Conclusion and discusion

We have shown that variations in the non-linear viscosity of blood associated to aging can be explained by means of a scaling theory based on the introduction of an adhesion scaling number Eq. (10.5). This quantity is defined as the ratio between the viscous energy and the aggregation energy. Our scaling theory allows us to quantify the increase in aggregation energy by aging with respect to its reference characteristic scale, E_0. The increase in the characteristic aggregation energy is given by the aging factor, k_a, which is observed to increase a the sample ages. We further show that the viscosity exhibits power-law behaviour over almost two orders of magnitude as a function of the scaling parameter A. We observe that blood exhibits non-Newtonian behaviour for large haematocrit, which, at the shear rate scales of our experiments, is associated to aggregation of RBCs. These results allows us to better characterise the non-linear microrheological behaviour of blood.

A strength of our approach comes from the introduction of a novel front microrheometer that allows to extract bulk non-linear viscosities from the simple observation of a moving air-fluid interface.

The second part of this chapter we were able to obtained an alternate scaling method but this time related to the bending coefficient of the red blood cells membranes.

The main achievement in this chapter is through this viscosity scaling processes we were able to relate blood as a continuous fluid, with features of it at a cellular level.

PART V

Electronical Detection

Electronical Detection of a Fluid Front

The great achivements of microfluidics related to medicine is to aims easy diagnostic of diseases, and to incorporate all that is necessary to perform a measure inside on a simple device. This devices are known as Lab on a Chip or μTas devices. In order to extend our device and method to a higer level of function, we have collaborated with the Electronic Department of the Faculty of Physics of the University of Barcelona. Based on the control of the fluid front, we have been able to compared results obtained with our optical detection method with an electronical detection device.

This chapter is dedicated to compared the results from our optical detection method with the electronical detection method. In Section 11.1 we will describe the main features of this new integrated electronical device and in Section 11.2 the results obtained with both method will be compared.

11.1 Electronical Device Principles

The designs for the detection system consist of and array of eight electrodes located equidistant from the central axis of the channel. The distance from centre to centre of the platinum electrodes is x=1.6mm deposited on a PET (polyethylene terephthalate) polymer.

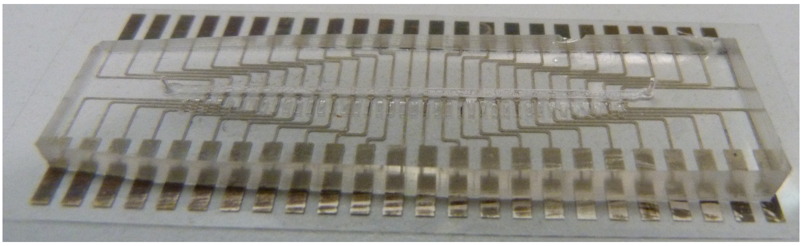

Figure 11.1: *Image of the microchannel over the PET which contains the electrodes.*

The electrodes may be disposed face-to-face or interdigital. They work like two terminals of an electrical switch activated by the fluid through the channel. The switch is turned on when the fluid reach the two electrodes simultaneously. At that point, a short circuit is created between them and an electrical current circulation starts to flow [Tañá et al., 2016]. Figure 11.3, shows the sequence of a front arriving to an electrode.

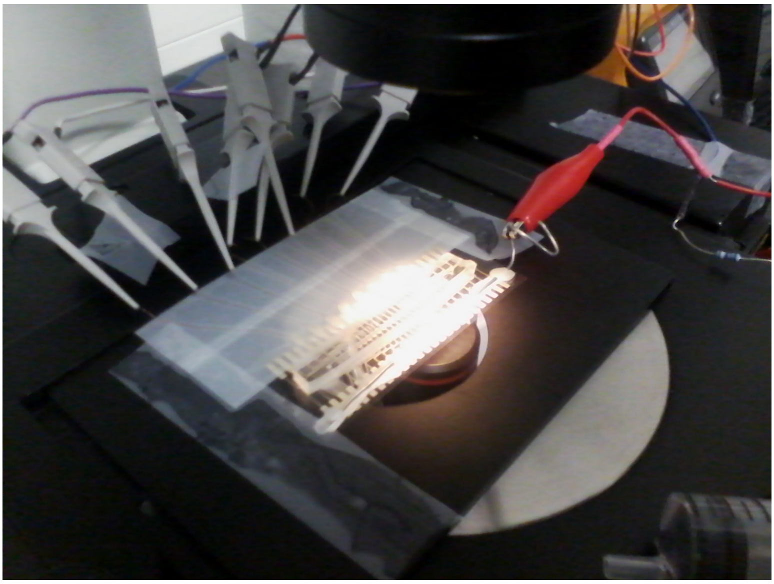

Figure 11.2: *Image of the microdevice with the electrodes conected to a power source, set over the microscope.*

We can see that in Figure 11.3a) only six light are turned on, while in Figure 11.3c) when the fluid interface has reached both electrodes a seventh light is turned.

Once the voltage is at the digital input, the control software starts to count the delay time between the activation of the different electrodes along the channel. The time between each conections is counted and since the distance between the electrodes is known the velocity can be easily calculated.

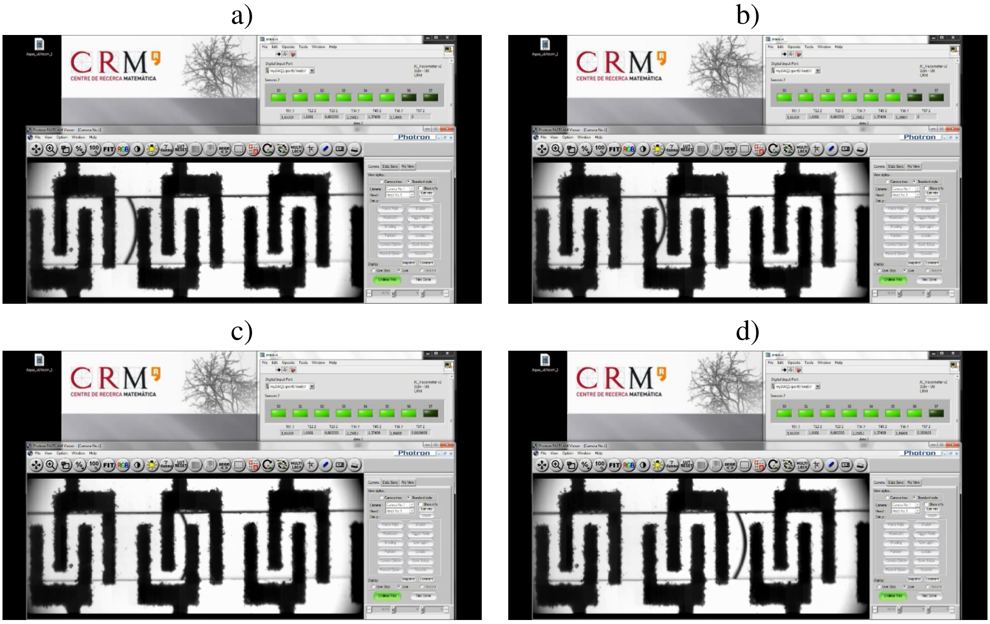

Figure 11.3: *Image of the interfase of the electroreometer and the optical capture of the fluid front. The figures show the sequence of a water front moving through the microchannel. In image a) we see 6 light on while in image c) we see a seventh light turned on once the fluid front has made contact with both electrodes.*

11.2 Optical versus Electronical Results

In the previous parts of this thesis we took advantage of the control of the capillary filling with constant velocity, so that the position where the measure was taken wasn't a parameter to take into account.

As an initial test we selected a height of the fluid column of $H = 300\,mm$, and we tested 3 different fluid in a microchannel of $b = 300\,\mu m$, water, ethylene.glycol at 5% volume concentration and ethylene-glycol at a 25% volume concentration and we compared the velocities obtained for each fluid, see Table 11.1. We can see from the table that the error between both measures are low less than a 2.5%.

Fluid	Optical Detection $v(mm/s)$	Electronical Detection $v(mm/s)$	Error $\%$
Water	2.105	2.0753	1.41
Etgl. 5%	1.903	1.9457	2.24
Etgl. 25%	1.089	1.0710	1.65

Table 11.1: *Comparison of the velocities obtained with the two different detection methods in a channel of* $b = 300\,\mu m$*. The fluids are submitted to an hydrostatic pressure of* $\rho g H \approx 3000\,Pa$*.*

A reliable velocity results is the firts step in other to entend the study to different exerted pressure and obtain the velocity response, which eventually will lead us to determined the viscosity of these fluids.

11.2.1 Viscosity of water

We measure the viscosity of water using both detection method, the usual optical detection method and the electronical detection method. The general setup was not changed, only the channels. We used the same principles used in the case of water in Chapter 5.

First, we obtained the velocity response of water at different exerted hydrostatic pressures, i.e. fluid column heights and we compared the results with the ones obtained using the optical detection, and the expected theoretical response. This results are shown in Figure 11.4.

Eventually, we calculated the rescaled stress and a shear rate for the data obtained with the electronical detection, see Figure **??**. From the fit to power-law, we obtained the general viscosity value of the fluid η and the exponent n, this values are shown in Table 11.2.

The viscosity values for each shear rate, were obtained by means of equation:

$$\eta = \frac{\sigma_{rs}}{\dot{\gamma}} \tag{11.1}$$

Again the results obtained with the micro-electro-viscometer were compared with the results from the optical detection, the viscosity comparison is shown in Figure 11.6, where we can see a big difference between both results.

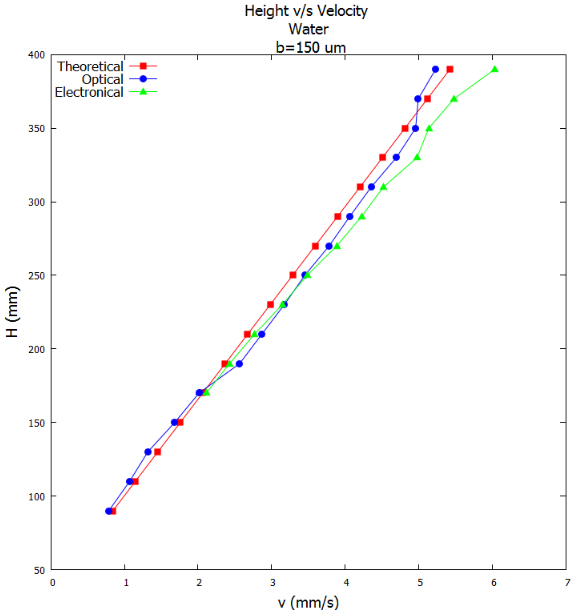

Figure 11.4: *Height as a function of the velocity of water. We compared the results obtained with the optical and electronical detection and the expected teoretical results in a microchannel of* $b = 150\mu m$.

Fluid	Viscosity $\eta\,(mPas)$	Exponent n
Optical Detection	1.02 ± 0.02	1.001 ± 0.006
Electronical Detection	0.900 ± 0.003	0.99 ± 0.02

Table 11.2: *Comparison of the viscosities of water obtained with the two different detection methods in a channel of* $b = 150\,\mu m$.

We can see from Table 11.2 that there is a big gap between the viscosity results obtained for water using the optical and electronical detection, with an error of 11.7%. This difference may be due to several main reasons. First, the substrate where the microchannel is set is from a diferent material in both cases. In the case of the optical detection the substrate is glass which has a contact angle with water of $\theta = 40°$, whereas PET has a contact angle with water of $\theta = 78°$. In both cases the contact angle is hidrophylic but the curvature of the fluid-interface is dominated by the PDMS, which make this option not convincing. The second reason is more believable, and it is due to the height of the microchannel been affected by the presence of the electrodes. These decrease the average height of the microchannel or may be generating a sort of pinning or faquir effect inside the channel which increase the velocity of the front. Last, the temperature inside the channel can be elevated due to the action of the electrodes which decreases the viscosity of water.

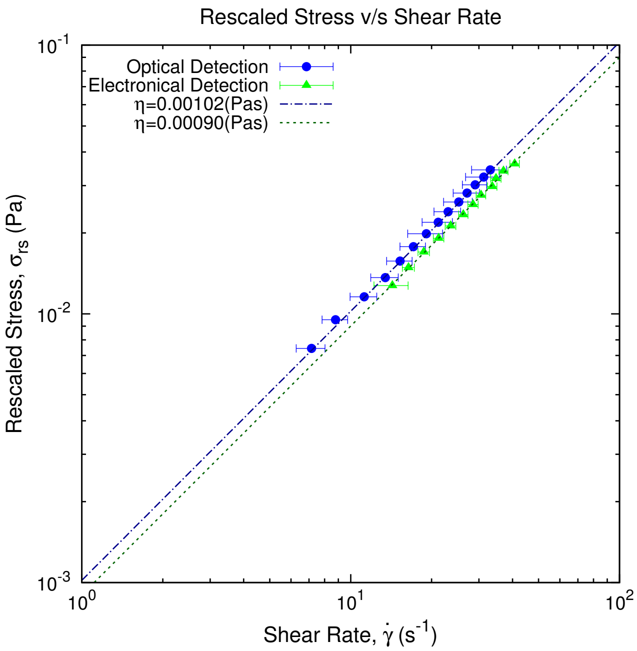

Figure 11.5: *Rescaled stress as a function of the shear rate for water in a microchannel of* $b = 150\,\mu m$*. We compare the results for the optical and electronical detection method. In both cases the power law fit delivers the response of a Newtonian fluids* $n = 1.001$ *and* $n = 0.99$*, respectively.*

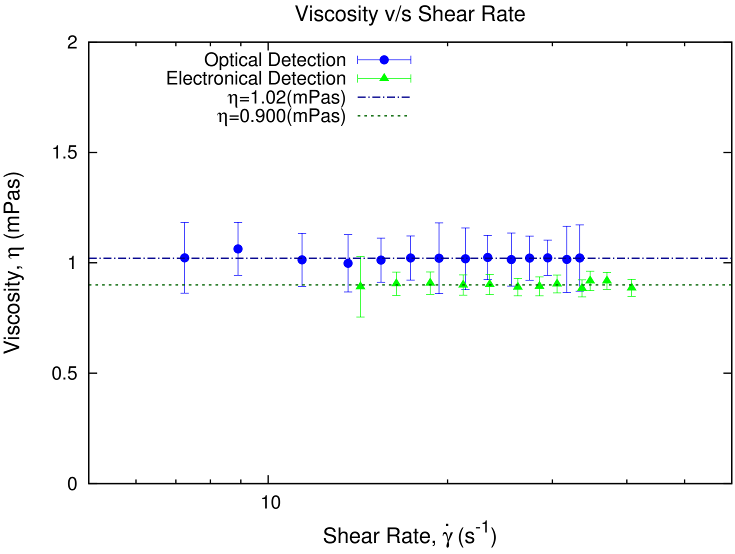

Figure 11.6: *Viscosity as a function of the shear rate for water in a microchannel of* $b = 150\,\mu m$*. Here compare optical and electronical detection method, and we see a big difference between both viscosity estimations.*

11.3 Conclusions

Even though the results obtained with both detection method have a percentual error of $e = 11.7\%$ for the viscosity measures, we are still not sure what causes this big differences. The fact that the velocity measures in Table 11.1 does not shown such a error between both method may give us a clue. Since the velocity measures are taken inside a higher microchannel, it may indicate that the presence of the electrodes in microchannels with lower gaps can have a bigger effect than those of higher gaps.

The biggest advantage of the electronical detection method and the controlled capillary filling at constant velocity is that we can obtained the mean velocity of front along the whole microchannel in a single measure, instead of capturing the velocity of the fluid interface by segments. This makes the measure to progress quickly and simplifies the analysis of the images.

PART VI

Conclusions and Future Perpectives

CHAPTER 12

Conclusions

The primary objective of this work was to study the viscosity of blood and some of its non-Newtonian properties, by means of a simple optical detection method based on tracking the blood-air interface moving inside a microchannel. In order to achieve this, we first had to developed a microfluidic device and method which allow us to obtain a clear image of the fluid front. This was made using a microscope and a high speed camera. The images were analyzed by means of a computational code developed in Wolfram Mathematica©. The thesis work has been mainly experimental, and our results have been compared with theoretical and bibliographical results. The original results from this thesis are separated in two parts, which are summarized as follows.

12.1 Newtonian Fluids

The first part of the research, Part III, was dedicated to the study the interface fluid-air of flows of Newtonian fluids in order to achieve reliable viscosity results with our device and method, and prove our system as a viscometer.

In Chapter 5, we study a water front inside the microchannels, in order to characterized them. We developed experiments at different channel heights ranging from $b = 50\,\mu m$ to $b = 350\,\mu m$. We study the position of the front as a function of time and we obtained that for channel gaps higher than $b = 150\,\mu m$ the exponent of a power law relating the position of the mean front as a function of time is, $\nu \approx 1$. This results implies that the velocity of the water interface along de microchannel was constant. In order to verify this result, we also analyzed the velocity of the water as a function of the position, and we obtained that effectively the velocity remains constant along the channel.

Relating the hydrostatic pressures exerted to the fluid inside the microchannel and the velocity response obtained from the water front, we observed a linear response which defines water as a Newtonian fluid, just as expected. Meaning that its viscosity does neither depends on the stress applied (pressure), nor the shear rate. This was demonstrated for several microchannel gaps.

The final step of this study was to obtain a reliable value of the viscosity of water. Taking into account the geometry of the coupled system for our setup, we were able to obtained the viscosity of water for different channel gaps. The water viscosity value obtained was $\eta = 1.02 \pm 0.02\,cP$ (at room temperature), which match well the known value of the viscosity of water.

One of our most relevant results is that using channel of different heights and scaling the stress, we can extend the shear rates ranges to characterized the fluid front, maintaining his viscosity values unaltered.

In Chapter 6, we extend the studies performed with water to other Newtonian fluids, we were able to obtain the viscosity of Ethylene-glycol at 40% and 44% volume concentration and Glycerol at 19% volume concentration with an error of less than a 10%.

We were also capable to obtain the viscosity of different samples of blood plasma (different donors) and differentiate each sample without an overlap of the values. The viscosities values obtained for the studied fluids are shown in Table 12.1.

Fluid	Micro-device	Rheometer	bibliog.
Water	1.02 ± 0.02		1
Ethylene-glycol 44%	3.517 ± 0.009	3.3	3.34
Ethylene-glycol 40%	2.87 ± 0.02	2.7	2.86
Glycerol 20%	1.96 ± 0.03	1.93	1.76
Blood plasma A	1.716 ± 0.01	1.84	1.81
Blood plasma B	1.55 ± 0.02	1.62	1.81

Table 12.1: *The table shows the viscosity values obtained with our device and method at room temperature, compared with the values obtained from a macroscopic rheometer and bibliographical data. References to this fluids viscosities are addressed in Appendix C.*

In Chapter 7, due to a modification on the experimental setup, we study the behavior of a system of two different fluids. We studied the fluid inside the channel pushed by a fluid with equal and different densities and different viscosities. We observed a slight acceleration or deceleration of the fluid front, that was not present in the single fluid system.

In this case, to determine the viscosity of the fluid inside the microchannel we used a two immiscible fluids model. We accurately determined the viscosity of water and ethylene-glycol at 40% volume concentration as a function of the height of the fluid column. This results are shown in Table 12.2.

Fluid	$b = 300\,\mu m$	$b = 200\,\mu m$
Water + Gl. 30%	0.98 ± 0.03	0.97 ± 0.04
Etgl.40% + Gl. 20%	2.9 ± 0.1	3.0 ± 0.2

Table 12.2: *The table shows the viscosities values of water and ethylene-glycol 40% using the 2 fluids system for 2 different channels.*

As a summary, the main results of this part of the work are:

- We were able to control the velocity of the fluid-air interface inside the channel in order to obtain a constant value, for different channel heights.

- The range of shear rate can be extended by simply changing the geometry of the microchannel, i.e. the height of the gap.

- With our device and method, we calculated the viscosity of 4 different Newtonian fluids as a function of the shear rate, with an accuracy of less than a 8%. And with better results at low shear rates than the tested rheometer.

- At the presence of a system with fluid with two different viscosities, the method is still reliable in the calculation of the viscosity of the fluid inside the microchannel.

12.2 Blood and non-Newtonian rheometry

The second part of this thesis, Part IV, is dedicated to extend the results for Newtonian fluid to blood. Blood is essentially a difficult fluid to manipulate and study. In general, it presents non Newtonian properties as shear thinning, meaning, that its viscosity decreases as the stress or the shear rate increases. This non Newtonian properties are due to plasma proteins and especial characteristics of its red blood cells.

In Chapter 9 we studied the blood from a macroscopic point of view. The viscosity of blood has a direct dependence on the percentage of hematocrit, which means, that if the hematocrit decreases also does its viscosity. An alternative way to describe this behavior, was relating the hematocrit with the velocity of the fluid front, in this case, if the percentage of hematocrit increases the velocity of the fluid front decreases.

To study blood viscosity, we observe its velocity response inside the microchannel when different hydrostatic pressures are exerted. We analyzed its response using 3 different non-Newtonian model: a Power Law model, the Weissenber-Rabinowitch-Mooney method (widely used in rheometry) and a third model were the shear rate depends on the viscosity exponent from the power law fit. We have been able, with each model, to describe the non-Newtonian behavior of blood and observe its shear thinning properties for several, healthy and sick, blood samples. This results are shown in Tables 12.3 and 12.4. References to the bibliographical values of blood are addressed in Appendix C.

In order to establish a relation between blood viscosity and the properties of its red blood cells, we developed two scaling models, which were presented in Chapter 10. In both cases, a normalization process as a function of the percentage of hematocrit was performed, to discard that the differences in viscosity were due to the red blood cell concentration of the sample.

In Chapter 10 we studied the viscosity of blood related to the aggregation properties of its red blood cells. We developed a scaling model for a sample of blood at different days from its extraction, comparing the aggregation levels of its red blood cells. For this, we defined an adimensional quantity based on a Morse Potential model. By mean of this model, we were able to collapse the viscosity curves of a sample with different aggregation levels. Which implies that the increase of the viscosity values of the sample are given, primarily, by the aggregation properties of its red blood cells.

Hematocrit %	$\eta\,(cP)$ $100\,(s^{-1})$
48 1d	5.3 ± 0.4
48 5d	5.3 ± 0.7
25 2d	2.84 ± 0.04
25 6d	2.72 ± 0.02
Blood Plasma	1.55 ± 0.02

Table 12.3: *Viscosity of blood at shear rate of* $\dot{\gamma} = 100\,(s^{-1})$ *for two different hematocrit of an original blood sample of 48% of hematocrit at* $20°C$. *Measured at different days from extraction.*

Hematocrit %	$\eta\,(cP)$ $180\,(s^{-1})$
38	3.6 ± 0.2
30	3.2 ± 0.2
20	2.7 ± 0.1
10	2.20 ± 0.09
Blood Plasma	1.61 ± 0.06

Table 12.4: *Viscosity of blood at a shear rate of* $\dot{\gamma} = 180\,(s^{-1})$ *for different hematocrit percentages of a decomposed blood sample of 38% of hematocrit at* $20°C$.

Also in this chapter we studied how the viscosity of blood is related to the elasticity of the cellular membrane of its red blood cells. In this case, we defined an adimensional quantity which relates the bending coefficient of the cellular membrane of red blood cell of different samples. In this matter, we compared healthy blood samples with anemic blood samples. Expressing the viscosity as a function of the defined adimensional quantity, we observed a collapse of the viscosity curves from both samples. This result implies that the viscosity of two samples may be described as a function of the bending coefficient of the cellular membrane of their red blood cell.

As a summary, the main results of this part of the thesis are:

- We relate the viscosity of a blood sample to different hematocrit percentages, and accurately normalized its hematocrit percentages.
- Using three different non-Newtonian models, we describe the non-Newtonian behavior of blood and observe it shear thinning properties for several, healthy and sick, blood samples.
- We were able to obtain reliable values of blood viscosity, compared with early results from bibliographical resources.
- We establish a relation between the viscosity of a blood sample and its aggregation levels, based on the time from extraction of the sample.
- We establish a relation between the viscosity of a blood sample and the bending coefficient of the cellular membrane of its red blood cells.
- The biggest breakthrough of this last two results, is that by studying blood as a continuous fluid we can understand and quantify particular features occurring at the cellular level.

Future Perspectives

This work started with the idea of simply measuring the velocity of a blood front inside a microchannel, with a simple setup, through which we were able to estimate the viscosity of the blood sample. We test our results previously with Newtonian fluids and then we directly passed to the study of blood. However, many interesting subjects arose during the development of this thesis and has open several new options to explore. This chapter is dedicated to discuss some open questions for future research.

13.1 Hydrophilic microchannels

From a Newtonian point of view new studies have arise using the same device and method but changing the properties of the microchannels, from been hydrophobic to hydrophilic. This is made changing the properties of the PDMS, using chemicals (HEMA) and oxygen plasma. This change has various objective. First it is easier to perform the measurements because the complete setup is simplified. The reservoir of liquid and the tube disappear and the fluid moves simply by setting a drop over the channel inlet, which enter the channel using capillary forces. This modification can be very important in diagnostic at point of care since only the devices would be needed.

13.2 Blood and aging for different hematocrits and temperature

We are also interested in studying the relation of blood hematocrit and aging. And how the level of aggregation of red blood cells affects the viscosity of a blood sample at different hematocrits. And observe if the Morse Potential model is still useful in this case. All of our research has been carried out at room temperature, between 20 and $25°C$, so it would be interesting to see how temperature affects viscosities values blood and the aggregation level of red blood cells, specially considering that in the human body normal temperatures are between 36 to $37°C$. This would give us a better understanding of how blood behaves inside the human body.

13.3 Other non-Newtonian fluids

Since our main objective was to direct our work to the study of blood we passed directly from Newtonian fluids to blood which has non-Newtonian properties. To study other non-Newtonian fluids may open several new perspective for our device and method, in order to relate other non-Newtonian properties of complex fluids, such as, its viscoelastic properties. In this case a temporal parameter should be inserted in our system to obtain the relaxation time response that define viscoelastic properties.

List of Publications

- *"Capillary filling at the microscale: Control of fluid front using geometry"*
  C. Trejo-Soto, E. Costa-Miracle, I. Rodríguez-Villarreal, J. Cid, T. Alarcón and A. Hernández-Machado.
  PLOS ONE, 2016, vol. 11, no 4, p. e0153559.

- *"Front microrheology of the non-Newtonian behaviour of blood: scaling theory of erytrocites aggregation by aging"*
  C. Trejo-Soto, E. Costa-Miracle, I. Rodríguez-Villarreal, J. Cid, M. Castro, T. Alarcón and A. Hernández-Machado.
  Submitted (2016)

- *"Collective behaviour of red blood cells in confined channels"*
  G. Rodríguez-Lázaro, C. Trejo-Soto, A. Hernández-Machado, I. Pagonagarraba.
  Preprint

- *"Optical versus electronical detection of fluid interfaces"*
  C. Trejo-Soto, L. Ortega, E. Costa-Miracle, I. Rodríguez-Villarreal, J. Colomer, T. Alarcón, P. Miribel and A. Hernández-Machado.
  In preparation

PART VII

Resumen en Castellano

Resumen en Castellano

14.1 Introducción

Desde los tiempo de Poiseuille, variadas técnicas para medir la viscosidad de la sangre han sido desarrolladas. Durante las décadas de los 60's y 70's con la aparición de los primeros reómetros las propiedades reológicas de la sangre fueron medidas y se determinó su comportamiento dependiente del gradiente de velocidad. Además se observó que posee un comportamiento pseudoplástico, es decir, que a medida que aumenta su velocidad su viscosidad disminuye.

Desde un punto de vista médico, la sangre y su plasma sanguíneo son los fluidos más eficaces para la detección de patologías globales. Estas patologías pueden estar relacionadas con su viscosidad, con las proteínas presentes en el plasma o con las propiedades de sus glóbulos rojos, como su agregación, deformabilidad o la capacidad elástica de su membrana celular.

En los últimos años con el nacimiento de la microfluidica, a principio de los 90's, nuevas técnicas para el diagnóstico de enfermedades se han desarrollado. La ventaja del uso de la microfluidica en el diagnóstico de enfermedades viene dada por el bajo requerimiento de muestra para realizar la detección, su portabilididad, la facilidad de uso y el bajo costo de su fabricación.

El objetivo de esta tesis ha sido el desarrollo de un dispositivo sencillo que permite obtener la viscosidad de la sangre con un error no superior al 10%. Además de ser capaces de relacionar su viscosidad con características específicas de sus células rojas como la agregación y la flexibilidad de su membrana.

14.2 Configuración Experimental

14.2.1 El dispositivo microfluídico

La fabricación del dispositivo microfluídico se realiza en 3 pasos. El primer paso consiste en realizar el diseño del dispositivo utilizando un software llamado Macromedia Freehand MX. La segunda parte del proceso consiste en la fabricación del molde del microcanal, para esto se utiliza una técnica denominada fotolitografía. En esta técnica se utilizan resinas fotosensibles negativas, que al exponerse a la luz cambian quimicamente y se endurecen dejando el molde impreso sobre un sustrato, en nuestro caso, vidrio. El último paso de la fabricación se denomina "Replica Moulding“ y consiste en imprimir el relieve del molde, hecho con fotolitografía, sobre un elástomero llamado PDMS. Este elástomero es una mezcla acuosa que se vierte sobre el molde y luego se deja en el horno a 65°C por 2 horas para que cure y se solidifique. Una vez curado, el PDMS es despegado cuidadosamente del molde donde el relieve de éste ha quedado impreso sobre el PDMS. El montaje del canal se realiza sometiendo el molde de PDMS y un sustrato de vidrio dentro de una cámara de limpieza de plasma de oxígeno por 10 segundos. Así, una vez terminado el barrido del plasma ambas superficies se ponen en contacto y quedan selladas irreversiblemente. La cavidad de aire que queda entre el vidrio y el PDMS es el microcanal. Las dimensiones de los canales utilizado para nuestros experimentos son: largo $l_c = 4\,cm$, ancho $w = 1\,mm$ y alto $b = 150$, 300 y $350\,\mu m$, figura 4.2.

14.2.2 Configuración experimental y captura de imágenes

Nuestra configuración experimental consiste en un depósito de líquido dispuesto a una altura H desde la entrada del microcanal conectado a éste por medio de un tubo biocompatible de radio $r = 127\mu m$, ver figura 4.4. El depósito está abierto en la parte superior ejerciendo un presión hidrostática, definida como $P_{hyd} = \rho g H$, que empuja el fuido del depósito dentro del canal.

El microcanal está dispuesto sobre un microscopio óptico invertido. El microscopio está conectado a un cámara de alta velocidad que captura la imagen de la interfase fluido-aire (frente de fluido) moviéndose dentro del microcanal, ver figura 4.5. La velocidad de captura de la cámara se estima previa al experimento, desde 60 cuadros por segundo a 1000 cuadros por segundo, dependiendo de la presión inyectada, el tamaño del microcanal y el fluido en estudio.

Las imágenes obtenidas son pasadas por un código en Wolfram Mathematica que permite calcular la velocidad instantánea del frente. El cálculo de velocidad se hace analizando en imágenes consecutivas el cambio de la posición promedio del frente, dentro de una escala de tiempo definida por la velocidad de captura de la cámara. Una vez obtenido el perfil de velocidades instantáneas a lo largo del camino observado, se obtiene un valor medio de la velocidad. Este mismo proceso se repite para diferentes valores de la presión hidrostática obteniendo así la respuesta en velocidad para cada presión.

14.3 Viscosidad de fluidos Newtonianos

La primera etapa de la investigación se concentró en el diseño de los microcanales y el estudio de flujos de agua en su interior a modo de caracterización. Se realizaron experimentos con canales de diferentes alturas y largos estudiando su posición con respecto al tiempo. Se obtuvo que para canales de alturas superiores a $b = 150\,\mu m$ el exponente de la ley de potencias de la posición del frente promedio con respecto al tiempo es $\nu \approx 1$. Este valor indica que la velocidad del frente de agua se mantiene constante a lo largo de todo el canal, ver figuras 5.1 y 5.5.

Obteniendo el valor de la velocidad del frente de agua para diferentes presiones hidrostáticas podemos establecer un relación entre la presión efectiva en la entrada del microcanal y la velocidad del fluido dentro de éste. La relación obtenida es lineal lo que indica que el fluido estudiado es Newtoniano, es decir, su viscosidad es constante y no depende del ritmo de cizalla entre sus capas, ver figura 5.10.

Como se esperaba el agua es un fluido Newtoniano y hemos sido capaces de corroborar su comportamiento como tal para diversos canales. El siguiente paso es obtener un valor de su viscosidad adecuado. Tomando en consideración la geometría del sistema acoplado (reservorio, tubo y microcanal) obtuvimos para distintos canales que la viscosidad del agua es $\eta = 1.02 \pm 0.02\, cP$ que coincide muy bien con el valor bibliográfico conocido de $\eta_{agua} = 1\, cP$ a temperatura ambiente. Uno de nuestros resultados más relevantes consiste en que al usar canales de distintas alturas podemos extender el rango de ritmos de cizalla conseguidos para la caracterización del frente de fluido, manteniendo inalterado el valor de su viscosidad, ver figura 5.17.

Con estos resultados ya tenemos un viscosímetro de agua, el que ahora debe ser extendido a otros fluidos también Newtonianos. Utilizamos en este caso 3 fluidos Newtonianos viscosos: etilenglicol, glicerina y plasma sanguíneo. El primer paso consistió en verificar que para estos fluidos la velocidad del frente también se mantiene constante a lo largo del microcanal, ver figura 6.1. Ya que el sistema para otros fluido Newtonianos se comporta igual que para el agua, utilizando la misma metodología logramos obtener la viscosidad de estos fluidos con un error no superior al 5%, ver figura 6.7. Incluso, se logró obtener la viscosidad del plasma sanguíneo de diferentes donantes sin observar solapamiento entre sus valores, ver figura 6.8. Los valores de viscosidad obtenidos con nuestro viscosímetro para fluidos Newtonianos se muestra en la tabla 14.1.

Fluido	Micro-dispositivo	Reometro	bibliog.
Agua	1.02 ± 0.02		1
Etilenglicol 44%	3.517 ± 0.009	3.3	3.2
Glicerina 19%	1.96 ± 0.03	1.93	2.01
Plasma sanguíneo A	1.716 ± 0.01	1.84	1.81
Plasma sanguíneo B	1.55 ± 0.02		1.81

Table 14.1: *La tabla muestra diferentes valores de la viscosidad de los fluidos medidos con diferentes métodos y aparatos*

Debido a una modificación en la configuración del experimento al realizar las medidas con sangre, se estudió el comportamiento de fluidos Newtonianos dentro del canal considerando 2 fluidos distintos moviéndose dentro del tubo que conecta el depósito con el microcanal. Se observó que al poner 2 fluidos con la misma densidad pero diferente viscosidad el comportamiento constante de la velocidad se veía alterado generando una pequeña aceleración en el fluido dentro del canal, ver figura 7.2. Dado que el sistema con velocidad constante no se conserva, para determinar la viscosidad del fluido dentro del canal se desarrolló una teoría para 2 fluidos inmiscibles. Por medio de esta nueva teoría se obtuvo la viscosidad del agua y del etilenglicol al 40% en función de la presión hidrostática ejercida sobre el fluido en el depósito, ver figura 7.3.

14.4 Viscosidad de la sangre

La sangre no es un fluido sencillo de estudiar ni manipular. Está formada por distintas fases: plasma y fracción celular. El plasma sanguíneo está compuesto principalmente de agua ($\approx 92\%$) y de diversas proteínas. La fracción celular está compuesta principalmente por eritrocitos o glóbulos rojos además de leucocitos o glóbulos blancos y plaquetas. De forma general la sangre tiene propiedades no Newtonianas y presenta un comportamiento pseudoplástico, es decir, que su viscosidad disminuye al aumentar el ritmo de cizalla del fluido, ver figura 3.4. Esta propiedades no Newtonianas vienen dadas tanto por las proteínas que se encuentran en el plasma como por las características especiales de sus células rojas.

A nivel macroscópico la viscosidad de la sangre tiene una dependencia directa con el hematocrito (concentración de eritrocitos de una muestra), es decir, que si disminuye el hematocrito disminuye también su viscosidad. Una forma alternativa de describir este comportamiento es relacionar el hematocrito con la velocidad del frente de fluido, así al aumentar el procentaje de hematocrito disminuye la velocidad del frente, ver figura 8.6.

Para obtener la viscosidad de la sangre, estudiamos su respuesta en el microcanal mediante 3 modelos de viscosidad no-Newtonianos distintos. El modelo de Ley de Potencia, el método de Weissenber-Rabinowitch-Mooney y un modelo en el que el shear rate depende del exponente de la viscosidad. Hemos podido corroborar con estos modelos el comportamiento no-Newtoniano y shear thinning de la sangre para diversas muestras sanas y enfermas, ver figuras 9.4, 9.8 y 9.10.

14.5 Viscosidad y Glóbulos rojos

De manera de poder establecer un relación entre la viscosidad de la sangre y las propiedades de sus células rojas hemos desarrollado dos modelos de escalamiento cada uno correspondiente a una característica particular. En primer lugar estudiamos la relación entre la viscosidad de la sangre y la agregación de sus células rojas. Luego estudiamos la relación entre la viscosidad de la sangre y la elasticidad de la membrana celular de sus eritrocitos.

En ambos casos antes de proceder al proceso de escalamiento se llevó a cabo un proceso de normalización con respecto al hematocrito para descartar así que las diferencia en el valor de la viscosidad estuvieran definidas por la concentración de sus glóbulos rojos. La ecuación de normalización está dada como:

$$\eta_{norm} = \frac{1}{\phi^{1/3}} \frac{\eta(\dot{\gamma})}{\eta_0} \tag{14.1}$$

14.5.1 Agregación

Primero desarrollamos un modelo de escalamiento que relaciona la viscosidad de una muestra de sangre a distintos días desde su extracción comparando el nivel de agregación de sus células rojas. Para esto definimos una número capilar adimensional C_a, como:

$$C_a = \frac{\eta_0 a^3}{D_e} \dot{\gamma}_F \tag{14.2}$$

Esta cantidad está basada en un modelo de agregación usando un Potencial de Morse, dónde $D_e = 200 \times 10^{-22}\, J$ corresponde a la altura del pozo de potencial, η_0 es la viscosidad del plasma sangüineo y $a \approx 7.8\, \mu m$ el tamaño medio de una célula roja. En este caso hemos podido establecer que al expresar la viscosidad en función de este número las curvas de viscosidad correspondientes a las muestras de ambos días colapsan, ver figura **??**. Este resultado indica que el aumento de la viscosidad de la sangre ”vieja” viene dado sólo por la reducción de la distancia de sus células al agregarse. En otras palabras, al colapsar ambas curvas hemos comprobado que es la agregación lo que genera el aumento de viscosidad de la muestra.

14.5.2 Coeficiente de elasticidad

Por otro lado, hemos definido un sistema de escalamiento relacionado con la elasticidad de la membrana celular. En este caso también hemos definido un número capilar, C_κ, pero esta vez relacionado con el coeficiente de elasticidad de la membrana:

$$C_\kappa = \frac{\eta_0 a^2 \dot{h}}{\kappa} \left(\frac{a}{b}\right) \tag{14.3}$$

Aquí η_0 es la viscosidad del plasma de la muestra, $a \approx 7.8\mu m$ es el diámetro del célula, $\dot{h}$ es la velocidad media del frente, b la altura del microcanal y κ el coeficiente de elasticidad. Hemos comparado sangre sana con sangre anémica considerando que el coeficiente de elasticidad de la membrana celular de una células sanas tiene un valor aproximado de $\kappa \approx 50 k_B T = 2 \times 10^{-19}\, (J)$. Nuevamente escribiendo la viscosidad en función del número capilar se observa un colapso entre las curvas de viscosidad. Este colapso demuestra que la diferencia en viscosidad de ambas sangres (sana y anémica) puede ser descrita en función de las características de la flexibilidad de la membrana celular de sus glóbulos rojos, ver figura 10.3.

14.6 Conclusiones

Las conclusiones generales y nuestros resultados de la tesis pueden separarse en dos partes. Una parte dedicada al trabajo con fluidos Newtonianos y una parte dedicada al trabajo con sangre. Para la primera parte de esta tesis nuestros principales resultados son:

- Hemos sido capaces de controlar la velocidad del frente de fluido dentro del microcanal de manera que permanezca constante, para canales de diferentes alturas.

- El rango del ritmo de cizalla puede extenderse cambiando la geometría (altura) del microcanal.

- Usando nuestro dispositivo y método hemos calculado la viscosidad de 4 fluidos Newtonianos distintos en función de su ritmo de cizalla con una presición de menos del 10%. Además para bajos ritmos de cizalla nuestros resultados son mejores que los testeados en un viscosimetro convencional.

- Para un sistema de dos fluidos de diferentes visosidades, el método puede adecuarse y aún así obtener resultado fiables de la viscosidad de los fluidos dentro de microcanal.

De la segunda parte de esta tesis nuestros principales resultados se nombran a continuación:

- Hemos sido capaces de relacionar la viscosidad de la sangre con su hematocrito para diferentes muestras.

- Usando tres modelos no-Newtonianos diferentes, hemos descrito el comportamiento no-Newtoniano y pseudoplástico de la sangre para diferentes muestras, sanas y enfermas.

- Hemos obtenido valores confiables de la viscosidad de la sangre, comparados con estudios previos de ella.

- Establecimos una relación entre la viscosidad de una muestra de sangre con su nivel de agregación, basado en el tiempo desde la extracción de la muestra.

- Establecimos una relación entre la viscosidad de una muestras de sangre con el coeficiente de deformación de la membrana de sus células rojas.

- De estos dos último puntos lo más relevante es que hemos sido capaces de entender y cuantificar propiedades de las células rojas, estudiando la sangre como un fluido continuo.

Appendix

Microchannels Fabrication

The fabrication of microdevices process is separated in 3 big stages. The first stage of the fabrication is the design of the mask. The second stage is the fabrication of the master which has the printed relief of the mould on it using photolithography. The third and final stage is the replica moulding method. The last two stages are perform on a Clean Room which secures that the microchannel won't be contaminated with dust and particles, which may altered the design features.

A.1 Design of the mask

The masks are drawn using Macromedia Free Hand MX software, other softwares as AutoCAD may be also used. Figure A.1 shows an image of the interface of the program with the building design. Since we will use a negative photoresist to fabricate the master, the transparent parts of the design mask will allow the penetration of light to polimerize the exposed resist. A final image of the mask is shown in figure A.2 which is printed in an acetate sheet using a high resolution printer.

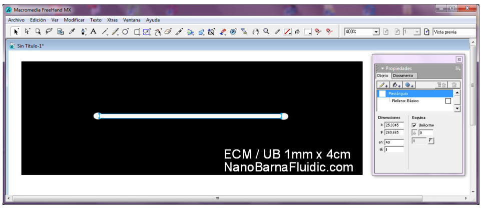

x: 25,0345
y: 260,665
an: 40
al: 1
☑ Uniforme
0

Figure A.1: *Interface of the Macromedia Freehand Software to design the mask.*

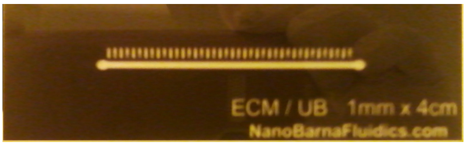

Figure A.2: *Image of the acetate mask used to fabricate the master.*

A.2 Master Fabrication with Photolithography

Conventional photolithography is a classic technique for patterning structures with feature size larger than 1 μm. The exposure of polymeric photosensitive material to UV radiation introduces a latent image into the material due to a set of chemical changes in its molecular structure. In our case, exposure is patterned interposing the acetate mask between the source of radiation and the photoresist material.

The polymeric photoresist may come as an aqueous solution as SU-8 2000 (MicroChem Inc.) or as a dry film, Ordyl SY300 (Elga Europe), TMMF S2000 (Tokyo Ohka Kogyo Co.). We have fabricated using both kind of polymeric resist, aqueous SU-8 2150 and SU-8 2010 and dry film Ordyl SY355. The processes performed with each photoresist are explained in the following subsections.

A.2.1 Cleaning of the substrates

One of the most important parts of the microchannel fabrication is cleaning the substrates which is common for both used photoresist. The resists are compatible with many substrates but we have used glass slides of $75 \times 25\,mm^2$, which are cheap to come by and easily cleaned with organic solvents.

The glass substrates are first scraped with a tissue soaked in acetone and then rinsed with de-ionized water. Later, an ultrasound wash is performed with DI water for $60\,s$, ethanol for $120\,s$ and again with DI water for $60\,s$. After the sonication wash, each glass slide is sprayed with ethanol, rinsed with ID water and dried with nitrogen. To eliminate humidity from the substrate we place it over a hot plate at 100°C for 5 minutes. Finally the clean substrates are submitted to an oxygen plasma sweep for 30 minutes [Rodríguez Villarreal, 2011].

A.2.2 SU-8 2000

The SU-8 2000 is a high contrast permanent epoxy based photoresist widely used by MEMS producers for many years. It has a high coating quality, excellent imaging characteristic and is capable of producing very high aspect ratio structures. Its optical transmission above $360\,nm$ makes it ideally suited for imaging near vertical side walls in very thick films. It is also very suitable for permanent applications. It can be found in different viscosities depending on the desired film thicknesses. The normal processing with SU-8 2000 photoresist consist of five basic steps:

1. Spin Coal
2. Soft Bake
3. Exposure
4. Post Exposure Bake
5. Develop

In some cases a Hard Bake procedure is performed after the fifth step.

A.2.2.1 Spin Coat

First we place the substrate on a spinning plate and then we poured the resin over it, $1\,ml$ for every $25\,mm$ of substrate diameter. Once the resist is poured and homogeneously distributed along the substrate we set a spinning process consisting on 2 steps.

An initial spin at 500 rpm with an acceleration of 100 rpm/s from 5 to 10 seconds. A second spin takes place at the proper rpm at an acceleration of 300 rpm for 30 second. The spinning process is aim to eliminate the excesses of resist in order to obtain an homogeneous layer with the desired height. The spin conditions to achieve a desired film thickness depends on the viscosity of the SU-8 resist. The appropriate spin coal revolutions per minute are shown in table A.1. To fabricate channels of 50 μm we performed the whole process 5 times for a 10 μm resist layer.

SU-8 Resist	Film Thickness	Step	rpm	rpm/s	time
		0	500	100	7 s
SU-8 2010	10 μm	1	3000	300	30 s
SU-8 2150	200 μm	1	3500	300	30 s
SU-8 2150	300 μm	1	2500	300	30 s
SU-8 2150	500 μm	1	1100	300	30 s

Table A.1: *Spin Coat Revolutions per minute and Time Table*

A.2.2.2 Pre and Soft Bake

After the spin coal process is finished, the obtained wafer is placed over a hot plate at $65°C$ from 5 to 10 minutes to provide an adequate evolution of the solvent. Then the temperature is raised at $95°C$ for the resist to cure and harden. The time of Soft Bake depends on the desired film thickness and the SU-8 viscosity. The appropriate times of Pre and Soft Bake are shown in Table A.2, this times may vary depending on the environmental conditions of the Clean Room (temperature, humidity).

To check that the resist is ready for the next step, the wafer is put away from the heat and let to cool for a few minutes. With a hard object we press over the wafer's edges in search for "wrinkles" in the resist, when "wrinkles" are no longer seen the soft bake process is finished. Otherwise the wafer is placed again over the hot plate until it is ready.

Film Thickness μm	Pre Bake Time $minutes$ 65°C	Soft Bake Time $minutes$ 95° C
10-20	4	15-20
100-150	5	20-30
160-225	5-7	30-45
230-270	7 1	45-60
280-550	7-10	60-120

Table A.2: *Pre bake and Soft bake times*

A.2.2.3 Exposure

The exposure process is the one at which the negative photoresist polimerizes when exposed to UV light. The mask, with the printed design, is set over the wafer and the ensemble is set over an aligner. Then the master is illuminated with UV light for 20 to 60 second depending on the height of the channel required. Table A.3 shows the energy values needed to obtained the expected channel height. During the exposure the photo-acid generator from the resist absorbs photons in the area of the SU-8 that is exposed to UV light, which produces a strong acid that acts as a catalyst in the Post Exposure Bake step.

Film Thickness μm	Exposure Energy mJ/cm^2
100-150	240-260
160-225	260-350
230-270	350-370
280-550	370-600

Table A.3: *UV light exposure energy*

It is important to clean the mask before exposure to avoid stains that may interfere with the master's pattern. This is made using Ethanol, rinsed with DI water and dried with nitrogen.

A.2.2.4 Post Exposure Bake

This is a process that has to take place directly after exposition to act as a catalyst for the polimerized master. The PEB times are shown in table A.4 according to the height of the master. While the exposed wafer is submitted to heat the image of the polimerized resist becomes clear.

Film Thickness μm	PEB Time $minutes$ 65°C	PEB Time $minutes$ 95° C
100-150	5	10-12
160-225	5	12-15
230-270	5	15-20
280-550	5	20-30

Table A.4: *Post Exposure Bake times*

A.2.2.5 Development

The develop is a delicate process perform as a chemical etching to the polimerized wafer. After the post-exposure bake, the wafer is immerse in a chemical solution, the SU-8 developer (1-Methoxy-2-Propanol Acetate), which dissolves all the unexposed resist leaving the relief of the mask printed on the substrate.

If we are working with low resist heights, instead of immersion is recommended to perform a repeated soft bath with the developer using a pipette until the relief is clear. This is to avoid that the relief peels off from the substrate. Table A.5 shows the suggested times of the immersion of the wafer in the developer. These times may vary depending on environmental and exposure conditions.

Film Thickness μm	Develop Time $minutes$
100-150	10-15
160-225	15-17
230-270	17-20
280-550	20-30

Table A.5: *Immersion times on the SU-8 developer solution*

A.2.2.6 Rinse and Dry

Once the relief appears on the substrate and all the excesses of unexposed resist have dissolved, the master is sprayed and washed with fresh solution. To stop the reaction, the developed master is sprayed with isopropyl alcohol and later dried with nitrogen. To ensure the developed image attachment to the substrate, the master is place in an oven at $150°C$ for 30-60 minutes.

A.2.3 Ordyl SY300

Ordyl SY300 is a solvent type permanent dry film for MEMS applications from Elga Europe. It has high resolution, great heat and chemical resistance and high dimension stability. It is a biocompatible material and guarantee good adhesion to glass surfaces [ElgaEurope, 2012]. The procedure to generate the master using this type of photoresist is simpler than the one with SU-8 2000. There is no need of the Pre, Soft and Post Exposure Bake steps which speeds up the whole fabrication process, especially when working with high heights. Another advantage of this resist over the aqueous one is the height homogeneity of the structure which does not overcome $5\,\mu m$.

The Ordyl SY355 resist is a sheet roll of $300\,mm$ width which is cut in smaller sheets of $80 \times 30\,mm^2$, enough to cover the glass substrate. Each sheet is composed by 3 layers: a polyester layer, a microlithographic polymer layer, with an effective thickness of $55\mu m$, and a polyethylene layer as shown in figure A.3.

Before start the coating process, it is important to cut enough Ordyl sheets to achieved the wanted height of the channel, adding $55\mu m$ layers.

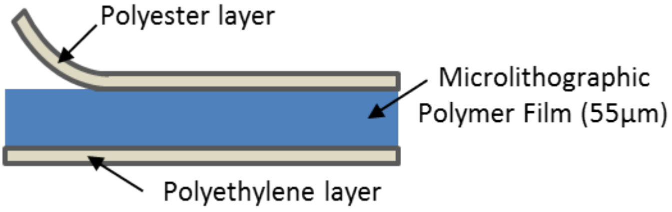

Figure A.3: *Representation of the Ordyl Sheet Structure.*

A.2.3.1 Coating and Lamination

Before lamination of the dry-film photoresist, the protective polyethylene layer is peeled off and the dry-film is carefully attached to the glass substrate. Then the photoresist attached to the substrate is laminated using a hot laminator at a temperature between $65 - 85°C$, figure A.4. The main objective of the lamination step is to provide intimate contact between the polymer and the substrate, ensuring the polymer flows into the surface roughness maximizing it adhesion. It is important to ensure that no bubbles or creases are present on the surface of the substrate after passing through the laminator, since these may affect the master's features.

After lamination, if we need to add more layers to the substrate (to increase the height of the final master) the second protective layer is peeled off from the wafer which is submitted to a plasma sweep for 10 second before the new sheet of Ordyl is attached to it. The lamination and Plasma Cleaning processes are repeated as many times as the wanted height of the master requires. If no more layer are needed, we allow the obtained wafer to cool down to room temperature prior to further processing.

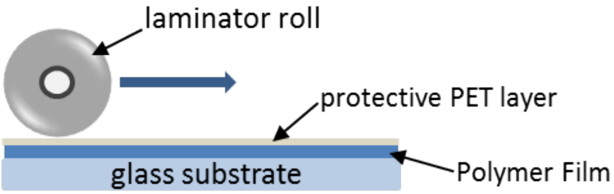

Figure A.4: *Representation of the hot lamination process.*

A.2.3.2 Exposure

The mask is set over the resist where the protective PET layer has been removed to avoid scattering and deflection of light which may result in inhomogeneous side walls

[Vulto et al., 2005], improving the definition on the edges of the relief. An exposure energy of $150\,mJ\,cm^2$ for 30 to $60\,s$ is recommended, exposition times may vary according to the number of layers used in the master.

Even though we have tested that with Ordyl SY355 a PEB is not essential, a 5 minutes Post Bake at $85°C$ might be useful to improve the definition of the structures [Wangler et al., 2011].

A.2.3.3 Develope

The developing process is performed using the Ordyl SY300 Developer. With Ordyl, sometimes immersion is not enough to eliminate the unexposed resist and agitation using ultrasonic frequencies is useful to achieve better definition on the edges of the relief. Once all the excesses of resist are removed we use the Ordyl SY300 Rinse to remove scum and clean the surface. If a final rinse with DI water is performed, is necessary an intermediate rinse with IPA solution. SU-8 developer solution may also be used to develop the Ordyl SY300 resist.

A.2.3.4 Post Bake

After developing is necessary an oven post-baking at $150°C$ for 30 to 60 minutes, to transform the resist into a rigid structure. Figure A.5 shows picture of a final master of Ordyl.

Figure A.5: *Image of a final master of Ordyl.*

A.3 Replica Moulding and Softlithography

The replica moulding technique, for microfluidics devices fabrication, is largely used due to its simplicity and low costs. It consist of transferring the pattern from a master to a polymeric material cast [Xia et al., 1997]. One of biggest advantages of this technique is that many copies or replicas of a mould may be reproduced using the same master, therefore its name.

Poly(dimethylsiloxane), commonly known as PDMS, has been one of the most used polymers for microfluidics in the latest decade, especially in biological applications. Fabrication with this polymer is easy and accurate since it may be cast against a suitable mould with less than $0.1\,\mu m$ error [McDonald and Whitesides, 2002].

PDMS has many other properties which makes it very suitable for our research. It is cheap and commercially available, non-toxic, easy to manipulate, optically transparent, it is hydrophobic (with a water contact angle $\approx 110^o$) but it may be modified to become hydrophilic, its elastomeric character allows it to conform to a surface at an atomic level contact and it can seal reversibly or, after oxidation, irreversibly to different types of substrates [Qin et al., 2010].

A.3.1 PDMS preparation

The PDMS, Sylgard 184 from Down Corning (distributed in Spain by Ellsworth Adhesives), is supplied in two components: a base and a curing agent. Mixing both parts on a 10:1 weight ratio of base:curing agent a cross-linked elastomeric solid is formed. The mixing process creates bubbles on the resulting mixture which are extracted using a vacuum pump.

When all bubbles are removed, the liquid pre-polymer PDMS is poured over the master (or several masters) inserted on a petri dish. Here the PDMS spreads through the dish covering the master and conforms to the shape of the pattern replicating the features of its design with high fidelity. Once the whole dish is covered, the height of the PDMS mixture over the master substrate must be ideally from 3 to $7\,mm$. For a petri dish of $12 \times 12\,cm^2$ and five masters, a mix of $30\,g$ is adequate. The petri dish is set into the vacuum pump to eliminate all the bubbles that may have been generated on the PDMS during its pouring, since they may affect the cast pattern. Once no more bubbles are seen the PDMS is set to cure in an oven at $65°C$ for 90-120 minutes until it solidifies.

If some prepared mix of PDMS is not used it may be maintain on a freezer at -18^{o}C to avoid solidification. The mixture is preserves in this conditions around 3 weeks.

A.3.2 Pattern moulding and Sealing

After curing, the PDMS is cut with a scalpel surrounding the channel and then it is carefully peeled from the master, figure A.6. Using a Harris Micro-Punch of $0.75\,mm$ diameter the PDMS cast is perforated at the extremes of the printed channel to set the inlets and outlets of the channel.

The PDMS replica is set (facing up) with a clean glass substrate in the Oxygen Plasma Cleaner for 10 seconds. This way a molecular sweep occurs in both surfaces. Placing the side of the patterned PDMS over the glass substrate these are irreversible sealed at contact by means of a molecular bonding.

Finally we place the obtained device in the oven at 60^{o}C for 10 minutes to strengthen the adhesive seal.

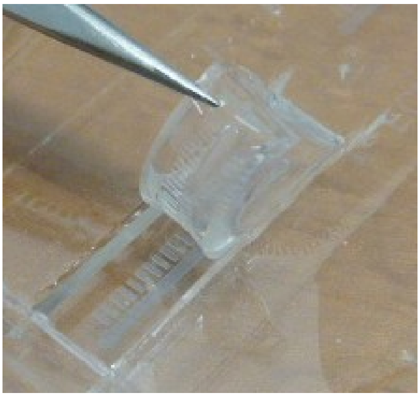

Figure A.6: *Image of the peeling process of PDMS from the master. We may appreciate the printed structure from the master on the PDMS.*

APPENDIX B

Microdevice Cleaning and Blood Protocols

B.1 Microchannel Cleaning

It is important to take good care of our microchannels and be aware of the effects that a measure may cause on them. An unavoidable consequence of a measure is wetting.

Normal wetting conditions of the microchannel is shown in figure B.1a. In this case, we may appreciate a well defined curvature of the fluid-air interface which it importance is explained in section5.1.3. After the fluid fills the microchannel, it must be removed and this leaves a wet layer on the channel walls, see figure B.1b. This layer changes the wetting properties of the channel which would altered the results from previous measures.

This implies that the microchannels must we dried after each measure. This is made pumping air inside the channel with a syringe and heating the glass surface of the microchannel to evaporate the micro-drops of water on it surface. Since surface tension is a temperature dependent quantity, C.2, the channel need to be cooled to room temperature before performing the next measure. Figure B.1c, shown the curvature change on the fluid interface due to high temperature.

When a fluid different that water is used in the microchannel (ethylene-glycol or glycerol) a rinse with water is needed after the fluid is removed from the channel. With biological sample (Blood Plasma, Blood) a more thorough cleaning must be perform an will be explained in the following section.

B.2 Blood Protocols

Ideally a channel after a measure with blood should be disposed, since we don't have an infinite stock of microchannel and we need to keep the conditions of it and the setup unaltered as much as possible we reused microchannel. These microchannels require a more demand cleaning that a channel used with non-biological samples.

Cleaning protocol for biological sample consist in several washes with different substance and solvent. First a deep rinse with water is performed in order to eliminate all the rest of sample from the channel. Next a wash with Oxygenated Water (H_2O_2) is perform to eliminate the residues of cells that may stay inside the channel. After the H_2O_2 again a rinse with water is perform to eliminate dead cells. Finally a rinse with ethanol or isopropyl alcohol is perform to disinfect the channel and avoid the growing of bacteria. Last the channel is dried with air and heat to evaporate the droplets let on the glass surface. Before using it again it is left to cool down at room temperature.

The tube and the container are also rinse with water and H_2O_2 and again with water to eliminate dead cells that may obstruct the bottom of the deposit or the tube, altering further measures.

All the cleaning process and preparation of samples take place under a vend hood to avoid contamination of the samples and of the environment. After all the measures are finish the vent hood and all surfaces and apparatus used to perform the measures are clean with water and H_2O_2 and finally disinfect with ethanol.

The residues are correctly disposed in the proper biological deposit of residues, facilitated by the Facultat de Física of the Universitat de Barcelona.

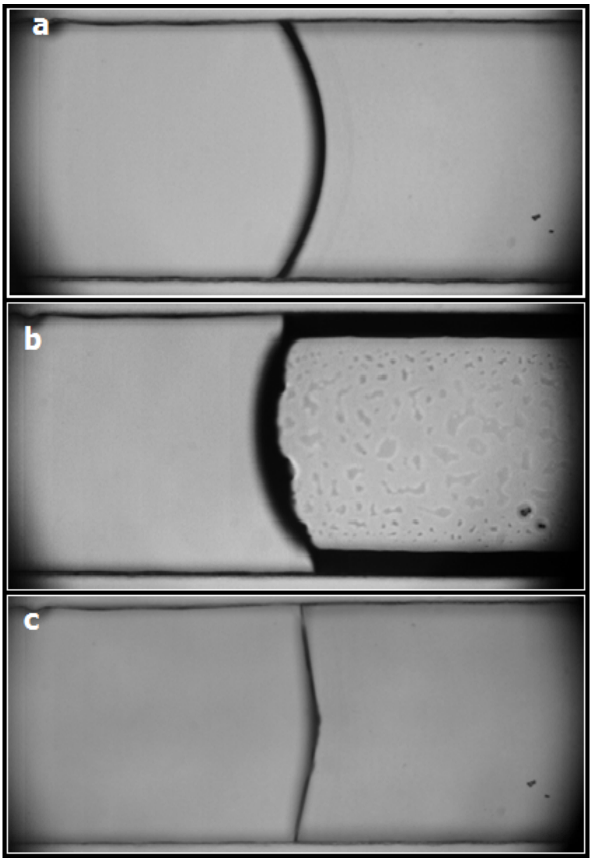

Figure B.1: *Real time images of the front moving inside the same microchannel with different wetting conditions. a) Normal wetting conditions of the dry channel. b) Wet channel without drying. c) Wetting conditions of dry channel at high temperature.*

Fluids Properties

C.1 Density

Fluid	*Temperature* $^{\circ}C$	*Density* $\rho\ \left(\frac{kg}{m^3}\right)$
Water	20	1000
Water	37	996
Ethylene glycol	20	1113
Ethylene glycol 44%	20	1050
Ethylene glycol 40%	20	1046
Glycerol	20	1259
Glycerol 19%	20	1049
Glycerol 14%	20	1036
Glycerol 10%	20	1026
Blood Plasma	20	1030
Blood Plasma	37	1025
Blood 45% HTC	20	1050-1060
Blood 45% HTC	37	1050
Blood 22% HTC	20	1035-1040
Blood 22% HTC	37	1035-1040
Red Blood Cells		1196

C.2 Surface Tension

Water Surface Tension:

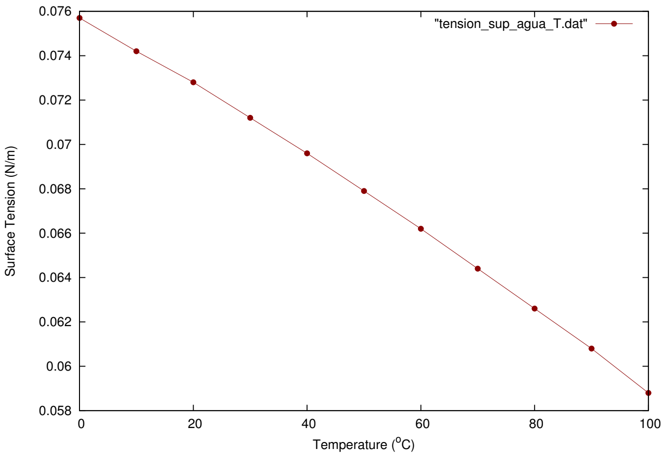

Figure C.1: *Surface Tension v/s Temperature for a water-air interface. Our experiment were performed at room temperature varying from 20 to 25 $^\circ C$. These values were extract from http://www.engineeringtoolbox.com.*

Fluid	*Temperature* $^\circ C$	*Surface Tension* $\tau \left(\frac{N}{m}\right)$
Water	15	0.0735
Water	20	0.0729
Water	25	0.0719
Ethylene-glycol	20	0.0477
Glycerol	20	0.0641

Table C.1: *Surface Tension for the used fluids. Reference taken from [Bruus, 2008] and [Engineering Toolbox, 2011].*

Plasma Surface Tension:

$$\tau_{T^\circ} = (-0.368 * T^\circ + 66.072) \times 10^{-}3 \, [N/m] \tag{C.1}$$

Whole Blood Surface Tension:

$$\tau_{T^\circ} = (-0.473 * T^\circ + 70.105) \times 10^{-}3 \, [N/m] \tag{C.2}$$

C.2.1 Contact angles of water

Fluid-Solid	Contact angle θ	*References*
Water-Glass	25°	[Bruus, 2008]
Water-PDMS	110°	[Qin et al., 2010]
Water-PDMS/HEMA	40°	[Bodas and Khan-Malek, 2006]
Water-PET	78°	[da Rosa et al., 2011]

Table C.2: *Contact angles between water and some solids at* $20°C$.

C.3 Viscosity

Fluid	*Temperature* $°C$	*Viscosity* $\eta\,(mPas)$	*References*
Water	0	1.787	[Bruus, 2008]
	20	1.002	[Bruus, 2008]
	37	0.691	[Bruus, 2008]
Ethylene-glycol 100%	20	19.14	[Engineering Toolbox, 2011]
Ethylene-glycol 40%	20	2.86	[Engineering Toolbox, 2011]
Ethylene-glycol 44%	20	3.34	[Engineering Toolbox, 2011]
Ethylene-glycol 25%	20	1.92	[Engineering Toolbox, 2011]
Glycerol 100%	20	1412	[Segur and Oberstar, 1951]
Glycerol 50%	20	6.00	[Segur and Oberstar, 1951]
Glycerol 20%	20	1.76	[Segur and Oberstar, 1951]
Glycerol 10%	20	1.31	[Segur and Oberstar, 1951]
Blood Plasma	20	1.810	[Baskurt, 2007]
	37	1.257	[Baskurt, 2007]
Whole Blood	37	39-48 ($0.277\,s^{-1}$)	[Baskurt, 2007]
	37	4.3-4.7 ($128.5\,s^{-1}$)	[Baskurt, 2007]
Blood 22% htc.	20		
	37	2.60 ($106\,s^{-1}$)	Thurston [1972]

APPENDIX D

Curvature of fluids inside the channel

In section 5.1.3 from chapter 5 I presented how the Laplace Pressure of a fluid inside a micro-channel is calculated using it curvature angle and we compared those results with the fitted results for the hydrostatic pressure. Here I show the curvatures for water in a channel with a gap $b = 100\,\mu m$ and the curvatures for plasma in a channel of $b = 300\,\mu m$ and whole blood in a channel of $b = 350\mu m$.

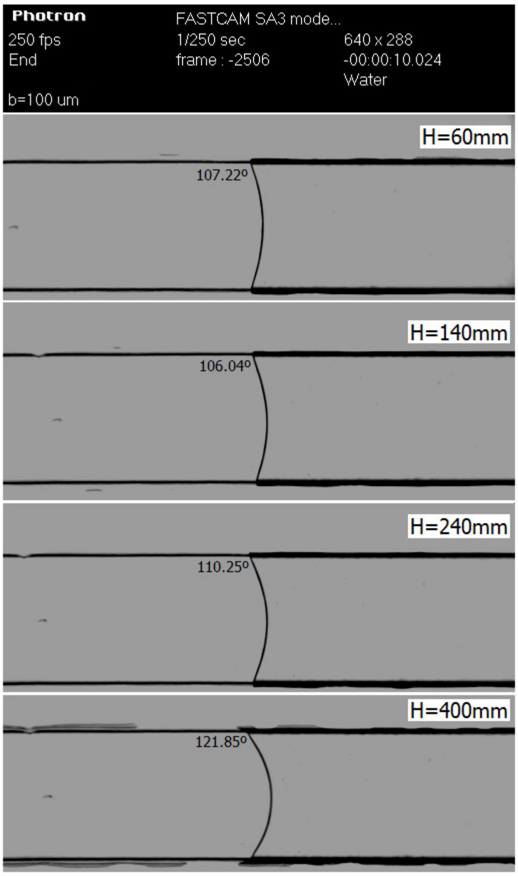

Figure D.1: *Curvature interface water-air in a channel of* $b = 100\,\mu m$. *We see that the curvature angle increases as the hydorstatic pressure increases. In channel of this depth the capillary forces become more important that in a channel of* $b = 300\,\mu m$*, section 5.1.3.*

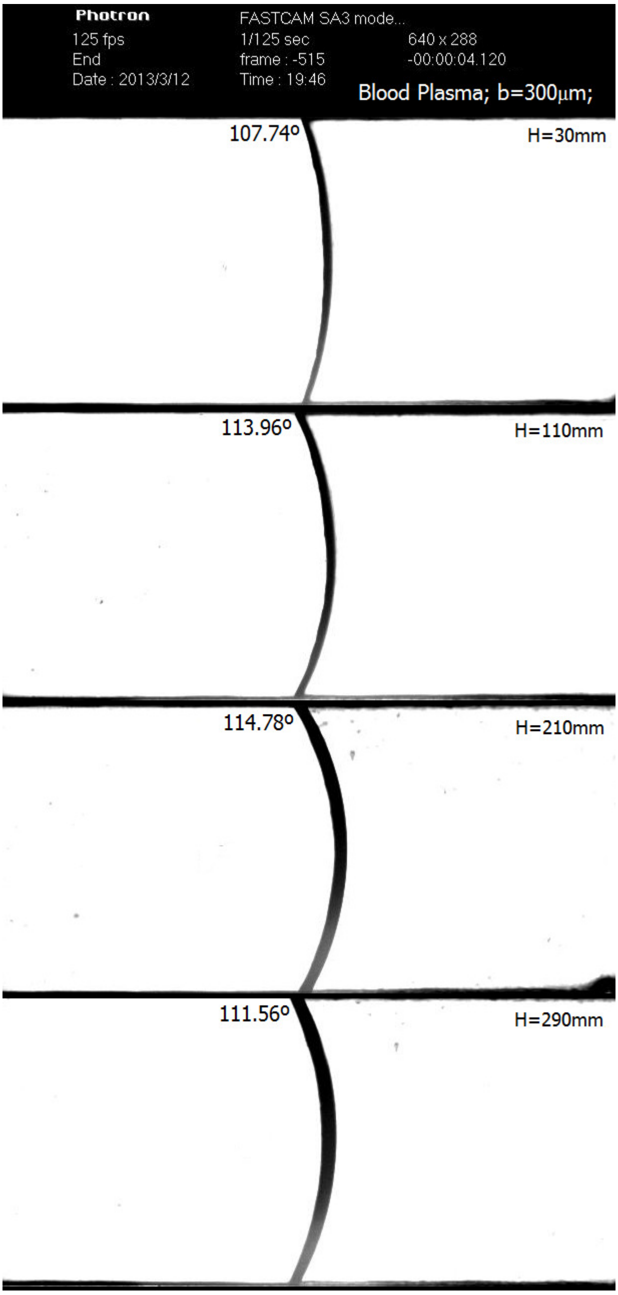

Figure D.2: *Curvature interface plasma-air in a channel of* $b = 300\,\mu m$. *We see that the curvature angle is almost constant at different hydrostatic pressures. The effect is also seen in water and ethylene-glycol for this micro-channel depth.*

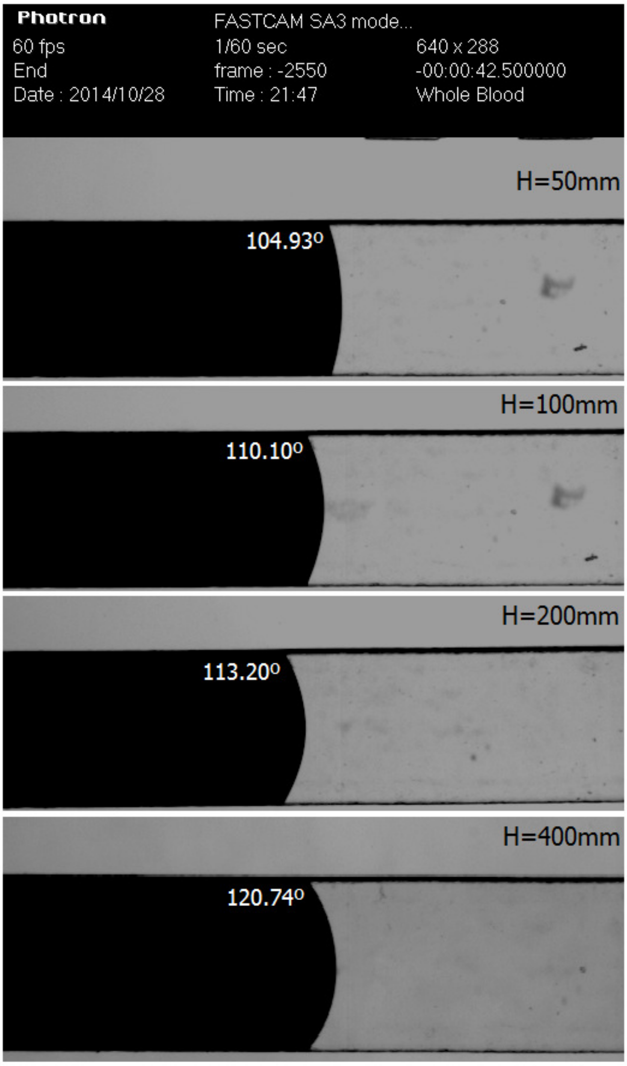

Figure D.3: *Curvature of the interface blood-air in a channel* $b = 350\,\mu m$*. In this case the curvature angle increases as the hydrostatic pressure, and the Laplace pressure is calculated for each curvature angle value.*

Microchannels Dimensions

E.1 Microchannels Dimensions

Channel Height $b\,(\mu m)$	Channel Height $b\,(mm)$	Cross Section $bw\,(mm^2)$	Hydraulic Diameter $D_h\,(mm)$
51 ± 5	0.051 ± 0.005	0.051 ± 0.005	0.097 ± 0.012
94 ± 6	0.094 ± 0.006	0.094 ± 0.006	0.172 ± 0.015
148 ± 2	0.148 ± 0.002	0.148 ± 0.003	0.258 ± 0.009
204 ± 9	0.204 ± 0.009	0.204 ± 0.011	0.338 ± 0.024
250 ± 3	0.250 ± 0.003	0.250 ± 0.005	0.400 ± 0.014
297 ± 5	0.297 ± 0.007	0.297 ± 0.009	0.458 ± 0.022
352 ± 6	0.352 ± 0.006	0.352 ± 0.009	0.521 ± 0.022

Table E.1: *Microchannels Cross section and Hydraulic Diameter. The cross section is calculated considering the width of the channel* $w = 1.00 \pm 0.01\,mm$*. The hydraulic diameter is calculated using the expression* $D_h = \frac{2bw}{b+w}$ *and it is usefull to compare with the blood vessels diameter.*

APPENDIX F

Images Analysis Code

The images were transformed and analized thought a computational code developed with Wolfram Mathematica©. The code is separated in different functions (subroutines) which are listed in the following sections.

F.1 Program Functions

F.1.1 Image processing function

Package Name:"PosicionPcte.m“

```
(*Function that process the image*)
procesaimagenvel[fondo_,frame_]:=(
(*image crop*)
fondo1=ImageCrop[fondo,{636,205},{Left,Top}];
frame1=ImageCrop[frame,{636,205},{Left,Top}];
fondo2=ImageCrop[fondo1,{636,100},{Right,Bottom}];
frame2=ImageCrop[frame1,{636,100},{Right,Bottom}];
(*contrast and brightness*)
fondo3=ImageAdjust[fondo2,{0,0.7}];
frame3=ImageAdjust[frame2,{0,0.7}];
(*image substraction*)
imresta=Image[(ImageData[fondo3]-ImageData[frame3])];
(*imresta1=ImageAdjust[imresta,{0,0}];*)
(*black and white*)
bin=Binarize[Image[imresta]];
matriz=ImageData[bin];
Return[matriz]
)
```

F.1.2 Position and Velocity of the mean interface functions

Package Name:"PosicionPcte.m“

```
(*Function that calculates the position of the mean front*)
posicion[matriz_]:=(
lpromf={};
Do[
 promf=N[Mean[Flatten[Position[matriz[[i]],1]]]];(*mean front in row i*)
 If[(Head[N[Mean[Flatten[Position[matriz[[i]],1]]]]]==Real),
   (lpromf=Append[lpromf,promf])];
,{i,1,Count[matriz,_]-1}];
(*mean front position*)
promc=N[Mean[lpromf]];
```

```
Return[promc]
)

(*Function that calculates the position of the blood front*)
posicionsangre[matriz_]:=(
lpromf={};
Do[
 promf=N[Mean[Flatten[Last[Position[matriz[[i]],1]]]]];(*mean front in row i*)
 If[(Head[N[Mean[Flatten[Position[matriz[[i]],1]]]]]==Real),
   (lpromf=Append[lpromf,promf])];
,{i,1,Count[matriz,_]-1}];
(*mean front position*)
promc=N[Mean[lpromf]];
Return[promc]
)

(*Function that calculates the velocity of the mean front*)
velocidad[pos_]:=(
suma1=N[fn/fps];
vinst={};vj={};
Do[
dpo=(pos[[j]]/(N[fn/fps]));
dp=(pos[[j]]-pos[[j-1]])/N[fn/fps];
If[j==1,vinst=Append[vinst,dpo],vinst=Append[vinst,dp]];
If[j==1,vj=Append[vj,{suma1,pos[[j]],dpo*pix}],vj=Append[vj,{suma1,pos[[j]],dp*pix}]];
suma1=suma1+N[fn/fps];
,{j,1,Count[pos,_]}];
Return[vinst]
)
(*vinst:instant velocity vector for each frame*)
(*vj:instant velocity array with respect to the position in pixels*)


(*Function that convert pixels/s in um/s*)
f[x_]:=x*pix;

(*Function that extract the velocity statistics*)
estadmedidas[velprom_,velpromum_,h_]:=(
mvelprom=Mean[velprom];
mvelpromum=Mean[velpromum];
sdvelprom=StandardDeviation[vinst];
sdvelpromum=StandardDeviation[vinstum];
epv=(sdvelpromum/mvelpromum)*100;
estadm=Append[estadm,{h,mvelprom,mvelpromum,sdvelprom,sdvelpromum,epv}];
Return[estadm];
```

F.1.3 Average of measures and statistical data acquisition functions

Package Name:"PromedioDatos.m“

```
ni=inicial_experiment
nf=final_experiment

(*Function that counts number of data*)
countdatos[s_,b_,h_,h1_,ni_,nf_]:=
(num={};
Do[
num=Append[num,Count[Import[StringJoin["vinstum_",ToString[s],"_4cm_1000x",ToString[b],
"um_H",ToString[h1],"mm_h",ToString[h],"mm_",ToString[i],".dat"]],_]];
,{i,ni,nf}];
tot=Min[num];
Return[tot];)
```

```
(*Function that averages the position and velocity for several experiments*)
velocidadpromedio[s_,b_,h_,h1_,fps_,fn_,ni_,nf_,tot_]:=(
sumat=N[fn/fps];
promvelocidad={}; (*time, mean velocities array*)
promposicion={}; (*time, mean positions array*)
tposvel={}; (*time, position, velocity array*)
pvaux={}; (*mean velocities auxiliar vector*)
Do[
pospromed={};(*position array j of the measurement i*)
velpromed={};(*velocity vector j of the measurement i*)
Do[
med=Import[StringJoin["vinstum_",ToString[s],"_4cm_1000x",ToString[b],"um_H",ToString[h1]
"mm_h",ToString[h],"mm_",ToString[i],".dat"]];
pmed=Import[StringJoin[ToString[s],"_4cm_1000x",ToString[b],"um_H",ToString[h1],
"mm_h",ToString[h],"mm_",ToString[i],".dat"]];
d=med[[j]];
dp=pmed[[j,2]];
pospromed=Append[pospromed,dp];
velpromed=Append[velpromed,d];
,{i,ni,nf}];

promvelocidad=Append[promvelocidad,{sumat,Mean[Flatten[velpromed]]}];
promposicion=Append[promposicion,{sumat,Mean[Flatten[pospromed]]}];
tposvel=Append[tposvel,{sumat,Mean[Flatten[pospromed]],Mean[Flatten[velpromed]]}];
pvaux=Append[pvaux,Mean[Flatten[velpromed]]];
sumat=sumat+N[fn/fps]; (*time*)
,{j,1,tot}];
Return[pvaux];)

(*Function that converts position values from pixel to um*)
posicionum[promposicion_,tposvel_]:=(
posi=promposicion;
positposvel=tposvel;
Do[
posi[[j,2]]=posi[[j,2]]*pix;
positposvel[[j,2]]=positposvel[[j,2]]*pix;
,{j,1,Count[posi,_]}];
fit=Fit[posi,{1,x},x];
vfit=First[fit[[2]]];
Return[posi];)

(*Function that eliminates all data outside 2SD*)
cortesd[pvaux_,promvelocidad_,positposvel_]:=(
var=Variance[pvaux];
sd=StandardDeviation[pvaux];
vmedia=Mean[pvaux];
vel={};vecvel={};tposvelprom={};
cmin=vmedia-2sd;
cmax=vmedia+2sd;
Do[
If[
pvaux[[i]]<=cmax&&pvaux[[i]]>=cmin,
vel=Append[vel,promvelocidad[[i]]]; (*cropped position, velocity array*)
vecvel=Append[vecvel,pvaux[[i]]];   (*cropped velocity vector*)
tposvelprom=Append[tposvelprom,positposvel[[i]]]; (*cropped time, position, velocity arra
]
,{i,1,Length[pvaux]}
];
Return[vecvel];)

(*Final Velocity*)
vfinal[vmediafinal_]:=(
```

```
vf=Mean[vmediafinal];
nd=Count[vmediafinal,_];
disp=(StandardDeviation[vmediafinal]/vf)*100;
Return[vf];)

(*Calculation of % dispersion*)
error[x_]:=(Abs[x-vf]/vf)*100;
```

F.2 Main Program

F.2.1 Data Extraction

```
SetDirectory["C:\\..."];
(*Import Packages*)
Import["PosicionPcte.m"];
Import["PromedioDatos.m"];

estadm = {{"#h(mm)", "v(pix/s)", "v(um/s)", "DevEst (pix)", "DevEst (um)", "e%"}};

velprom = {}; velpromum = {};
fi = inicial_frame; ff = final_frame;
pix = size of a pixel;
Do[
 (*Previous settings*)
 b = height of the channel; s = "name_of_fluid";
 h1 = height of the column; h = position on the channel;
 fps = frame rate; fn = number of frames;
 SetDirectory[
   StringJoin["C:\\...\\",ToString[s],"_1000x",
    ToString[b], "um_H", ToString[h1], "mm_h", ToString[h], "m_",
    ToString[n], "_"]];
 pos = {};
 posiciones = {};
 suma = N[fn/fps] (*time*);
  Do[
  (*Image Calling*)
  fondo = Import["fondo.png"];
  If[i < 10,
  frame = Import[
     StringJoin[ToString[s], "_4cm_1000x", ToString[b], "um_H",
      ToString[h1], "mm_h", ToString[h], "mm_", ToString[n], "_000",
      ToString[i], ".png"]],
   (If[i < 100,
     frame =
      Import[StringJoin[ToString[s], "_4cm_1000x", ToString[b],
        "um_H", ToString[h1], "mm_h", ToString[h], "mm_", ToString[n],
         "_00", ToString[i], ".png"]],
     (If[i < 1000,
       frame = Import[
         StringJoin[ToString[s], "_4cm_1000x", ToString[b], "um_H",
          ToString[h1], "mm_h", ToString[h], "mm_", ToString[n], "_0",
          ToString[i], ".png"]],
       frame =
        Import[StringJoin[ToString[s], "_4cm_1000x", ToString[b],
          "um_H", ToString[h1], "mm_h", ToString[h], "mm_",
          ToString[n], "_", ToString[i], ".png"]]
       ])
     ])
    ];

   (*Calling the function that process the image*)
```

```
   procesaimagenvel[fondo,frame];

   (*Calling the function of position*)
   posicion[matriz];
   pos = Append[pos, promc]; (*position vector in pixels*)
   posiciones = Append[posiciones, {suma, promc}]; (*time:position matrix*)
   suma = suma + N[fn/fps];(*time*)
 ,{i, fi, ff, 1}]

 (*Calling the function that calculates the velocity*)
 velocidad[pos];

 vinst = Delete[vinst,{1}];
 vj = Delete[vj,{1}]
 vinstum = Map[f, vinst];(*convert all elements in vinst into um/s*)
 promvinst = Mean[vinst];(*averaged instant velocities in pixel/s*)
 promvinstum =  Mean[vinstum];(*averaged instant velocities in um/s*)
 velfit = Fit[posiciones, {1, x}, x];(*linear fit for position v/s time*)
 velfitum = Map[f, velfit];
 velprom = Append[velprom, promvinst];
 velpromum = Append[velpromum, promvinstum];

 Export[StringJoin["plasma_4cm_1000x", ToString[b], "um_H",
   ToString[h1], "mm_h", ToString[h], "mm_", ToString[n], ".dat"],
  posiciones];
 Export[StringJoin["vinst_plasma_4cm_1000x", ToString[b], "um_H",
   ToString[h1], "mm_h", ToString[h], "mm_", ToString[n], ".dat"],
  vinst];
 Export[StringJoin["vinstum_plasma_4cm_1000x", ToString[b], "um_H",
   ToString[h1], "mm_h", ToString[h], "mm_", ToString[n], ".dat"],
  vinstum];
 Export[StringJoin["vj_plasma_4cm_1000x", ToString[b], "um_H",
   ToString[h1], "mm_h", ToString[h], "mm_", ToString[n], ".dat"], vj];

,{n,1,number of experiments}];
```

F.2.2 Position and mean velocity calculations

```
estad = {{"#h(mm)", "v(um/s)", "vfit", "Var", "DevEst", "v_sd (um/s)", "e%"}};

SetDirectory["C:\\..."];
b = 300; s = "a"; pix = 3.5;
fps = 500; fn = 10; h1 = 30; hi = 15; hf = 15;
ni = 2; nf = 5;

Do[
  (*Calculation of the mean value of positions and velocities for various experiments*)
  countdatos[s, b, h, h1, ni, nf];

  (*Calculation of the mean velocity*)
  velocidadpromedio[s, b, h, h1, fps, fn, ni, nf, tot];
  posicionum[promposicion, tposvel];

  (*Elimination of the dispersion*)
  cortesd[pvaux, promvelocidad, positposvel];

  (*Calculation of final velocity and dispersion*)
  vfinal[vecvel];
  Print["vmedia= ", vmedia];
  Print["vmediafinal=  ", vf];
  errorj = Map[error, vecvel];
  ep = Mean[jueee];
```

```
  Print["e%=  ", ep];

 estad = Append[estad, {h, vmedia, vfit, var, sd, vf, ep}];

 Export[StringJoin["estad_vel_", ToString[s], "_4cm_1000x", ToString[b],
   "um_H", ToString[h1], "mm.dat"], estad];
 Export[StringJoin["prom_vel_", ToString[s], "_4cm_1000x", ToString[b],
   "um_H", ToString[h1], "mm_h", ToString[h], "mm.dat"], promvelocidad];
 Export[StringJoin["prom_pos_um_", ToString[s], "_4cm_1000x", ToString[b],
   "um_H", ToString[h1], "mm_h", ToString[h], "mm.dat"], posi];
 Export[StringJoin["vec_promvel_", ToString[s], "_4cm_1000x", ToString[b],
   "um_H", ToString[h1], "mm_h", ToString[h], "mm.dat"], pvaux];
 Export[StringJoin["tposvelprom_", ToString[s], "_4cm_1000x", ToString[b],
   "um_H", ToString[h1], "mm_h", ToString[h], "mm.dat"], positposvel];
 Export[StringJoin["vec_promvel_", ToString[s], "_4cm_1000x", ToString[b],
   "um_H", ToString[h1], "mm_h", ToString[h], "mm_sd.dat"], vecvel];
 Export[StringJoin["prom_vel_", ToString[s], "_4cm_1000x", ToString[b],
   "um_H", ToString[h1], "mm_h", ToString[h], "mm_sd.dat"], vel];
 Export[StringJoin["tposvelprom_", ToString[s], "_4cm_1000x", ToString[b],
   "um_H", ToString[h1], "mm_h", ToString[h], "mm_sd.dat"], tposvelprom];
 , {h, hi, hf}]
```

F.3 Viscosity Calculations

F.3.1 Previous setting

```
s = "name_of_fluid"; hs = position; hc = canal height;
SetDirectory[
  "C:\\..."];

rt = 0.000127; lt = 0.43;(*Tube characteristics*)
b = hc*10^-6; w = 0.001; hm = hs*0.001; (*Canal characteristics*)
pg = 1000*9.8; (*Fluid Properties*)
d = N[(8*w*lt)/(Pi*rt^4)]; (*Tube term*)
ca = N[(12*hm)/(b^2)]; (*Canal term*)
(*S.I.*)

(*errors*)
z1 = N[ca*(0.000039/hm + 2*0.000010/b)];
z2 = N[d*(0.000010/b + 0.001/lt)];
z3 = N[pg*0.001 + 10];
z4 = N[z1 + z2];
```

F.3.2 Stress v/s Shear Rate: velocity profile

```
vecss = {}; vecsr = {}; vecssc = {}; velprom = {}; velpromm = {};
viscosr = {}; srer = {}; viser = {}; vecpgh = {};

Do[
  velocidad =
   Flatten[Import[
     StringJoin["vec_promvel_", ToString[s], "_4cm_1000x", ToString[212],
      "um_H", ToString[h1], "mm_h", ToString[hs], "mm.dat"]]];
  pgh = pg*(h1*10^-3); (*densidad et 40%: 1045.28 kg/m3*)
  vm = velocidad;
  Do[
   vm[[i]] = velocidad[[i]];
   vecssc =
    Append[vecssc, {N[(vm[[i]]*10^-6)/b], N[(pgh - pc)/(b^2*d)]}];(*SI*)
   viscosr =
```

```
    Append[viscosr, {N[(vm[[i]]*10^-6)/b],
      N[(pgh - pc)/(vm[[i]]*10^-6*((12*hm/b^2) + b*d))]}];
   , {i, 1, Count[velocidad, _]}];
  meanvm = Mean[vm];
  errorabs = StandardDeviation[vm];
  velprom =
   Append[velprom, {N[h1*10^-3], N[meanvm*(10^-6)], errorabs*(10^-6)}];
  vecpgh = Append[vecpgh, {N[meanvm*(10^-6)], N[pg*h1*10^-3]}];
  , {h1, 50, 290, 20}];
Print["velprom: ", velprom]
fit = Fit[vecpgh, {1, x}, x];
pc = fit[[1]];
m = First[fit[[2]]];
eta = N[m/(ca + d*b)];
Print["Pcap=", pc];
Print["Viscosidad=", eta];

(*Export[StringJoin["shear_stress_",ToString[s],"at_4cm_1000x350um_h",\
ToString[hs],"mm_ce.dat"],vecssc];*)
Export[StringJoin["V_vs_H_error_", ToString[s], "_4cm_1000x", ToString[hc],
   "um_h", ToString[hs], "mm.dat"], velprom];
Export[StringJoin["pgH_vs_V_", ToString[s], "_4cm_1000x", ToString[hc],
   "um_h", ToString[hs], "mm.dat"], vecpgh];

ListPlot[vecpgh, PlotRange -> {{0, 0.002}, {0, 4500}}]
```

F.3.3 Stress v/s Shear Rate and Viscosity v/s SR:mean velocities

```
velprom = Import[StringJoin["V_vs_H_",ToString[s],"_4cm_1000x",ToString[hc],"um.dat"]];
vecpgh = Import[StringJoin["pgH_vs_V_",ToString[s],"_4cm_1000x",ToString[hc],"um.dat"]];

(*General Viscosity for Newtonian Fluids*)
fit = Fit[vecpgh, {1, x}, x]
m = First[fit[[2]]];
pc = fit[[1]];
eta = N[m/(ca + d*b)];

(*Viscosty for each shear rate value*)
etavec = {}; sssrc = {}; viscoc = {}; error = {};

Do[
  hh = velprom[[i, 1]];
  v = velprom[[i, 2]];
  erv=velprom[[i,3]];(*velocity error*)
  ssc = N[(pg*hh - pc)/(ca + b^2*d)];
  sr = N[v/b];
  srer = N[sr*((erv/v) + (10^-6/b))]; (*shear rate error*)

  etac = N[ssc/sr];(*For newtonian fluids*)
  z5 = N[v*(ca + b*d)*(erv/v + z4/(ca + b*d))];(*viscosity error*)

  vis = N[(pg*hh - pc)/(v*(ca + b*d))];
  viser = N[vis*(z5/(v*(ca + b*d)) + z3/(pg*hh - pc))]; (*viscosity error*)
  viscoc = Append[viscoc, {sr, etac}];(*For newtonianos fluids*)
  sssrc = Append[sssrc, {sr, ssc(*,srer*)}];
  etavec = Append[etavec, {sr, vis(*,viser*)}];
  , {i, 1, Count[velprom, _]}];
Print["viscosidad_ce=", etavec]; Print["sssr_ce=", sssrc]; Print["visco_ce=",
 Mean[viscoc]];

Export[StringJoin["ss_sr_promedio_", ToString[s], "_1000x", ToString[hc],
   "um_h", ToString[hs], "mm_ce.dat"], sssrc];
```

```
(*Export["visco_s38_1000x200um_h20mm.dat",visco];
Export["visco_s38_1000x200um_h20mm_ce.dat",viscoc];*)
Export[StringJoin["viscosidad_", ToString[s], "_1000x", ToString[hc], "um_h",
   ToString[hs], "mm.dat"], etavec];
```

References

A. Arora, G. Simone, G. B. Salieb-Beugelaar, J. T. Kim, and A. Manz. Latest developments in micro total analysis systems. *Analytical chemistry*, 82(12):4830–4847, 2010.

F. K. Balagaddé, L. You, C. L. Hansen, F. H. Arnold, and S. R. Quake. Long-term monitoring of bacteria undergoing programmed population control in a microchemostat. *Science*, 309(5731):137–140, 2005.

O. K. Baskurt. *Handbook of hemorheology and hemodynamics*, volume 69. IOS press, 2007.

D. J. Beebe, G. A. Mensing, and G. M. Walker. Physics and applications of microfluidics in biology. *Annual review of biomedical engineering*, 4(1):261–286, 2002.

M. Bilgi, H. Güllü, İ. Kozanoğlu, H. Özdoğu, N. Sezgin, A. T. Sezgin, H. Altay, T. Erol, and H. Müderrisoğlu. Evaluation of blood rheology in patients with coronary slow flow or non-obstructive coronary artery disease. *Clinical hemorheology and microcirculation*, 53(4):317–326, 2012.

R. B. Bird, R. C. Armstrong, and O. Hassager. Dynamics of polymeric liquids. volume 1: fluid mechanics. *A Wiley-Interscience Publication, John Wiley & Sons*, 1987.

D. Bodas and C. Khan-Malek. Formation of more stable hydrophilic surfaces of pdms by plasma and chemical treatments. *Microelectronic engineering*, 83(4):1277–1279, 2006.

H. Bruus. *Theoretical microfluidics. 2008.* New York: Oxford University Press, 2008.

M. A. Burns, B. N. Johnson, S. N. Brahmasandra, K. Handique, J. R. Webster, M. Krishnan, T. S. Sammarco, P. M. Man, D. Jones, D. Heldsinger, et al. An integrated nanoliter dna analysis device. *Science*, 282(5388):484–487, 1998.

H. Cai, J. W. Parks, T. A. Wall, M. A. Stott, A. Stambaugh, K. Alfson, A. Griffiths, R. A. Mathies, R. Carrion, J. L. Patterson, et al. Optofluidic analysis system for amplification-free, direct detection of ebola infection. *Scientific reports*, 5, 2015.

S. Chien. Shear dependence of effective cell volume as a determinant of blood viscosity. *Science*, 168(3934):977–979, 1970.

S. Chien, S. Usami, H. M. Taylor, J. L. Lundberg, and M. I. Gregersen. Effects of hematocrit and plasma proteins on human blood rheology at low shear rates. *Journal of Applied Physiology*, 21(1):81–87, 1966.

S. Chien, S. Usami, and J. F. Bertles. Abnormal rheology of oxygenated blood in sickle cell anemia. *Journal of Clinical Investigation*, 49(4):623, 1970a.

S. Chien, S. Usami, R. J. Dellenback, and M. I. Gregersen. Shear-dependent interaction of plasma proteins with erythrocytes in blood rheology. *American Journal of Physiology–Legacy Content*, 219(1):143–153, 1970b.

C. D. Chin, T. Laksanasopin, Y. K. Cheung, D. Steinmiller, V. Linder, H. Parsa, J. Wang, H. Moore, R. Rouse, G. Umviligihozo, et al. Microfluidics-based diagnostics of infectious diseases in the developing world. *Nature medicine*, 17(8): 1015–1019, 2011.

Y. I. Cho, M. P. Mooney, and D. J. Cho. Hemorheological disorders in diabetes mellitus. *Journal of diabetes science and technology*, 2(6):1130–1138, 2008.

G. R. Cokelet, E. W. Merrill, E. R. Gilliland, H. Shin, A. Britten, and R. E. Wells Jr. The rheology of human blood—measurement near and at zero shear rate. *Transactions of The Society of Rheology (1957-1977)*, 7(1):303–317, 1963.

P. Connes, T. Alexy, J. Detterich, M. Romana, M. D. Hardy-Dessources, and S. K. Ballas. The role of blood rheology in sickle cell disease. *Blood reviews*, 2015.

E. Costa Miracle. Front Dynamics in Microchannels. Master's thesis, Universitat de Barcelona, 2014.

A. K. da Rosa, C. H. Michelin, and R. Campomanes. Reciclaje de pet: evaluación de la eficiencia de separación del contaminante pvc. 2011.

J. V. Dacie, S. M. Lewis, et al. *Practical haematology*. Churchill Livington, London, 2002.

G. Degré, P. Joseph, P. Tabeling, S. Lerouge, M. Cloitre, and A. Ajdari. Rheology of complex fluids by particle image velocimetry in microchannels. *Applied Physics Letters*, 89(2):024104, 2006.

L. Dintenfass. *Blood microrheology: viscosity factors in blood flow, ischaemia, and thrombosis: an introduction to molecular and clinical haemorheology*. Appleton-Century-Crofts, 1971.

A. M. Dondorp, P. A. Kager, J. Vreeken, and N. J. White. Abnormal blood flow and red blood cell deformability in severe malaria. *Parasitology today*, 16(6):228–232, 2000.

D. M. Eckmann, S. Bowers, M. Stecker, and A. T. Cheung. Hematocrit, volume expander, temperature, and shear rate effects on blood viscosity. *Anesthesia & Analgesia*, 91(3):539–545, 2000.

ElgaEurope. Permanent dry film for MEMS and biochips, june 2012. URL `http://www.elgaeurope.it/`.

The Engineering Toolbox. Engineering Toolbox, april 2011. URL `http://www.engineeringtoolbox.com`.

R. Fåhræus. VOL. IX APRIL, 1929 No. 2. *Physiological Reviews*, 9(2), 1929.

R. Fåhræus and T. Lindqvist. The viscosity of the blood in narrow capillary tubes. *American Journal of Physiology–Legacy Content*, 96(3):562–568, 1931.

D. A. Fedosov, B. Caswell, and G. E. Karniadakis. A multiscale red blood cell model with accurate mechanics, rheology, and dynamics. *Biophysical journal*, 98(10): 2215–2225, 2010.

D. A. Fedosov, W. Pan, B. Caswell, G. Gompper, and G. E. Karniadakis. Predicting human blood viscosity in silico. *Proceedings of the National Academy of Sciences*, 108(29):11772–11777, 2011.

M. Gad-el-Hak. *The MEMS handbook*. CRC press, 2001.

G. Gompper, M. Schick, and S. Milner. Self-assembling amphiphilic systems. *Physics Today*, 48(3):91–93, 2008.

P. Guillot, P. Panizza, J. B. Salmon, M. Joanicot, A. Colin, C. H. Bruneau, and T. Colin. Viscosimeter on a microfluidic chip. *Langmuir*, 22(14):6438–6445, 2006.

E. Guyon. *Physical hydrodynamics*. Oxford University Press, 2001.

J. E. Hall. *Guyton and Hall textbook of medical physiology*. Elsevier Health Sciences, 2010.

W. Helfrich. Elastic properties of lipid bilayers: theory and possible experiments. *Zeitschrift für Naturforschung C*, 28(11-12):693–703, 1973.

J. W. Hong and S. R. Quake. Integrated nanoliter systems. *Nature biotechnology*, 21 (10):1179–1183, 2003.

S. M. Hosseini and J. J. Feng. How malaria parasites reduce the deformability of infected red blood cells. *Biophysical journal*, 103(1):1–10, 2012.

Y. Imai, H. Kondo, T. Ishikawa, Chwee T. Lim, and T. Yamaguchi. Modeling of hemodynamics arising from malaria infection. *Journal of biomechanics*, 43(7):1386–1393, 2010.

A. V. Ivlev, V. Steinberg, R. Kompaneets, H. Höfner, I. Sidorenko, and G. E. Morfill. Non-newtonian viscosity of complex-plasma fluids. *Physical review letters*, 98(14): 145003, 2007.

B. Kaoui, G. Biros, and Ch. Misbah. Why do red blood cells have asymmetric shapes even in a symmetric flow? *Physical review letters*, 103(18):188101, 2009.

K. Kikuchi and O. Mochizuki. Micro-PIV (micro particle image velocimetry) visualization of red blood cells (RBCs) sucked by a female mosquito. *Measurement Science and Technology*, 22(6):064002, 2011.

R. G. King and A. L. Copley. Modifications to the Weissenberg rheogoniometer for hemorheological and other biorheological studies. *Biorheology*, 7(1):1, 1970.

R. G. Larson. *The structure and rheology of complex fluids*, volume 33. Oxford university press New York, 1999.

G. R. Lázaro, A. Hernández-Machado, and I. Pagonabarraga. Rheology of red blood cells under flow in highly confined microchannels: I. effect of elasticity. *Soft matter*, 10(37):7195–7206, 2014a.

G. R. Lázaro, A. Hernández-Machado, and I. Pagonabarraga. Rheology of red blood cells under flow in highly confined microchannels. II. Effect of focusing and confinement. *Soft matter*, 10(37):7207–7217, 2014b.

G. Rodríguez Lázaro. *Red Blood Cell mechanics: from membrane elasticity to blood rheology*. PhD thesis, Universitat de Barcelona, 2014.

P. F. Leblond. Hemorheology and blood diseases. In *Clinical Hemorheology*, pages 227–254. Springer, 1987.

H. Lei, D. A. Fedosov, B. Caswell, and G. E. Karniadakis. Blood flow in small tubes: quantifying the transition to the non-continuum regime. *Journal of fluid mechanics*, 722:214–239, 2013.

R. L. Letcher, S. Chien, T. G. Pickering, J. E. Sealey, and J. H. Laragh. Direct relationship between blood pressure and blood viscosity in normal and hypertensive subjects: role of fibrinogen and concentration. *The American journal of medicine*, 70(6):1195–1202, 1981.

Y. Liu and W. K. Liu. Rheology of red blood cell aggregation by computer simulation. *Journal of Computational Physics*, 220(1):139–154, 2006.

G. D. O. Lowe et al. *Clinical blood rheology*. CRC Press, 1988.

C. W. Macosko and R. G. Larson. *Rheology: principles, measurements, and applications*. VCH New York, 1994.

A. Magnin and JM. Piau. Cone-and-plate rheometry of yield stress fluids. Study of an aqueous gel. *Journal of Non-Newtonian Fluid Mechanics*, 36:85–108, 1990.

A. W. Martinez, S. T. Phillips, B. J. Wiley, M. Gupta, and G. M. Whitesides. Flash: a rapid method for prototyping paper-based microfluidic devices. *Lab on a Chip*, 8 (12):2146–2150, 2008.

L. Martynova, L. E. Locascio, M. Gaitan, G. W. Kramer, R. G. Christensen, and W. A. MacCrehan. Fabrication of plastic microfluid channels by imprinting methods. *Analytical chemistry*, 69(23):4783–4789, 1997.

J. C. McDonald and G. M. Whitesides. Poly (dimethylsiloxane) as a material for fabricating microfluidic devices. *Accounts of chemical research*, 35(7):491–499, 2002.

C. D. Meinhart, S. T. Wereley, and J. G. Santiago. PIV measurements of a microchannel flow. *Experiments in fluids*, 27(5):414–419, 1999.

E. W. Merrill. Rheology of blood. *Physiol. Rev*, 49(4):863–888, 1969.

MicroChem. Processing Guidelines for: SU-8 2000 permanent Epoxi Negative Photoresist, 2011.

M. Mohammadi, H. Madadi, and J. Casals-Terré. Microfluidic point-of-care blood panel based on a novel technique: Reversible electroosmotic flow. *Biomicrofluidics*, 9(5):054106, 2015.

W. M. Moreau. *Semiconductor lithography: principles, practices, and materials*. Springer Science & Business Media, 2012.

F. A. Morrison. *Understanding rheology*. Oxford University Press, 2001.

B. Neu and H. J. Meiselman. Depletion-mediated red blood cell aggregation in polymer solutions. *Biophysical journal*, 83(5):2482–2490, 2002.

P. Nghe, G. Degré, P. Tabeling, and A. Ajdari. High shear rheology of shear banding fluids in microchannels. *Applied Physics Letters*, 93(20):204102, 2008.

A. Nilghaz, D. H. B. Wicaksono, D. Gustiono, F. A. A. Majid, E. Supriyanto, and M. R. A. Kadir. Flexible microfluidic cloth-based analytical devices using a low-cost wax patterning technique. *Lab on a Chip*, 12(1):209–218, 2012.

K. Ohene-Frempong, S. J. Weiner, L. A. Sleeper, S. T. Miller, S. Embury, J. W. Moohr, D. L. Wethers, C. H. Pegelow, F. M. Gill, Cooperative Study of Sickle Cell Disease, et al. Cerebrovascular accidents in sickle cell disease: rates and risk factors. *Blood*, 91(1):288–294, 1998.

T. Omori, Y. Imai, K. Kikuchi, T. Ishikawa, and T. Yamaguchi. Hemodynamics in the Microcirculation and in Microfluidics. *Annals of biomedical engineering*, 43(1): 238–257, 2015.

Z. Peng, A. Mashayekh, and Q. Zhu. Erythrocyte responses in low-shear-rate flows: effects of non-biconcave stress-free state in the cytoskeleton. *Journal of Fluid Mechanics*, 742:96–118, 2014.

C. Picart, JM. Piau, H. Galliard, and P. Carpentier. Human blood shear yield stress and its hematocrit dependence. *Journal of Rheology (1978-present)*, 42(1):1–12, 1998.

C. Pipe and G. H. McKinley. Microfluidic rheometry. *Mechanics Research Communications*, 36:110–120, 2009.

K. L. Pitts and M. Fenech. High speed versus pulsed images for micro-particle image velocimetry: a direct comparison of red blood cells versus fluorescing tracers as tracking particles. *Physiological measurement*, 34(10):1363, 2013.

J. L. Poiseuille. *Recherches expérimentales sur le mouvement des liquides dans les tubes de très-petits diamètres*. Imprimerie Royale, 1844.

G. Pontrelli, I. Halliday, S. Melchionna, T. J Spencer, and S. Succi. Lattice Boltzmann method as a computational framework for multiscale haemodynamics. *Mathematical and Computer Modelling of Dynamical Systems*, 20(5):470–490, 2014.

M. Pradas Gené. *Interfases in disordered media*. PhD thesis, Universitat de Barcelona, 2009.

A. R. Pries, D. Neuhaus, and P. Gaehtgens. Blood viscosity in tube flow: dependence on diameter and hematocrit. *American Journal of Physiology-Heart and Circulatory Physiology*, 263(6):H1770–H1778, 1992.

D. Qin, Y. Xia, and G. M. Whitesides. Soft lithography for micro-and nanoscale patterning. *Nature protocols*, 5(3):491–502, 2010.

M. Queralt Martín. Fluid Fronts in Hidrophilic and Hidrophobic Microchannels. Master's thesis, Universitat de Barcelona, 2009.

M. Queralt-Martín, M. Pradas, R. Rodríguez-Trujillo, M. Arundell, E. Corvera Poiré, and A. Hernández-Machado. Pinning and avalanches in hydrophobic microchannels. *Physical review letters*, 106(19):194501, 2011.

M. W. Rampling. Blood viscosity characteristics and red cell aggregation. *Rheology of food, pharmaceutical and biological materials with general rheology/edited by RE Carter*, 1990.

D. R. Reyes, D. Iossifidis, P-A. Auroux, and A. Manz. Micro total analysis systems. 1. introduction, theory, and technology. *Analytical chemistry*, 74(12):2623–2636, 2002.

L. G. Rigat-Brugarolas, A. Homs-Corbera, and J Samitier. Simple alignment marks patterning for multilayered master fabrication, june 2012. URL `http://www.blogs.rsc.org/chipandtips/2012/03/12/`.

A. I. Rodríguez Villarreal. *Microfluidic Device for Blood Plasma Separation and Magnetic Cell Manipulation*. PhD thesis, Universitat de Barcelona, 2011.

A. I. Rodríguez-Villarreal, M. Arundell, M. Carmona, and J. Samitier. High flow rate microfluidic device for blood plasma separation using a range of temperatures. *Lab on a Chip*, 10(2):211–219, 2010.

E. K. Sackmann, A. L. Fulton, and D. J. Beebe. The present and future role of microfluidics in biomedical research. *Nature*, 507(7491):181–189, 2014.

J. G. Santiago, S. T. Wereley, C. D. Meinhart, D. J. Beebe, and R. J. Adrian. A particle image velocimetry system for microfluidics. *Experiments in fluids*, 25(4):316–319, 1998.

S. Sarkar and T. S. Rosenkrantz. In *Seminars in Fetal and Neonatal Medicine*.

J. B. Segur and H. E. Oberstar. Viscosity of glycerol and its aqueous solutions. *Industrial & Engineering Chemistry*, 43(9):2117–2120, 1951.

R. Sista, Z. Hua, P. Thwar, A. Sudarsan, V. Srinivasan, A. Eckhardt, M. Pollack, and V. Pamula. Development of a digital microfluidic platform for point of care testing. *Lab on a Chip*, 8(12):2091–2104, 2008.

T. M. Squires and S. R. Quake. Microfluidics: Fluid physics at the nanoliter scale. *Reviews of modern physics*, 77(3):977, 2005.

V. Srinivasan, V. K. Pamula, and R. B. Fair. An integrated digital microfluidic lab-on-a-chip for clinical diagnostics on human physiological fluids. *Lab on a Chip*, 4(4): 310–315, 2004.

N. Srivastava, R. D. Davenport, and M. A. Burns. Nanoliter viscometer for analyzing blood plasma and other liquid samples. *Analytical chemistry*, 77(2):383–392, 2005.

H. A. Stone, A. D. Stroock, and A. Ajdari. Engineering Flows in Small Devices: Microfluidics Toward a Lab-on-a-Chip. *Annual Review of Fluid Mechanics*, 36: 381–411, 2004.

Y. Sugii, R. Okuda, K. Okamoto, and H. Madarame. Velocity measurement of both red blood cells and plasma of in vitro blood flow using high-speed micro PIV technique. *Measurement science and Technology*, 16(5):1126, 2005.

P. Tabeling. *Introduction to microfluidics*. Oxford University Press, 2010.

L. O. Tañá, J. Cid, A.I.R. Villarreal, J. Colomer-Farrarons, and P.L. Miribel-Català. Design and implementation of a micro-rheometer for poc applications. In *XIV Mediterranean Conference on Medical and Biological Engineering and Computing 2016*, pages 451–455. Springer, 2016.

M. Thiébaud, Z. Shen, J. Harting, and Ch. Misbah. Prediction of anomalous blood viscosity in confined shear flow. *Physical review letters*, 112(23):238304, 2014.

T. Thorsen, S. J. Maerkl, and S. R. Quake. Microfluidic large-scale integration. *Science*, 298(5593):580–584, 2002.

G. B. Thurston. Viscoelasticity of human blood. *Biophysical journal*, 12(9):1205, 1972.

G. B. Thurston and N. M. Henderson. Effects of flow geometry on blood viscoelasticity. *Biorheology*, 43(6):729–746, 2006.

M. Toner and D. Irimia. Blood-on-a-chip. *Annual review of biomedical engineering*, 7:77, 2005.

C. Trejo-Soto, E. Costa-Miracle, I. Rodriguez-Villarreal, J. Cid, T. Alarcón, and A. Hernández-Machado. Capillary filling at the microscale: Control of fluid front using geometry. *PLOS ONE*, 11(4):e0153559, 2016a.

C. Trejo-Soto, E. Costa-Miracle, I. Rodríguez-Villarreal, J. Cid, M. Castro, T. Alarcón, and A. Hernández-Machado. Front micro-rheology of non-Newtonian Blood behavior. *preprint*, 2016b.

C. Tropea, A. L. Yarin, and J. F. Foss. *Springer handbook of experimental fluid mechanics*, volume 1. Springer Science & Business Media, 2007.

P. Vulto, N. Glade, L. Altomare, J. Bablet, L. Del Tin, G. Medoro, I. Chartier, N. Manaresi, M. Tartagni, and R. Guerrieri. Microfluidic channel fabrication in dry film resist for production and prototyping of hybrid chips. *Lab on a Chip*, 5(2):158–162, 2005.

N. Wangler, L. Gutzweiler, K. Kalkandjiev, C. Müller, F. Mayenfels, H. Reinecke, R. Zengerle, and N. Paust. High-resolution permanent photoresist laminate TMMF for sealed microfluidic structures in biological applications. *Journal of Micromechanics and Microengineering*, 21(9):095009, 2011.

M. E. Warkiani, A. K. P. Tay, B. L. Khoo, X. Xiaofeng, J. Han, and Ch. T. Lim. Malaria detection using inertial microfluidics. *Lab on a Chip*, 15(4):1101–1109, 2015.

E. W. Washburn. The dynamics of capillary flow. *Physical review*, 17(3):273, 1921.

S. T. Wereley, J. G. Santiago, R. Chiu, C. D. Meinhart, and R. J. Adrian. Microresolution particle image velocimetry. In *BiOS'98 International Biomedical Optics Symposium*, pages 122–133. International Society for Optics and Photonics, 1998.

G. M. Whitesides. The origins and the future of microfluidics. *Nature*, 442(7101): 368–373, 2006.

S. R. F. Whittaker and F. R. Winton. The apparent viscosity of blood flowing in the isolated hindlimb of the dog, and its variation with corpuscular concentration. *The Journal of physiology*, 78(4):339–369, 1933.

T. Wu and J. J. Feng. Simulation of malaria-infected red blood cells in microfluidic channels: Passage and blockage. *Biomicrofluidics*, 7(4):044115, 2013.

Y. Xia, J. J. McClelland, R. Gupta, D. Qin, XM. Zhao, L. L. Sohn, R. J. Celotta, and G. M. Whitesides. Replica molding using polymeric materials: A practical step toward nanomanufacturing. *Advanced Materials*, 9(2):147–149, 1997.

C. Zhang, D. Xing, and Y. Li. Micropumps, microvalves, and micromixers within pcr microfluidic chips: advances and trends. *Biotechnology advances*, 25(5):483–514, 2007.